Theoretical studies of zeolite catalysis

A thesis submitted to the University of Manchester

for the degree of Doctor of Philosophy

in the Faculty of Science

by

Stephen Paul Greatbanks

March 1995

The Department of Chemistry

ProQuest LLC.
789 East Eisenhower Parkway
P.O. Box 1346
Ann Arbor, MI 48106 – 1346

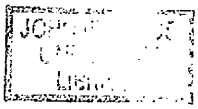

Contents

Contents 2

Abstract 7

Declaration 8

Copyright notice 9

Acknowledgements 10

Epigram 11

The Author 12

Dedication 13

Chapter One - Zeolites and solid state catalysis 14

1.1 - Zeolites in historical context 15

1.2 - Zeolite structure and catalysis 17

1.2.1 - Zeolite structural features 17

1.2.2 - Shape selective catalysis 18

1.2.3 - Brønsted acidity 20

1.3 - Studying zeolite catalysis 22

1.3.1 - Experimental studies of zeolite catalysis 22

1.3.2 - Computational studies of zeolite catalysis 23

1.4 - References 25

Chapter Two - Theoretical methods 27

2.1 - Introduction 28

2.2 - Molecular Orbital theory 29

2.2.1 - Hartree-Fock theory 29

2.2.2 - The Roothaan-Hall equations 33

2.3 - Basis sets and orbitals 34

2.3.1 - Polarisation and diffuse functions 36

2.4 - Geometry Optimisation methods 37

2.5 - Electronic correlation and density functionals 38

2.5.1 - Møller-Plesset perturbation theory 38

2.5.2 - Density functional methods 40

2.6 - Periodic Hartree-Fock theory 42

2.6.1 - Introduction 42

2.6.2 - CRYSTAL 92 42

2.6.3 - Basis functions and orbitals 44

2.6.4 - Computational approach 46

2.6.5 - Approximate methods 50

2.6.6 - Periodic electrostatic potentials 52

2.7 - References 54

Chapter Three - Embedded cluster modelling.....56

3.1 - Cluster modelling of zeolites - previous work.....57

3.2 - The embedded cluster model.....59

3.2.1 - Overview of the model.....59

3.2.2 - Computational strategy.....60

3.2.3 - Cluster selection.....61

3.2.4 - Cluster termination procedure.....62

3.2.5 - Sampling grid selection.....64

3.2.6 - Difference potential evaluation.....65

3.2.7 - Fitting grid selection.....66

3.2.8 - Point charge evaluation.....66

3.2.9 - Model construction and nomenclature.....68

3.3 - Model validation.....69

3.3.1 - Selecting a system for validation.....69

3.3.2 - Computational details of model generation.....71

3.3.3 - Electrostatic potentials.....74

3.3.4 - Cluster geometries.....78

3.3.4.1 - Computational details.....78

3.3.4.2 - Computational results.....79

3.3.5 - Interaction energies.....81

3.3.5.1 - Computational details.....81

3.3.5.2 - Computational results.....82

3.4 - Refinement of the fitting procedure 86

3.4.1 - Determining the optimum charge field 86

3.4.2 - Determining the optimum difference potential 87

3.4.3 - Optimising the screening procedures 89

3.4.4 - Cluster-substrate optimisations 91

3.5 - Conclusions 93

3.6 - References 95

Chapter Four - Studies of catalysis in Zeolite Y 97

4.1 - Introduction 98

4.2 Periodic Hartree-Fock study of zeolite Y 99

4.3 - Si-OH terminated T3 clusters 101

4.3.1 - Cluster selection and fitting details 101

4.3.2 - Computational results 105

4.3.2.1 - Cluster geometry 107

4.3.2.2 - Brønsted site vibrational frequencies 108

4.3.2.3 - Deprotonation energies 110

4.4 - Si-H terminated T3 clusters 113

4.4.1 - Cluster selection and fitting details 113

4.4.2 - Cluster optimisations 115

4.4.3 - Interaction of water with zeolite Y T3 clusters 117

4.4.4 - Interaction of methanol with zeolite Y T3 clusters 126

4.4.5 - Interaction of ammonia with zeolite Y T3 clusters 133

4.4.6 - Thermochemistry of ammonia binding in zeolite Y 140

4.5 - Si-OH terminated T2 clusters 142

4.5.1 - Cluster selection and fitting details 142

4.5.2 - Interaction of ammonia with zeolite Y T2 clusters 145

4.6 - Conclusions 148

4.7 - References 151

Appendix A 154

Appendix B 158

Abstract

The University of Manchester

ABSTRACT OF THESIS submitted by **STEPHEN PAUL GREATBANKS** for the Degree of Doctor of Philosophy and entitled **THEORETICAL STUDIES OF ZEOLITE CATALYSIS**.

Month and Year of Submission: March 1995.

The work presented in this thesis applies state of the art *ab initio* molecular orbital theory to the study of catalysis in zeolite minerals. A model, designed to include an accurate representation of the electrostatic environment of the infinite zeolite within finite cluster models, is developed and computationally implemented. The zeolite cancrinite is then used in the validation of this embedded cluster model, by comparison with results from periodic Hartree-Fock calculations. The new model is then used to predict structural properties of acidic Brønsted sites, as well as structure of species adsorbed in the zeolite pore. The important zeolite Y is then studied, with calculations of vibrational properties and geometries of crystallographically different sites within the zeolite. The interaction of water, methanol and ammonia with the zeolite is considered, with calculated predictions of vibrational properties, binding energies and geometries. The importance of cluster size, termination effects and electronic correlation are also investigated. The work has shown our new model to be successful in modelling a range of zeolite properties.

Declaration

No portion of the work referred to in this thesis has been submitted in support of an application for another degree or qualification at this or any other university or institute of learning.

Copyright notice

Acknowledgements

I would like to offer my thanks to the following people who have helped me with the work contained in this thesis:

Professor Ian Hillier for his patience, assistance, insight and funding.

Dr Paul Sherwood for his generous help, code, and technical expertise.

Dr Mark Vincent, Dr Neil Burton and Dr Matt Cooper for help with things technical.

Dr Nic Harrison for help with the periodic Hartree-Fock section.

Professor C. R. A. Catlow, Dr J. D. Gale and Dr V. R. Saunders for their assistance.

I would like to acknowledge the members of the group, past and present, for making my time here more enjoyable. Special thanks (in strict alphabetical order) to:

Catherine Apps, Gina Berry, Charlie Bond, Bob Buesnel, Aldo Cervi, Ian Clements, Simon Craw, Dave Dos Santos, Andy Fearn, Shaun Fletcher, Steve St. Gallay, Richard Hall, Steve Harrop, John Hollifield, Carolyn Hughes, Nicola Le Gassicke, Carole & Chris Leary, Noj Malcolm, Sarah Maw, Pat McCabe, Gordon Middleton, Mike Minns, Ian Palmer, Chris Parkinson, Mark Peterson, Matt Randall, Matthias Stein, Mike Tennant, Keith Trollope, and Phill Young.

Extra special thanks to Rob Laird for putting up with me at home as well as work.

Thanks to my family, Dad, Mum, Mark, Joanne, Michael and David for all their help.

Final thanks to Sally (the dog) and Basil (the cat) for providing light relief.

Epigram

The moving Moon went up the sky,
And no where did abide:
Softly she was going up,
And a star or two beside.

Her beams bemocked the sultry main,
Like April hoar-frost spread;
But where the ship's huge shadow lay,
The charmed water burnt alway
A still and awful red.

Beyond the shadow of the ship,
I watched the water-snakes:
They moved in tracks of shining white,
And when they reared, the elfish light
Fell off in hoary flakes.

Within the shadow of the ship
I watched their rich attire:
Blue, glossy green, and velvet black,
They coiled and swam; and every track
Was a flash of golden fire.

O happy living things! no tongue
Their beauty might declare:
A spring of love gushed from my heart,
And I blessed them unaware:
Sure my kind saint took pity on me,
And I blessed them unaware.

The self same moment I could pray;
And from my neck so free
The Albatross fell off, and sank
Like lead into the sea.

Taken from The Rime of the Ancient Mariner by Samuel Taylor Coleridge.

The Author

The author studied for his first degree in Chemistry between 1987 and 1990 at UMIST. In 1991 he joined the Theory group at the Department of Chemistry in the University of Manchester, engaged in theoretical studies of zeolite catalysis under the supervision of Professor Ian Hillier.

Dedication

This thesis is dedicated to my parents, John and Christine, for their constant support, both emotional and financial, throughout my education. Without them, this work would have never been accomplished. My heartfelt thanks and love.

Chapter 1

Zeolite catalysis

1.1 - Zeolites in historical context.

Zeolites are aluminosilicate minerals, both naturally occurring and synthetic, which are of increasing industrial importance due to their unique structural and chemical properties. Zeolites are currently used in a large and increasing variety of distinct roles which fall into two primary areas. The major use of zeolites is as industrial catalysts, chiefly in the petrochemical field, where they are used as cracking catalysts in the refining of crude oil. Zeolites also find considerable use as adsorbents, particularly in the field of detergency, where they are increasingly used as an alternative to ecologically unsound sodium tripolyphosphates.

The name 'zeolite', derived from the Greek ξειν (zein) meaning to boil and λιθοζ (lithos) meaning stone, was devised in 1756 by the Swedish mineralogist Cronstedt, who observed intumesence when a natural zeolite was placed in a flame[1]. The study of zeolites continued at a modest pace until the middle of the twentieth century when pioneering work in the 1940's by Barrer into the characterisation of zeolites and their activity, and subsequently their synthesis by crystallisation from aqueous gels of silicates and aluminates, generated huge interest. The culmination of his work was the successful production of a synthetic analogue of the naturally occurring zeolite Mordenite[2].

During the 1950's and 1960's, Milton and Breck of the Linde division of the Union Carbide company developed a range of novel zeolites classified as types A, X and Y, which proved to be of considerable economic importance and were the spur for the subsequent rise of the use of zeolites as industrial catalysts. Zeolite A is finding

increasing use as a water softening agent in detergents, where it acts by the sequestration of Ca^{2+} ions, whilst zeolite Y is the primary industrial catalytic cracking catalyst, used during the refining of crude oil. The importance of these catalysts can be gauged from the scale of their usage, with zeolite A alone constituting over two thirds of the world market of around 600,000 tonnes, with zeolite Y contributing around 100,000 tonnes[3].

Work during the 1970's resulted in the synthesis of high-silica zeolites with pores of medium size (in the range 4.5-6.0 Å), complementing the large and small pored zeolites already known. These zeolites, particularly ZSM-5[4], have found considerable use in many petrochemical processes due to their pore dimensions being of the same order as gasoline-range hydrocarbons. Other work involved the modification of zeolite reactivity by the use of hydrothermal treatment to produce ultra-stable forms of zeolites, and the incorporation of metal ions within zeolites[5].

Contemporary research into zeolites is a large and diversifying area with the discovery of novel zeolite framework geometries, and zeolite-like structures like the AlPO (aluminophosphates) SAPO, and more recently the MeAlPO minerals. Whilst there is considerable interest in these other compounds, the study of zeolites themselves is still proving a fruitful area. For example, chiral zeolites have recently been discovered, e.g. zeolite beta, which offer great prospects for asymmetric syntheses.

One particular area in which zeolites are finding an increasing number of applications is environmental chemistry, where they are used in the purification of water and the cleanup of nuclear contamination, though the possibility of them being used to remove toxic heavy metals from the environment is also being investigated.

1.2 - Zeolite structure and catalysis

1.2.1 - Zeolite structural features

Zeolites have structures composed of tetrahedrally orientated TO_4 units (where T is 4 co-ordinated silicon or 3 co-ordinated aluminium) linked *via* corner sharing. From this modest precursor, a series of more complex building units[6], often referred to as structural building units (SBU), some examples of which are shown in figure 1.1, can be generated.

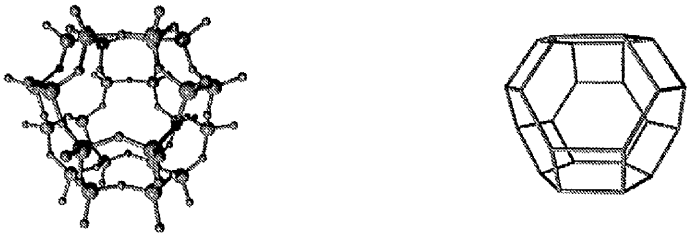

(a) The sodalite cage - two views showing all atoms (left) and the T sites only (right).

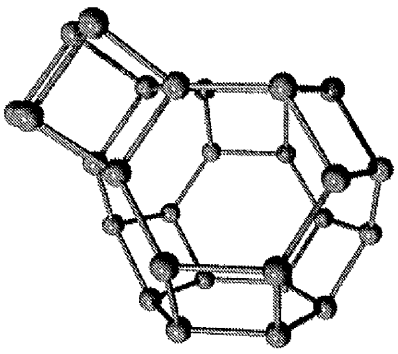

(b) Double 4 ring (D4R) attached to a sodalite cage.

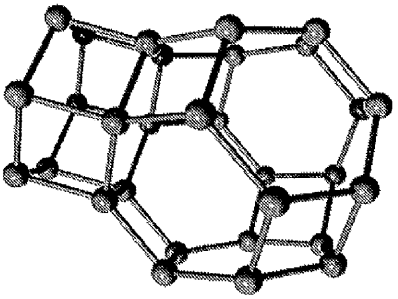

(c) Double 6 ring (D6R) attached to a sodalite cage.

figure 1.1 - Zeolite structural building units.

Figure 1.1(a) shows the cubo-octahedral sodalite cage, one of the most important units which forms the basis of a number of industrially important zeolites, including both zeolite A and zeolite Y. Figure 1.1(b) shows a double 4 ring (D4R) attached to one of the square faces of a sodalite cage (repetition of this motif gives the zeolite A structure), and figure 1.1(c) shows a hexagonal-prismatic double 6 ring (D6R) linked to a hexagonal face of a sodalite cage, the basis of the zeolite Y framework structure. A comprehensive overview of zeolite structures, detailing the nomenclature of SBU and framework topologies, has been published by Meier and Olsen[7].

Although zeolites are often referred to as 'molecular sieves', this term is more correctly used to describe a generic class of pore-containing materials of which the zeolites are currently the most industrially important. The most commercially significant characteristic of zeolite minerals is the presence of pore systems, in 1, 2 and frequently 3 dimensions, through which molecular species can diffuse. Additionally, the presence of these channel systems gives zeolite minerals a very high internal surface area, a limiting property in surface catalysed reactions, which is difficult to achieve using traditional catalysts where the maximum surface area attainable depends on the ability to produce very small particles of the catalyst, usually *via* milling.

1.2.2 - Shape selective catalysis

The pore systems within zeolites are known to contain large electrostatic fields, which are widely thought to be important in the orientation and stabilisation of substrates during reaction processes, paralleling the behaviour of biological catalysts. Indeed, it is

often remarked that zeolites behave as though they were solid state enzymes. The substrate selectivity associated with enzymes is found in zeolites, which demonstrate the ability to prevent or allow the sorption of molecules on the basis of shape or size, endowing them with a most desirable catalytic property. Shape selective catalysis, illustrated in figure 1.2, is employed in a range of situations whereby the progress of a reaction and the resulting product distribution can be altered, often dramatically, by selectively admitting or excluding the reactants, transition states or products[8]. The effect of this property is shown to dramatic effect in the Methanol to Gasoline (MTG) reaction[9], developed by the Mobil Oil Company in 1973. In this process, a stream of methanol is passed over a H-ZSM-5 catalyst under modest conditions, resulting in the quantitative production of high quality gasoline and water. The size of the zeolite pores is responsible for the sharp cut-off in the product distribution in the region of C_{11} compounds, the largest hydrocarbons which can exist within the pores, which fortuitously corresponds to the upper end of the gasoline range. A result of this inherent restriction on the product distribution is that no additional, expensive processing to remove unwanted heavier residues is required. The potential economic impact of this process, in view of the fact that most of the remaining fossil-fuel reserves are in the form of natural gas, is enormous, and has generated considerable research activity. Indeed, the process is used on a commercial scale in some regions of the world, South Africa and New Zealand, for example, in which no crude oil reserves exist.

Figure 1.2 demonstrates how a zeolite can exhibit both reactant or product selective catalysis. Reactant selectivity arises when only the *para* di-substituted benzene can enter the pore system, where it takes part in a reaction scheme, with the *meta* isomer sterically excluded - a more trivial example of this is the cracking of hydrocarbons in

which linear alkanes can diffuse into the catalyst erionite, though branched isomers cannot. Product shape selective catalysis can be envisaged within the scheme shown in figure 1.2, whereby if the *meta* di-substituted product could be formed by some reaction process within the zeolite, it would be sterically unable to leave (an industrial process which uses this effect is the methylation of toluene, where *ortho* and *meta* xylene products cannot leave the zeolite, but the reaction conditions are such that the unwanted isomers are converted into the *para* xylene which forms essentially 100% of the product stream).

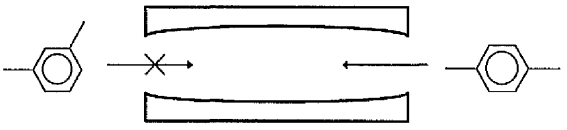

figure 1.2 - Shape selective catalysis

Analogously, transition state selectivity can be applied to alter product distributions by using the zeolite pores to constrain sterically the transition states which can form, allowing routes to unwanted products to be excluded.

1.2.3 - Brønsted acidity

In addition to the shape selectivity and very large internal surface area of zeolite catalysts, an additional mode of catalysis exists which results from the presence of acidic sites within the zeolite pores. These acidic sites arise from the isomorphous replacement of silicon by aluminium at a zeolite T site, resulting in the formation of a negatively

charged defect in the zeolite lattice. To maintain charge neutrality, cations, frequently sodium or potassium, are associated with these aluminium sites. An alternative situation arises as the result of hydrothermal treatment, in which a proton rather than a metal cation is associated with the aluminium, whereby a hydroxyl group is formed, shown in figure 1.3.

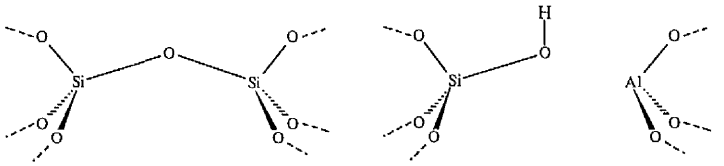

(a) Siliceous zeolite. *(b) Zeolite Brønsted site.*

figure 1.3- Isomorphous replacement of silicon forming a Brønsted site.

The hydroxyl group thus formed is extremely labile, causing the site to behave in the manner of a classic Brønsted (proton donating) acid. These highly acidic sites give rise to one of the most important modes of zeolite catalytic activity, providing the ideal catalysts for industrial processes in which protonation of a substrate within the zeolitic pore system is an important step. The action and importance of these sites can be clearly demonstrated by the fact that the Methanol to Gasoline reaction fails to occur in silicalite, the purely siliceous analogue of ZSM-5, in which there are no aluminium substitutions and therefore no Brønsted sites. Knowledge of the elusive first stage of the mechanism by which this specific reaction occurs, and enhanced understanding of the chemistry of these sites in general, may point to modifications which could be made to the catalysts to produce enhanced catalytic activity.

1.3 - Studying zeolite catalysis

1.3.1 - Experimental studies of zeolite catalysis

Many groups, utilising the whole spectrum of experimental methods, have probed the structure and chemistry of zeolite acid sites, and much is known about them and their role in catalytic processes. There are, however difficulties associated with experimental approaches which limit the information they can provide.

A difficulty in the determination of the local geometry at the Brønsted site arises because X-ray crystallographic methods usually employed in structure determination are unable to resolve the location of acidic hydrogens. A more general problem of diffraction techniques, including neutron diffraction in which the acidic hydrogens can be resolved, is their inability to provide detailed information about the co-ordination environment of aluminium at specific lattice positions. This occurs because although aluminium substitution often occurs preferentially at certain T sites, the occupancy is often very low and the virtually identical scattering factors of silicon and aluminium prevents their individual resolution. As a result structural differences associated with aluminium substitutions become averaged over the T sites, and much of the information associated with the local co-ordination environment of the Brønsted site is lost.

A range of chemical techniques have been employed in the past to investigate zeolite acidity including titration[10,11], calorimetry[12], and spectroscopic methods[13,14], yet the direct determination of Brønsted acidity, and the acidity of solid acids in general, remains a difficult experimental problem.

Titration techniques, particularly those which use the common approach of titrating a series of Hammett indicators directly against zeolite acid sites to gauge the acidity, are plagued by a fundamental difficulty. The problem arises in that the basicity of the Hammett indicators is determined in aqueous solution, but is strongly solvent dependent. The zeolite framework can considerably modify the solvation of the bases, evidenced by the interaction of ammonia and pyridine with H-ZSM-5 where the heat of interaction of pyridine is found to be substantially larger than that of ammonia, even though the solution phase result predicts ammonia to be considerably more basic. Thus the use of Hammett indicators on zeolite acidic sites must be viewed with suspicion unless substantially more is understood about the influence of the zeolite framework on base solvation.

More widely used are spectroscopic studies in which IR frequencies or NMR shifts of the acidic hydrogen, or interaction with probe molecules (e.g. CO[15,16], CD_3CN[17], and other weak bases[18]) are used to determine the acidity of the Brønsted site. The application of spectroscopic techniques still does not, however address the problem of direct, unambiguous consideration of specific zeolite T sites.

1.3.2 - Computational studies of zeolite catalysis

As in many other areas of chemistry, the realisation that increasingly sophisticated and powerful computer modelling techniques can be of great assistance, particularly when allied to experimental studies, has meant that theoretical studies of zeolite structure and catalysis are widespread. Many differing approaches have been applied, from

empirical studies using molecular mechanical force fields[19,20] (with the recent advent of zeolite-specific force fields[21,22]) or lattice dynamics studies[23], through to non-empirical *ab initio* approaches[24,25,26,27,28,29] which attempt to gain a more fundamental understanding of the electronic structure of zeolites, and how this influences catalytic activity. The application of these methods will be described in more detail in later chapters.

Theoretical methods, covered in more detail in chapter 2, are now capable of providing the same range of information as experiment, including the calculation of binding energies and geometries, IR and NMR properties, with the additional benefit of being able to probe different T sites directly. An additional benefit afforded by theoretical studies is that direct *ab initio* determinations of the proton affinity of the anionic zeolite, a crucial measure of the acidity of the zeolite Brønsted site, can be made, in contrast with experimental studies which rely on empirical relationships between the proton affinity and the vibrational properties of the acidic hydrogen.

Within an *ab initio* approach, the most common method of modelling zeolites and their catalysis involves the use of small cluster models in which a fragment of the infinite periodic crystal is considered, and for convenience, the 'dangling' bonds which result from the truncation of the infinite system are usually saturated with hydrogen atoms (though alternative termination methods have been suggested[24]) to give a neutral cluster. Due to the high computational cost of *ab initio* calculations, the size of the clusters that can be considered is limited by the available computational resources. Typically, 2 or 3 T sites are used (where T denotes Si or Al), though recent studies have systematically investigated the properties of larger clusters with up to 25 T sites[30]. The implications of the use of small cluster models will be discussed in later chapters.

1.4 - References

[1] Cronstedt, A. F., *Akad. Handl. Stockholm*, **1756**, 18, 120

[2] Barrer, R. M., *J. Chem. Soc.*, **1948**, 2158

[3] Moscou, L., in "*Introduction to Zeolite Science and Practice*", Elsevier, Amsterdam, **1991**

[4] Olson, D. H.; Kokotailo, G. T.; Lawton, S. L.; Meier, W. M., *J. Phys. Chem.*, **1981**, 85, 2238

[5] Szostak, R., in "*Introduction to Zeolite Science and Practice*", Elsevier, Amsterdam, **1991**

[6] Van Koningsveld, H., in "*Introduction to Zeolite Science and Practice*", Elsevier, Amsterdam, **1991**

[7] Meier, W. M.; Olsen, D. H., "*Atlas of Zeolite Structure Types*", 2nd rev. edn., Butterworths, London, **1987**

[8] Dwyer, J., *Nature*, **1989**, 339, 174

[9] Meisel, S. L.; McCullough, J. P.; Lechthaler, C. H.; Weisz, P. B., *CHEMTECH*, **1976,** 86

[10] Crocker, M.; Herold, R. H. M.; Sonnemans, M. H. W.; Emeis, C. A.; Wilson, A. E.; van der Moolen, J. N., *J. Phys. Chem.*, **1993**, 97, 432

[11] Sonnemans, M. H. W.; den Heijer, C.; Crocker, M., *J. Phys. Chem.*, **1993**, 97, 440

[12] Parrillo, D. J.; Gorte, R. J.; Farneth, W. E., *J. Am. Chem. Soc.*, **1993**, 115, 12441

[13] Gil, B.; Broclawik, E.; Datka, J.; Klinowski, J., *J. Phys. Chem.*, **1994**, 98, 930

[14] van Hooff, J. H. C.; Roelofsen, J. W., in "*Introduction to Zeolite Science and Practice*", Elsevier, Amsterdam, **1991**

[15] Makarova, M. A.; Al-Ghefaili, K. M.; Dwyer, J., *J. Chem. Soc., Faraday Trans.*, **1994**, 90, 383

[16] Zecchina, A.; Bordiga, S.; Spoto, G.; Scarano, D.; Petrini, G.; Leofanti,G.; Padovan, M.; Otero Areán, C., *J. Chem. Soc., Faraday Trans.*, **1992**, 88, 2959

[17] Pelmenschikov, A. G.; van Santen, R. A.; Jänchen, J.; Meier, E., *J. Phys. Chem.*, **1993**, 97, 11071

[18] Makarova, M. A.; Ojo, A. F.; Karim, K.; Hunger, M.; Dwyer, J., *J. Phys. Chem.*, **1994**, 98, 3619

[19] Mabilia, M.; Pearlstein, R. A.; Hopfinger, A. J., *J. Am. Chem. Soc.*, **1987**, 109, 7960

[20] Nicholas, J. B.; Hopfinger, A. J.; Trouw, F. R.; Iton, L. E., *J. Am. Chem. Soc.*, **1991**, 113, 4792

[21] Kramer, G. J.; Farragher, N. P.; van Beest, B. H. W.; van Santen, R. A., *Phys. Rev. B.*, **1991**, 43, 5068

[22] Hill, J-R.; Sauer, J., *J. Phys. Chem.*, **1994**, 98, 1238

[23] Vetrivel, R.; Catlow, C. R. A.; Colbourn, E. A., *J. Phys. Chem.*, **1989**, 93, 4594

[24] Sauer, J., *Chem. Rev.*, **1989**, 89, 199 and references therein

[25] Greatbanks, S. P.; Sherwood, P.; Hillier, I. H., *J. Phys. Chem.*, **1994**, 98, 8134

[26] Sauer, J., *J. Phys. Chem.*, **1987**, 91, 2315

[27] Mortier, W. J.; Sauer, J.; Lercher, J. A.; Noller, H., *J. Phys. Chem.*, **1984**, 88, 905

[28] O'Malley, P. J.; Dwyer, J., *J. Phys. Chem.*, **1988**, 92, 3005

[29] Nicholas, J. B.; Hess, A. C., *J. Am. Chem. Soc.*, **1994**, 116, 5428

[30] Brand, H. V.; Curtiss, L. A.; Iton, L. E., *J. Phys. Chem.*, **1992**, 96, 7725

Chapter 2

Theoretical methods

2.1 - Introduction

The aim of this thesis is primarily to study catalytic chemical processes within zeolites. A first step towards this goal is a consideration of the limits of validity of *ab initio* cluster models in the study of chemistry within zeolites. Fortuitously, the recent implementation of *ab initio* molecular orbital theory for periodic systems[1] (described in more detail in section 2.6) provides a benchmark by which cluster models be judged. In this thesis, the *ab initio* wavefunction of the periodic system is used in the generation of a model intended to include a more realistic representation of the zeolite electrostatic potential, of obvious importance in the stabilisation of substrates within the zeolite. The basis of the model is that a set of point charges, inside which a small cluster is embedded, can act in tandem with the electrostatic potential of the cluster to reproduce the electrostatics of the periodic zeolite. Chapter 3 covers the implementation of the embedded cluster model and where possible, comparison is then made between properties of the periodic system, the bare cluster and the embedded cluster models. Subsequent calculations, detailed in Chapter 4, apply the embedded cluster model to systems and situations of chemical interest, especially the important area of substrate protonation by zeolites.

The theoretical methods used in the development and application of the embedded cluster model are described in the rest of this chapter.

2.2 - Molecular Orbital theory

2.2.1 - Hartree-Fock theory

The basis of theoretical methods which are used to describe chemical systems in terms of electronic structure depend fundamentally on the ability to solve the time independent, non-relativistic Schrödinger equation[2].

$$\hat{H}\Psi = E\Psi \qquad (2.1)$$

In this eigenvalue equation, the total molecular wavefunction is denoted Ψ, the molecular energy E, and $\hat{H}$ is the Hamiltonian operator for the system, containing information about the kinetic and potential energies of the particles of the system. In practice, the many-bodied nature of this equation prevents exact solution, so an alternative method is followed where approximations are introduced and solutions to the approximated equations are sought instead.

The first approximation applied in the solution of the Schrödinger equation for molecular systems is that due to Born and Oppenheimer[3] which assumes that the motion of electrons is very much faster than that of the nuclei, allowing the electrons to be considered as moving in the potential generated by the field of stationary nuclei. Thus, we can reduce the molecular problem to a consideration of an electronic Hamiltonian for a fixed set of nuclear co-ordinates.

$$\hat{H}_{elec} = \sum_{i=1}^{n} -\frac{h^2}{8\pi^2 m}\nabla_i^2 - \sum_{i=1}^{n}\sum_{\alpha=1}^{N}\frac{Z_\alpha e^2}{4\pi\varepsilon_0 r_{i\alpha}} + \sum_{i<}\sum_{j}^{n}\frac{e^2}{4\pi\varepsilon_0 r_{ij}} \qquad (2.2)$$

The three terms contributing to the electronic Hamiltonian in equation 2.2 are the electronic kinetic energy, where n is the number of electrons in the system, a second term which involves the electron-nuclear attraction energy, where N refers to nuclei, with the final term representing inter-electron repulsion. Simplification can be achieved by working in so-called 'atomic units', the bohr, a_0, for length and the hartree, E_h, for energy.

$$a_0 = \frac{h^2 \varepsilon_0}{\pi m_e e^2} \qquad E_h = \frac{e^2}{4\pi\varepsilon_0 a_0} \tag{2.3}$$

This allows equation 2.2 to be greatly simplified to

$$\hat{H} = \sum_{i=1}^{n} -\frac{1}{2}\nabla_i^2 - \sum_{i=1}^{n}\sum_{\alpha=1}^{N}\frac{Z_\alpha}{r_{i\alpha}} + \sum_{i<j}\sum\frac{1}{r_{ij}} \tag{2.4}$$

The wavefunction can be approximated in terms of one electron functions (orbitals), ϕ. In it's simplest form, this approach yields the Hartree product.

$$\Psi(\mathbf{r}_1, \mathbf{r}_2, \ldots \mathbf{r}_n) = \phi_1(\mathbf{r}_1)\phi_2(\mathbf{r}_2)\ldots\phi_n(\mathbf{r}_n) \tag{2.5}$$

The Hartree product does not, however provide an acceptable wavefunction, because it fails to conform to the Pauli principle, a generalised expression of the exclusion principle, which demands that an acceptable wavefunction must be antisymmetric with respect to exchange of the co-ordinates of any pair of electrons. Electronic spin, which can take the values of ±½, must be accounted for by the inclusion of a spin function, α or β, forming a spin orbital from a spatial orbital (a one-electron function defined uniquely by a set of co-ordinates). An additional property of the wavefunction requires that the electrons be indistinguishable. After the electron exchange criteria, electronic spin, and indistinguishability of the electrons are included, the most convenient method of

expressing the resulting representation of the wavefunction is *via* a Slater determinant[4], shown in equation 2.6, where $\frac{1}{\sqrt{n!}}$ is a normalisation factor.

$$\Psi = \frac{1}{\sqrt{n!}} \begin{vmatrix} \phi_1(\mathbf{r}_1)\alpha(1) & \phi_1(\mathbf{r}_1)\beta(1) & \phi_2(\mathbf{r}_1)\alpha(1) & \cdots & \phi_{\frac{n}{2}}(\mathbf{r}_1)\beta(1) \\ \phi_1(\mathbf{r}_2)\alpha(2) & \phi_1(\mathbf{r}_2)\beta(2) & \phi_2(\mathbf{r}_2)\alpha(2) & \cdots & \phi_{\frac{n}{2}}(\mathbf{r}_2)\beta(2) \\ \phi_1(\mathbf{r}_3)\alpha(3) & \phi_1(\mathbf{r}_3)\beta(3) & \phi_2(\mathbf{r}_3)\alpha(3) & \cdots & \phi_{\frac{n}{2}}(\mathbf{r}_3)\beta(3) \\ \vdots & \vdots & \vdots & \ddots & \vdots \\ \phi_1(\mathbf{r}_n)\alpha_n(n) & \phi_1(\mathbf{r}_n)\beta(n) & \phi_2(\mathbf{r}_n)\alpha(n) & \cdots & \phi_{\frac{n}{2}}(\mathbf{r}_n)\beta(n) \end{vmatrix} \qquad (2.6)$$

The indistinguishability is incorporated by allowing the permutation of every electron into every spin orbital (the above expression assumes there are n electrons in n/2 spatial orbitals). The use of a determinant has the inherent property of incorporating antisymmetry. The exchange of a pair of electrons corresponds to an interchange of two rows within the determinant, which necessarily causes a change of sign.

The simplification of reducing the insoluble many-body problem to a series of single-body problems was suggested by Hartree[5] and Fock[6]. In this formulation, the energy of the molecular system is given as a sum of single electron and inter-electronic terms,

$$E = \sum_{i=1}^{\frac{n}{2}} 2h_{ii} + \sum_{i=1}^{\frac{n}{2}} \sum_{j=1}^{\frac{n}{2}} \left(2J_{ij} - K_{ij}\right) \qquad (2.7)$$

where h_{ii} are one-electron contributions to the energy. J_{ij} is the energy due to Coulomb interactions between electrons (a local effect), with K_{ij}, a purely quantum term having no

classical interpretation, giving non-local exchange contributions to the energy. h_{ii}, and the integrals J_{ij} and K_{ij} are given by

$$h_{ii} = \int \phi_i^*(1)\left(-\frac{1}{2}\nabla_i^2 - \sum_{\alpha=1}^{N}\frac{Z_\alpha}{r_{1\alpha}}\right)\phi_i(1)\, d\tau_1 \qquad (2.8)$$

$$J_{ij} = \int \phi_i^*(1)\phi_j^*(2)\frac{1}{r_{12}}\phi_i(1)\phi_j(2)\, d\tau_{12} \qquad (2.9)$$

$$K_{ij} = \int \phi_i^*(1)\phi_j^*(2)\frac{1}{r_{12}}\phi_i(2)\phi_j(1)\, d\tau_{12} \qquad (2.10)$$

From the variational principle, the best wavefunction is that which has the lowest energy. This is central to the computational solution of the Hartree-Fock equations as it provides an unambiguous criterion by which the quality of the wavefunction can be judged. This can be expressed as

$$E = \frac{\int \Phi^* \hat{H} \Phi\, d\tau}{\int \Phi^* \Phi\, d\tau} \qquad (2.11)$$

It can thus be shown that there are n/2 Schrödinger-like equations of the form

$$\hat{F}_i(1)\phi_i(1) = \varepsilon_i\phi_i(1) \qquad (2.12)$$

Where $\hat{F}_i(1)$ is the Fock operator, and $\phi_i(1)$ and ε_i are the i'th orbital and the corresponding energy, respectively.

$$\hat{F}_i(1) = -\frac{1}{2}\nabla_1^2 - \sum_a^N \frac{Z_a}{r_a} + \sum_j^{\frac{n}{2}}\left[2\hat{J}_j(1) - \hat{K}_j(1)\right] \qquad (2.13)$$

2.2.2 - The Roothaan-Hall equations

The computational solution of the Hartree-Fock equations for molecular systems relies upon the expansion of the orbitals, ϕ_i, in terms of a linear combination of atomic orbitals (LCAO), suggested by Roothaan[7] and Hall[8],

$$\phi_i = \sum_{\mu=1}^{m} c_{\mu i}\chi_\mu \qquad (2.14)$$

Substituting this expansion into equation 2.12 gives

$$\hat{F}\sum_{\mu} c_{\mu i}\chi_\mu = \varepsilon_i \sum_{\mu} c_{\mu i}\chi_\mu \qquad (2.15)$$

Multiplication by another basis function, χ_p and integration gives rise to the secular equations

$$\sum_{\nu=1}^{N}\left(F_{\mu\nu} - \varepsilon_i S_{\mu\nu}\right)c_{\nu i} = 0 \qquad (2.16)$$

where ε_i are the orbital eigenvalues (energies). The solution of the Roothaan-Hall equations then reduces to

$$FC = SC\varepsilon \qquad (2.17)$$

where F is the Fock matrix, S the overlap matrix in the atomic orbital basis and ε a diagonal matrix of orbital eigenvalues (energies). An element of F is given by

$$F_{\mu\nu} = H_{\mu\nu}^{core} + \sum_{\lambda=1}^{N}\sum_{\sigma=1}^{N} P_{\lambda\sigma}\left[(\mu\nu|\lambda\sigma) - \frac{1}{2}(\mu\lambda|\nu\sigma)\right] \qquad (2.18)$$

where

$$F_{\mu\nu} = \int \chi_\mu \hat{F} \chi_\nu \, d\tau \qquad (2.19)$$

$$H_{\mu\nu}^{core} = \int \phi_{\mu}^{*}(1)\left[-\frac{1}{2}\nabla^2 - \sum_{a=1}^{N}\frac{Z_a}{r_{1a}}\right]\phi_{\nu}\, d\tau \qquad (2.20)$$

and $P_{\lambda\sigma}$ the density matrix, defined as

$$P_{\lambda\sigma} = 2\sum_{i=1}^{occupied} c_{\lambda i}c_{\sigma i} \qquad (2.21)$$

In equation 2.18, $(\mu\nu|\lambda\sigma)$ and $(\mu\lambda|\nu\sigma)$ are the two-electron repulsion integrals, defined as

$$(\mu\nu|\lambda\sigma) = \int \chi_{\mu}(1)\chi_{\nu}(1)\frac{1}{r_{12}}\chi_{\lambda}(2)\chi_{\sigma}(2)\, d\tau_{12} \qquad (2.22)$$

$$(\mu\lambda|\nu\sigma) = \int \chi_{\mu}(1)\chi_{\lambda}(1)\frac{1}{r_{12}}\chi_{\nu}(2)\chi_{\sigma}(2)\, d\tau_{12} \qquad (2.23)$$

Since the Fock matrix elements depend upon the coefficients of the orbitals, solution of the Roothaan-Hall equations relies on the use of an iterative scheme. An initial guessed set of coefficients is used to determine the elements of the Fock matrix, resulting in an improved set of orbitals which are successively refined until they remain unchanged. At this point, the orbitals are said to be self-consistent, giving rise to the name self-consistent field (SCF) procedure.

2.3 - Basis sets and orbitals

Within the LCAO formalism detailed above, the i'th molecular orbital is described in terms of a linear combination of atomic orbitals.

$$\phi_i = \sum_{\mu=1}^{n} c_{\mu i}\chi_\mu \qquad (2.24)$$

where μ references the atomic orbital and $c_{\mu i}$ is the corresponding coefficient. The atomic orbitals, which in their simplest form are solutions of the Schrödinger equation for an atomic system, were originally expressed in terms of Slater functions[9].

$$\phi_i(\zeta,n,l,m;r,\theta,\phi) = Nr^{n-1}e^{-\zeta r}Y_{lm}(\theta,\phi) \qquad (2.25)$$

Here N is a normalisation constant, n, l and m the principal, angular momentum and magnetic quantum numbers respectively. r,θ,ϕ are a set of spherical co-ordinates, ζ an exponent and Y_{lm} the spherical harmonic. Whilst Slater functions do provide an excellent representation of atomic orbitals, they are very difficult functions in which to evaluate two-electron integrals. Boys[10] suggested an alternative approach in which sets of carefully chosen Gaussian functions with differing exponents and coefficients were used. The exponents and coefficients of the primitives are obtained by energy minimisation within atomic calculations. Very efficient methods have since been developed by which two electron integrals over Gaussian functions can be rapidly evaluated. Even though many such primitive Gaussian functions are required to convincingly represent an atomic orbital, the ease of integration provides a significant advantage compared to the use of Slater orbitals. Gaussian functions, in a Cartesian co-ordinate system, are of the form

$$g(\alpha,l,m,n;x,y,z) = Ne^{-ar^2}x^l y^m z^n \qquad (2.26)$$

As before, N is a normalisation constant, α an exponent and x,y,z Cartesian co-ordinates. Here l, m and n are integral exponent values which determine the angular form of the functions.

The combination of a number of these primitive Gaussian functions is referred to as a contraction. The nomenclature adopted by Pople to describe his widely used basis sets, with which all calculations in this thesis were performed, is particularly illuminating in explaining the use and derivation of contractions. The 6-31G basis set[11] uses a contraction of 6 primitive Gaussian functions to describe the core shells, with the valence shell represented by two contractions, one of 3 primitive Gaussians and another of a single primitive function, respectively. Basis sets of this kind, where 2 contractions are used to define the valence shell, are referred to as valence double zeta sets (DZV). A widely used class of basis sets, also due to Pople, the STO-nG family, the most widely used variant of which is STO-3G[12], in which only single contractions of n primitives are used for all shells, and are referred to as single zeta (SZ) basis sets.

2.3.1 - Polarisation and diffuse functions

In many cases, the quality of the basis set is enhanced by the inclusion of additional basis functions, intended to incorporate a greater degree of variational flexibility. A polarisation function is a basis function with an angular quantum number, l, one greater than the highest value already on the atom - i.e. for carbon at the 6-31G basis set, where the maximum l quantum number is 1 for the p-type functions, the inclusion of a d-type function with l=2 would be denoted 6-31G* using the Pople nomenclature. A second asterisk shows the additional inclusion of p-type polarisation functions on hydrogen. A complication arises with the 3-21G basis set, in which polarisation functions are not conventionally added to first row elements. The partially polarised nature of this

basis set will be represented in this thesis by including parentheses around the asterisk associated with the heavy atom - i.e. 3-21G(*).

The accurate modelling of anionic systems is found to be greatly dependent on the correct representation of the more diffuse electronic distribution. To achieve this, it is necessary to supplement the standard basis set description with basis functions having smaller exponents (more diffuse functions) than those of the standard basis set. Again using the Pople system, this is denoted 6-31+G for a basis set in which the heavy atoms include diffuse functions and 6-31++G where the hydrogen atom basis also includes diffuse functions.

2.4 - Geometry Optimisation methods

Within standard molecular SCF codes, the optimisation of geometrical parameters is accomplished by determining the first derivative of the energy with respect to nuclear co-ordinates. Whilst this can be accomplished by finite-differences, very efficient analytical algorithms have been developed which allow the evaluation of both first and second derivatives of the energy with respect to nuclear co-ordinates. Even so, complete investigation of the multi-dimensional potential energy surface of molecules having large numbers of degrees of freedom, such as those studied here, is generally impractical. Thus, it is not typically possible to ensure that the energy minimum reached is the global one. More typically, a local minimum dependent on the starting geometry used, is obtained.

Minima are points on the potential energy surface from which any geometrical displacement is accompanied by a rise in energy. Thus, a minimum can only be fully characterised by a consideration of the second derivatives of the energy with respect to nuclear positions, where all eigenvalues of the second derivative matrix will be positive. Situations in which there are negative eigenvalues of the second derivative matrix correspond to stationary points on the potential energy surface which are minima in most directions, but maxima in one or more others. For the simplest case where a single displacement is a maximum, termed a first order saddle point or transition state, a path exists which passes through the transition state, connecting two lower energy minima. Similarly for higher order saddle points, maxima in more than one direction, many distinct paths to minima of lower energy may exist.

2.5 - Electronic correlation and density functionals

2.5.1 - Møller-Plesset perturbation theory

The basis of this approach is that perturbation theory (Rayleigh-Schrödinger theory) can be used to incorporate higher excitations into the Hartree-Fock wavefunction. The first stage is to express the Hamiltonian operator as

$$\hat{H} = \hat{H}_0 + \lambda V \qquad (2.27)$$

where V is a small perturbation in relation to $\hat{H}_0$ (the unperturbed Hamiltonian) and λ is an arbitrary parameter. If V is sufficiently small, both the energy and wavefunction can be expressed as power series

$$\Psi = \Psi^{(0)} + \lambda\Psi^{(1)} + \lambda^2\Psi^{(2)} + \ldots \qquad (2.28)$$

$$E = E_0 + \lambda E^{(1)} + \lambda^2 E^{(2)} + \ldots \qquad (2.29)$$

where $\lambda^n\Psi^{(n)}$ and $\lambda^n E^{(n)}$ are the n'th order corrections to the wavefunction and energy, respectively. Substitution for $\hat{H}$, Ψ and E into equation 2.1 gives

$$\left(\hat{H}_0 + \lambda V\right)\left(\Psi^{(0)} + \lambda\Psi^{(1)} + \ldots\right) = \left(E^{(0)} + \lambda E^{(1)} + \ldots\right)\left(\Psi^{(0)} + \lambda\Psi^{(1)} + \ldots\right) \qquad (2.30)$$

Within Møller-Plesset[13] theory the unperturbed Hamiltonian, $\hat{H}_0$ is given as the sum of one-electron Fock operators, with $E^{(0)}$ given as the sum of orbital eigenvalues

$$\hat{H}_0 = \sum_{i=1}\hat{F}_i \qquad E^{(0)} = \sum_i \varepsilon_i \qquad (2.31)$$

The zero order energy and first order correction simply gives the ground state Hartree-Fock energy. In a similar manner, the zero order wavefunction is simply the Hartree-Fock ground state wavefunction.

It should be noted that whilst Møller-Plesset corrections are size consistent, they are not variational and a Møller-Plesset calculation does not lead to a meaningful wavefunction. Successive corrections to the energy, the most commonly applied of which is that at second order, can be derived by expanding equation 2.30 and expressing in terms of the desired order. For the second order correction, it can be shown that

$$\left(\hat{H}^{(0)} - E^{(0)}\right)\Psi^{(2)} = E^{(2)}\Psi^{(0)} + \left(E^{(1)} - V\right)\Psi^{(1)} \qquad (2.32)$$

With the second order correction to the energy obtained as

$$E^{(2)} = \sum_t \frac{\int \Psi^{(0)} V \Psi_t^{(0)}\, d\tau \int \Psi^{(0)} V \Psi_t^{(0)}\, d\tau}{E^{(0)} - E_t^{(0)}} \qquad (2.33)$$

where $\Psi_t^{(0)}$ is an arbitrary substituted wavefunction.

The use of Møller-Plesset theory within small molecule calculations has become routine, with MP2 first and second derivatives implemented in standard Hartree-Fock codes. The use of higher order Møller-Plesset corrections, usually to MP4, is also common, though generally restricted to relatively small systems.

2.5.2 - Density functional methods

In density functional theory (DFT), the charge density, ρ, is used as the variable which describes all ground state properties of the molecular system. The total energy of the system, E_{total}, is defined as a functional of ρ.

$$E_{total} = T[\rho] + U[\rho] + E_{xc}[\rho] \qquad (2.34)$$

Where $T[\rho]$ is the kinetic energy of the system of non-interacting particles of density ρ, $U[\rho]$ the classical Coulomb energy and $E_{xc}[\rho]$ a many-body term which includes all exchange and correlation effects. The so-called 'Kohn-Sham'[14] equations, single-particle Schrödinger equations, can be formulated by varying E_{total} with respect to ρ, which can then be solved in an iterative manner. The exchange functional used in this thesis is that due to Becke[15].

Whilst equation 2.34 is formally exact, no exact solutions are presently known for $E_{xc}[\rho]$. The local density approximation (LDA) is applied, where for an inhomogeneous

molecular charge density, ρ, the single particle exchange-correlation energy, ε_{xc}, is integrated over all space using a form of ε_{xc} which gives the exact solution to the homogeneous electron gas problem.

$$E_{xc}[\rho] \approx \int \rho(\mathbf{r})\, \varepsilon_{xc}[\rho(\mathbf{r})]\, d\mathbf{r} \qquad (2.35)$$

Corrections are typically applied to modify the non-local effects badly represented within the LDA. The non-local correction applied in conjunction with the Becke exchange functional is that due to Lee, Yang and Parr[16]. The widely used combination of the Becke exchange functional with the Lee Yang and Parr non-local correction is denoted B-LYP, nomenclature which will also be used in this thesis. The B-LYP functional, as used in this thesis, is implemented in a code developed at Manchester[17], within the GAUSSIAN 92 package[18]. Whilst density functional methods are somewhat computationally expensive, their cost is competitive with energy evaluations at the MP2 level, with substantially less memory and disk overhead. An additional advantage is the scaling of DFT calculations with molecular size, which is substantially less restricting than using perturbative methods, and limited more by the number of atoms than the number of basis functions.

2.6 - Periodic Hartree-Fock theory

2.6.1 - Introduction

The implementation of Hartree-Fock theory with a crystalline orbital basis set, subject to periodic boundary conditions, can be accomplished with equal validity using either a direct space or momentum space formulation. The approach described here, as implemented within the CRYSTAL[19] program of Pisani, Dovesi, and Roetti, is essentially a direct space implementation, in which many aspects of traditional molecular Hartree-Fock theory (described in section 2.2) are paralleled. Whilst a full discussion of the techniques utilised in facilitating periodic Hartree-Fock (PHF) calculations is beyond the scope of this thesis, a brief exposition of the general approach as well as the relative importance of the approximations necessary to make such calculations tractable are described. CRYSTAL 92 was used for all periodic Hartree-Fock calculations in this thesis.

2.6.2 - CRYSTAL 92

The use of CRYSTAL 92 is central to the subsequent work in this thesis, and a brief consideration of the operation and construction of the program is warranted. CRYSTAL is a suite of three large, separate codes, *integrals*, *scf* and *properties*, typically run serially, which would be used in the following way for a typical calculation:

(a) First run *integrals*, which takes the input file containing the geometry data in fractional co-ordinates, the computational parameters (including the basis set or pseudopotential input) and a series of user-definable options. The code then performs any geometrical manipulations which are required, determining the new symmetry of the system, if appropriate. The majority of the time within this code is spent evaluating the mono and bi-electronic integrals, with very efficient selection schemes for determining which integrals must be exactly evaluated and which need only be approximated. The one and two-electron integrals are then written to separate disk files. For zeolite calculations, the files are routinely of the order 1-2Gb for the one-electron integrals, and several times this size for two-electron integrals. For this reason, supercomputer resources were required for most of these calculations.

(b) Run *scf* which picks up the pre-calculated integrals and performs the self-consistent field calculation. When the user-defined convergence criteria are met, the wavefunction data are written to an external file. A direct SCF version of CRYSTAL exists, in which the operations of *integrals* and *scf* are combined within a single executable module, with the two-electron integrals calculated at every iteration of the SCF. The more modest disk space requirements of only storing the relatively small one-electron integral file mean reasonably large calculations can now be performed on workstations.

(c) From the converged wavefunction, the user can calculate a large number of properties of the system. An additional input deck is required to run *properties*, in the form of a list of keywords, executed sequentially. The version of *properties* used in this thesis was modified to allow the evaluation of electrostatic potentials and electron densities at an arbitrary, user-defined list of points.

2.6.3 - Basis functions and orbitals

In contrast to standard molecular techniques, the study of periodic systems has seen a great variety of different approaches, which are dictated fundamentally by the initial choice of basis functions. Discussion of the functional forms chosen for the basis functions within CRYSTAL 92 is necessary as it highlights the salient features of the approach, which influence all subsequent areas of the implementation.

(i) As in the molecular case, the orbitals used must be eigenfunctions of the one-electron Hamiltonian, but for an efficient periodic scheme, the orbitals used, crystal orbitals (CO), must make maximum use of the translational symmetry inherent in the crystal. The first step is to define the local atomic orbital basis as

$$\chi_{\alpha}^{\mathbf{g}}(\mathbf{r}) \equiv \chi_{\{n,l,m\}}(\mathbf{r}-\mathbf{g}-\mathbf{s}_{\alpha}) \qquad (2.36)$$

Where $\mathbf{g}$ is a vector referencing the general cell, α denotes the α'th atomic orbital in that cell and $\mathbf{r}$ the position at which the wavefunction is to be evaluated. The subscript $\{n,l,m\}$ refers to the quantum numbers which characterise the atomic orbital and $\mathbf{g}-\mathbf{s}_{\alpha}$ represents a 'fractional' vector which references the position of the atom. The atomic orbitals are then expressed in a form which incorporates the translational symmetry of the periodic system, using a momentum-space formulation in terms of Bloch functions, where $\mathbf{k}$ is a wave vector.

$$\phi_{\alpha k} = \sum_{g} e^{ik.g} \chi_{\alpha}^{g}(\mathbf{r}) \qquad (2.37)$$

The crystal orbitals are then expressed in terms of linear combinations of the Bloch functions, where $c_{n\alpha}^{(k)}$ is a variational coefficient.

$$\varphi_{nk} = \sum_{\alpha} c_{n\alpha}^{(k)} \phi_{\alpha k} \qquad (2.38)$$

(ii) Bloch functions, rather than plane-waves, are used as the functional form for the basis sets within this implementation of PHF theory as a result of the benefits that result from their ease of expression in terms of atom-centred local functions. It should be noted that plane-wave implementations do exist, and have the distinct advantage that a single plane wave provides the exact solution to the homogeneous electron gas problem, the archetype for all solid-state studies.

(iii) The atom centred local functions are expanded, as in the molecular case, in terms of CGTF (contracted Gaussian type functions). In this manner, maximum use can be made of highly efficient molecular Hartree-Fock integral generation techniques and proven basis sets. The incorporation of diffuse functions is not, however appropriate within periodic Hartree-Fock calculations as their substantial overlap cause unacceptable increase in the number of integrals to be evaluated. The more contracted nature of the orbitals within periodic systems, however, means standard molecular basis sets lie closer to the Hartree-Fock limit when applied within a periodic context.

2.6.4 - Computational approach

A typical periodic Hartree-Fock calculation within the CRYSTAL program, can be broken down into the following series of steps:

(i) First, construct the Fock matrix in direct space. The terms which contribute are the same as those of standard molecular Hartree-Fock theory. The general element, $\mathbf{F}_{12}^{\mathbf{g}}$, where $\mathbf{g}$ denotes a direct lattice vector by which a given unit cell is referenced, is given by

$$\mathbf{F}_{12}^{\mathbf{g}} = \mathbf{T}_{12}^{\mathbf{g}} + \mathbf{Z}_{12}^{\mathbf{g}} + \mathbf{C}_{12}^{\mathbf{g}} + \mathbf{X}_{12}^{\mathbf{g}} \qquad (2.39)$$

Where $\mathbf{T}_{12}^{\mathbf{g}}$ is the kinetic energy matrix, $\mathbf{Z}_{12}^{\mathbf{g}}$ and $\mathbf{C}_{12}^{\mathbf{g}}$ are the interactions of the AO overlap distribution, $\chi_1^{\mathbf{g}}(\mathbf{r})\chi_2^{\mathbf{g}}(\mathbf{r})$, with the full nuclear and electronic charge distributions respectively (in overlap distributions, superscripts refer to the cell in which the AO is located, $\mathbf{0}$ indicating the reference cell). Expressing the Coulomb component, $\mathbf{C}_{12}^{\mathbf{g}}$, of the Fock matrix in the concise notation of Pisani, Dovesi and Roetti[1]

$$\mathbf{C}_{12}^{\mathbf{g}} = \sum_{\lambda} \left(\{12\mathbf{g}\} | \{\lambda;\mathbf{T}\} \right) \qquad (2.40)$$

where, $\{12\mathbf{g}\}$, equivalent to $\{1\mathbf{0}\ 2\mathbf{g}\}$, is simply the overlap $\chi_1^{\mathbf{0}}(\mathbf{r})\chi_2^{\mathbf{g}}(\mathbf{r})$, it is clear that the charge distributions $\chi_1^{\mathbf{0}}$ and $\chi_2^{\mathbf{g}}$ are located in different cells, a complicating factor not present in molecular Hartree-Fock theory. Within the $\{\lambda;\mathbf{T}\}$ term, the Mulliken scheme[20] is used to produce a shell expansion of charges, with the shell charge denoted by λ. $\mathbf{T}$ denotes a sum over the infinite set of $\mathbf{h}$ vectors.

In equation 2.39, the $\mathbf{X}_{12}^{g}$ term is the exchange contribution to the Fock matrix, given by

$$\mathbf{X}_{12}^{g} = -\frac{1}{2}\sum_{34n}\mathbf{P}_{34}^{n}\left[\sum_{h}\left(\mathbf{10\ 3h}\middle|\mathbf{2g\ 4n+h}\right)\right] \qquad (2.41)$$

The two summations in the above equation, over indices **h** and **n**, are extended to include all direct lattice vectors. It is clear that each of the basis functions in the above equation can be formally located over four centres which can each be in different cells, another feature which has no counterpart in standard Hartree-Fock theory.

The energy per cell can be expressed as a sum of the following terms

$$\mathbf{E} = \mathbf{E}_{k} + \mathbf{E}^{ex} + \mathbf{E}^{c} \qquad (2.42)$$

Where $\mathbf{E}_{k}$ is the kinetic energy, $\mathbf{E}^{ex}$ the exchange energy and $\mathbf{E}^{c}$ the Coulomb term. These individual terms are given by

$$\mathbf{E}_{k} = \sum_{12g}\mathbf{P}_{12}^{g}\mathbf{T}_{12}^{g} \qquad (2.43)$$

$$\mathbf{E}^{ex} = \frac{1}{2}\sum_{12g}\mathbf{P}_{12}^{g}\mathbf{X}_{12}^{g} \qquad (2.44)$$

$$\mathbf{E}^{c} = \mathbf{E}_{ee}^{c} + \mathbf{E}_{en}^{c} + \mathbf{E}_{ne}^{c} + \mathbf{E}_{nn}^{c} \qquad (2.45)$$

With the bielectronic component of $\mathbf{E}^{c}$, $\mathbf{E}_{ee}^{c}$, given by

$$\mathbf{E}_{ee}^{c} = \sum_{12g}\mathbf{P}_{12}^{g}\left\{\sum_{34n}\mathbf{P}_{34}^{n}\left[\sum_{h}\left(\left\{\mathbf{10\ 2g}\middle|\mathbf{3n\ 4n+h}\right\}\right)\right]\right\} \qquad (2.46)$$

A problem arises because the individual electron-nuclear, electron-electron and nuclear-nuclear terms in the Coulomb summation are divergent when considered in isolation, and the sum as a whole is only conditionally convergent. If, however, the Coulomb lattice sum is evaluated using the method of Ewald[21], rapid and unconditional convergence can be enforced. However, a recent reformulation of periodic Hartree-Fock theory by Hammes-Schiffer and Andersen[22] allows all series contributing to Fock matrix

elements to be expressed in an unconditionally convergent form, with terms which correspond closely to those of standard molecular Hartree-Fock theory. Such a formulation would allow the direct incorporation of many post Hartree-Fock techniques, particularly perturbative correlation corrections, directly from molecular Hartree-Fock theory.

(ii) The reciprocal space analogue of the direct space Fock matrix is generated at a number of points in **k** space using Fourier transform and antitransform relations which interconvert direct space Fock matrix elements and their reciprocal space counterparts, shown in equations 2.47 and 2.48. In equation 2.47, V_B is the volume of the first Brillouin zone (The Wigner-Seitz cell of a reciprocal lattice point)[23].

$$\mathbf{F}_{12}^{\mathbf{g}} = \frac{1}{V_{\mathrm{B}}} \int_{\mathrm{BZ}} d\mathbf{k}\, \mathbf{F}_{12}(\mathbf{k}) \mathrm{e}^{-\mathrm{i}\mathbf{k}.\mathbf{g}} \qquad (2.47)$$

$$\mathbf{F}_{12}(\mathbf{k}) = \sum_{\mathbf{g}} \mathbf{F}_{12}^{\mathbf{g}} e^{i\mathbf{k}.\mathbf{g}} \qquad (2.48)$$

Considerable efforts have been made into determining efficient schemes for the evaluation of the minimal set of points at which diagonalisation must occur for correct convergence. It has been shown that the reciprocal space Fock matrix need only be diagonalised at **k** points within the irreducible part of the first Brillouin zone (IBZ)[1]. The Monkhorst net scheme[24,25] is used for allocation of **k** points in CRYSTAL. In this scheme, the set $\{\mathbf{k}_i\}$ of **k** points, are generated by choosing 'shrinking factors' by which the reciprocal lattice vectors are subdivided. The basis vectors are given by $\mathbf{b}_1/s_1$, $\mathbf{b}_2/s_2$ and $\mathbf{b}_3/s_3$, where $\mathbf{b}_1$, $\mathbf{b}_2$ and $\mathbf{b}_3$ are the standard reciprocal lattice vectors, and s_1, s_2 and s_3 are the integral shrinking factors. For typical cases, it is usual to set s_1=s_2=s_3. In the

case of periodic systems which have large unit cells and relatively low symmetry (*viz.* zeolites considered in this thesis), the number of **k** points which need to be considered is small. At each of the **k** points in the set $\{\mathbf{k}_i\}$, the following relation holds

$$\mathbf{F}(\mathbf{k})\mathbf{A}(\mathbf{k}) = \mathbf{S}(\mathbf{k})\mathbf{A}(\mathbf{k})\mathbf{E}(\mathbf{k}) \qquad (2.49)$$

Where $\mathbf{A}(\mathbf{k})$ is the matrix of eigenvectors and $\mathbf{E}(\mathbf{k})$ the corresponding diagonal matrix of eigenvalues for the crystal orbitals.

(iii) Generate the reciprocal space density matrix using the following relation

$$\mathbf{P}_{12}(\mathbf{k}) = 2\sum_{j} a_{1j}^{*}(\mathbf{k}) a_{2j}(\mathbf{k})\, \Theta\left[\varepsilon_F - \varepsilon_j(\mathbf{k})\right] \qquad (2.50)$$

In equation 2.50, $\Theta$is the Heaviside step function and ε_F the Fermi energy term which is determined *via* a reciprocal space integration scheme, in which the energy-dependent total density of states, DOS, is expressed as a sum of the DOS of each of the constituent bands of the system, which are then expanded in terms of Legendre polynomials, with the **k** dependent properties, eigenvalues and eigenvectors, expressed as Fourier series. In the case of insulating systems, the bands are either fully occupied or empty. As a result, equation 2.50 can be reduced to a simple weighted sum at the set $\{\mathbf{k}_i\}$ of **k** points, with the j summation including only occupied bands, with geometric weights w_i.

Using the value of ε_F, a new direct space density matrix, $\mathbf{P}_{12}^{g}$, is defined

$$\mathbf{P}_{12}^{g} = 2\sum_{n} \int_{BZ} d\mathbf{k}\, e^{i\mathbf{k}g} a_{1n}^{*}(\mathbf{k}) a_{2n}(\mathbf{k})\, \Theta\left[\varepsilon_F - \varepsilon_n(\mathbf{k})\right] \qquad (2.51)$$

(iv) Define a new direct space Fock matrix.

(v) Go to (i) and iterate in a self-consistent manner until convergence criteria are met.

2.6.5 - Approximate methods

The basic formulation, as described above, would prove computationally untenable due to the extremely large number of integrals to be evaluated and the formally infinite nature of the coulomb sums. It is therefore inevitable that any realistic implementation must incorporate substantial approximations. However, the application of approximations must not unduly affect the results of the scheme, so a delicate balance must be struck between the computational cost of the calculation and the desired accuracy.

The primary approximation applied is a spatial partitioning scheme in which the **h** space in the Coulomb term, equation 2.46, is subdivided into a small 'bielectronic zone' where the large overlap of the interacting charge distributions forces the exact evaluation of the associated overlap integral and a 'monoelectronic zone', encompassing all regions of space complementary to the bielectronic zone, in which the overlap integral can be approximated *via* a rapid bipolar scheme, or neglected.

Whilst CRYSTAL can be treated largely as a 'black box', in the same way as most molecular Hartree-Fock codes, two additional sets of parameters, not required in the molecular case, must also be supplied as part of the input for the calculation.

(i) The first set, computational parameters ITOL 1 to 5, are designed to affect the relative sizes of the monoelectronic and bielectronic zones, and the balance between the number of integrals which are calculated exactly and those which are approximated. More specifically, ITOL 1 is used to control the selection of bielectronic integrals by discarding any integral in which the total charge associated with a given overlap distribution (in terms of adjoined Gaussians) is smaller than a user defined tolerance, S_c, where $\mathrm{ITOL}1 = -\log S_c$. ITOL 2 controls the spatial partitioning scheme, assigning overlaps to either the approximated or exact regions, based on the penetration, $S_{1\lambda}$, between an overlap distribution ρ_1 and the shell charge distribution ρ_λ. If $ITOL2 > -\log S_{1\lambda}$, ρ_λ is assigned to the exact region.

ITOL parameters, 3 to 5 are involved in the truncation of the exchange series. More specifically, since there is an exponential decrease in the overlap $\chi_1^{\mathbf{0}}(\mathbf{r})\chi_3^{\mathbf{h}}(\mathbf{r})$ with increasing **h**, the **h** summation can be truncated at a specific value if the charges associated with the adjoined Gaussians, $q_1 = \{G_1^{\mathbf{0}} G_3^{\mathbf{h}}\}$ or $q_2 = \{G_2^{\mathbf{g}} G_4^{\mathbf{n+h}}\}$ are less than $10^{-\mathrm{ITOL}3}$. In a similar manner, ITOL 4 and ITOL 5 are used to truncate the **g** and **n** summations. Although their behaviour is more complex than the case of **h** summation, the same basic approach still holds.

(ii) Choice of the parameters controlling the reciprocal space aspects of the calculation, particularly the diagonalisation of the reciprocal space Fock matrix and the integration scheme used to determine the Fermi energy, ε_F, is especially important. The sensitivity of correct wavefunction convergence has been shown to be strongly affected by the choice of the shrinking factors defining the Monkhorst net and thus, the set of **k**

points at which the reciprocal space Fock matrix is diagonalised. However, in the case of systems which have large unit cells and relatively low symmetry (e.g. zeolitic systems studied in this thesis), the number of $\mathbf{k}$ points at which the Fock matrix must be diagonalised is small.

The important parameters which control the reciprocal space aspects of the calculation are RTOL1, RTOL2 and RTOL3, where RTOL1 is the integral shrinking factor in reciprocal space from which the Monkhorst net is generated. RTOL2 determines the number of plane waves used in the expansion of the $\varepsilon(\mathbf{k})$ function and RTOL3 the shrinking factors by which the Gilat net, used in the determination of ε_F, is generated. Special consideration of RTOL2 and RTOL3 is only necessary in the case of conducting systems, otherwise it is reasonable to set RTOL1=RTOL2=RTOL3.

2.6.6 - Periodic electrostatic potentials

As in the molecular case, the quantum mechanical electrostatic potential, $V(\mathbf{r})$, is determined from the electronic charge density, $\rho(\mathbf{r})$, of the converged wavefunction. In the molecular case, the potential of a system containing N atoms, at a point $\mathbf{r}$, where Z_i is the nuclear charge of the i'th atom, is given by

$$V(\mathbf{r}) = \sum_{i=1}^{N} \frac{Z_i}{|\mathbf{r}-\mathbf{R}_i|} - \int \frac{\rho(\mathbf{r}')}{|\mathbf{r}-\mathbf{r}'|}\, d\mathbf{r}' \qquad (2.52)$$

Analogously, the potential at a point within the periodic system can be determined *via* the Ewald summation technique. Such an approach is, however is computationally expensive. Using the same spatial partitioning techniques applied to the approximation of

Coulomb integrals, the short range contributions to the electrostatic potential can be evaluated exactly, with longer range contributions evaluated *via* a multipole expansion of the shell charges[26].

$$\rho(\mathbf{r}) = \sum_{\mathbf{h}} \sum_{\lambda} \rho_{\lambda}^{\mathbf{h}} \qquad (2.53)$$

The shell contributions are considered short-range if $e^{\alpha_\lambda(r-s_\lambda-h)} > 10^{-\xi}$, where α_λ is the exponent of the adjoined Gaussian, $\mathbf{s}_\lambda$ is the fractional vector which references the shell λ, and ξ the integral penetration parameter. At high multipole order, e.g. l=6, with an appropriate choice of the penetration parameter, the resulting approximated electrostatic potential is within 0.1 % of the exact value at a substantially lower cost. Throughout this thesis, all periodic electrostatic potentials have been evaluated using the approximate method, using a multipole expansion to order l=6, the maximum permissible, with a penetration parameter of 5.

A problem arises in that the standard molecular definition of the zero value of the electrostatic potential, at an infinite distance from the molecule, is not applicable to a true periodic solid as an infinite displacement is still formally within the crystal. Although methods have been derived which allow the calculation of electrostatic potentials within crystals, the absolute value determined depends on a number of parameters including the summation method used. For this reason, it is frequently the case that electrostatic potentials within periodic systems are 'shifted' to give a zero value at a convenient high symmetry point in the crystal, the centre of a zeolite channel for instance, relative to which all other potentials are reported.

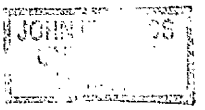

2.7 - References

[1] Pisani, C.; Dovesi, R.; Roetti, C., *"Hartree-Fock Ab Initio Treatment of Crystalline Systems"* Springer-Verlag, New York, **1988**

[2] Schrödinger, E., *Ann. Physik*, **1926**, 79, 361

[3] Born, M.; Oppenheimer, J. R., *Ann. Physik*, **1927**, 84, 457

[4] Slater, J. C., *Phys. Rev.*, **1929**, 34, 1293

[5] Hartree, D. R., *Proc. Cambridge Phil. Soc.*, **1928**, 24, 89

[6] Fock, V., *Z. Physik*, **1930**, 61, 126

[7] Roothaan, C. C. J., *Rev. Mod. Phys.*, **1951**, 23, 69

[8] Hall, G. G., *Proc. Roy. Soc. (London)*, **1951**, A205, 541

[9] Slater, J. C., *Phys. Rev.*, **1930**, 36, 57

[10] Boys, S. F., *Proc. Roy. Soc. (London)*, **1950**, A200, 542

[11] Gordon, M. S.; Binkley, J. S.; Pople, J. A.; Pietro, W. J.; Hehre, W. J., *J. Am. Chem. Soc.*, **1982**, 104, 2997

[12] Hehre, W. J.; Stewart, R. F.; Pople, J. A., *J. Chem. Phys.*, **1969**, 51, 2657

[13] Møller, C.; Plesset, M. S., *Phys. Rev.*, **1934**, 46, 618

[14] Kohn, W.; Sham, L. J., *Phys. Rev.*, **1965**, A140, 1133

[15] Becke, A. D., *Phys. Rev.*, **1988**, A38, 3098

[16] Lee, C.; Yang, N.; Parr, R. G., *Phys. Rev.*, **1988**, B37, 785

[17] Hall, R. J.; Burton, N. A.; Hillier, I. H.; Young, P. E., *Chem. Phys. Lett.*, **1994**, 220, 129

[18] GAUSSIAN 92, Revision A, M. J. Frisch, G. W. Trucks, M. Head-Gordon, P. M. W. Gill, M. W. Wong, J. B. Foresman, B. G. Johnson, H. B. Schlegel, M. A. Robb, E. S. Replogle, R. Gomperts, J. L. Andres, K. Raghavachari, J. S. Binkley, C. Gonzales, R. L. Martin, D. J. Fox, D. J. Defrees, J. Baker, J. J. P. Stewart and J. A. Pople, Gaussian, Inc., Pittsburgh PA, **1992**

[19] Dovesi, R.; Pisani, C.; Roetti, C.; Causa, M.; Saunders, V. R., In Quantum Chemistry Programs Exchange, Publication 577: University of Indiana, **1988**

[20] Mulliken, R. S., *J. Chem. Phys.*, **1955**, 23, 1833, 1841, 2338, 2343

[21] Ewald, P. P., *Ann. Phys.*, **1921**, 64, 253

[22] Hammes-Schiffer, S.; Andersen, H. C., *J. Chem. Phys.*, **1994**, 101, 375

[23] Hall, H. E., *"Solid State Physics"*, Wiley, Chichester, **1987**

[24] Monkhorst, H. J.; Pack, J. D., *Phys. Rev. B.*, **1976**, 13, 5188

[25] Pack, J. D.; Monkhorst, H. J., *Phys. Rev. B.*, **1977**, 16, 1748

[26] Saunders, V. R.; Freyria-Fava, C.; Dovesi, R.; Salasco, L.; Roetti, C., *Mol. Phys.*, **1992**, 629

Chapter 3

Embedded cluster modelling

3.1 - Cluster modelling of zeolites - previous work

Previous studies have acknowledged inadequacies within the standard terminated cluster approach for studies of zeolite catalysis. For their studies on methanol interaction with H-ZSM-5, Vetrivel, Catlow and Colbourn[1,2] suggested a modification to the terminated zeolite cluster model in which a set of point charges, with formal values of +4 for silicon and -2 for oxygen, were placed around a cluster in an attempt to produce a more realistic electrostatic environment in which substrate interactions could be studied. This set of charges was found to cause unphysical polarisation effects and revised halved values of +2 and -1, designed to represent a degree of covalent nature within the zeolite, were used instead. These values are more in keeping with the findings of Mulliken population analysis of small clusters and periodic Hartree-Fock studies[3,4], as well as the intuitive model which suggests zeolite bonding to be more covalent than fully ionic in nature. Whilst this approach was largely empirical, it did acknowledge the problems associated with the accurate representation of zeolite electrostatics within terminated cluster models, and attempted to suggest a remedy.

A more sophisticated modification was subsequently suggested by Kassab, Seiti and Allavena[5], who proposed a scheme in which an attempt was made to produce an accurate reproduction of the Madelung potential within a model of a zeolite cavity. This model used a partitioning of the zeolite into three zones, a region in which an *ab initio* treatment was applied to the zeolite cluster, an intermediate region in which a correction was applied to the terminal regions of the zeolite cluster, and a complementary region in which the Madelung potential was represented by a continuum approach.

A full non-empirical quantum mechanical treatment of the embedding of clusters has been formulated by Pisani, Dovesi, Nada and Kantorovich[6], and implemented within the code EMBED[7]. This perturbed cluster (PC) approach is unlikely to reach widespread utility as the computational demands are of the same order as periodic supercell calculations. Difficulties also arise because SCF convergence can require large numbers of cycles, with considerable sensitivity to the arbitrary selection of the perturbed cluster.

A common problem with the use of small terminated clusters in which there has been no attempt to incorporate modifications to the potential is the tendency for the acidity of the Brønsted site to be severely underestimated. Kramer, van Santen, Emeis and Nowak[8] suggested a scheme in which the acidity of the bridging acidic oxygen site could be tailored by varying the bond lengths of the terminating hydrogens, mimicking the deprotonation energy differences found in real zeolites.

Other than the approaches detailed above, cluster studies of zeolites generally use small, hydrogen terminated clusters and allow the entire cluster to geometry optimise. A review of the use of small cluster models in the study of heterogeneous catalysis is given by Sauer[9]. This approach cannot, however be used to model chemical processes specific to a particular zeolite as the unique structural features of the framework are lost during the optimisation. Other schemes, in which the terminal regions of the cluster are held fixed can be used to circumvent this difficulty, though there is a danger that the inherent flexibility of the zeolite may be repressed.

The primary deficiency in the modelling of zeolites by small cluster models is a reasonable representation of the electrostatic potential within the infinite periodic solid. In this thesis, a simple model designed to correct this major shortcoming is developed, computationally implemented and used to study a range of zeolite-substrate interactions.

3.2 - The embedded cluster model

3.2.1 - Overview of the model

The model we propose is based on the simple premise that a set of correcting charges can be obtained, and used in conjunction with a terminated cluster model, to generate a representation of the zeolite electrostatic potential, which models more closely (than bare clusters) the electrostatic potential derived from a periodic Hartree-Fock calculation. This method attempts to marry the convenience and familiarity of small terminated cluster models with the inclusion of accurate electrostatics derived from periodic *ab initio* calculations. Such an approach is readily incorporated into standard molecular Hartree-Fock codes, *via* the inclusion of point (or ghost) charges. These charges are incorporated into both the Gaussian[10] suite of programs and the GAMESS-UK[11] molecular SCF codes, as classical point charges, and affect only the one-electron terms within the Hamiltonian providing a feasible method of including electrostatic perturbations into molecular calculations at the SCF and post-SCF levels.

The major differences between the electrostatic potential of the periodic crystal and that of the molecular cluster system are due to a combination of the neglect of long-range effects within the molecular model, and problems which arise from the termination procedure. Any successful embedded cluster model must address both problems. The approach we suggest is similar in philosophy to that of Vetrivel, Catlow and Colbourn[1,2], except their empirical formal charges are replaced by a set of charges which are determined so that when added to the cluster potential, the electrostatic potential from a periodic Hartree-Fock calculation is generated.

The relationship between the periodic Hartree-Fock potential, $P_{crystal}$, and the combined potential from the terminated molecular cluster, $P_{cluster}$, and a correcting field of point charges, $P_{charges}$, is simply

$$P_{crystal} = P_{cluster} + P_{charges} \qquad (3.1)$$

or

$$P_{charges} = P_{crystal} - P_{cluster} \qquad (3.2)$$

Thus a set of charges which reproduce the difference between the periodic and cluster potentials, provides a correction to the bare cluster which generates an accurate representation of the periodic Hartree-Fock potential.

3.2.2 - Computational strategy

The series of steps followed in the generation of our embedded cluster model are outlined below. A more detailed consideration of each will subsequently be given.

(i) Select the cluster to be studied.

(ii) Apply a termination procedure to generate a neutral molecular cluster.

(iii) Select the region of space in which accurate electrostatics are required, subsequently referred to as the 'sampling grid'.

(iv) Calculate the electrostatic potential (ESP) in the region defined in (iii) for both the periodic system, $P_{crystal}$, and the terminated molecular cluster, $P_{cluster}$ and subsequently the difference potential $\left(P_{crystal} - P_{cluster}\right)$.

(v) Select a set of points at which the correcting charges are to be sited, hereafter referred to as the 'fitting grid'.

(vi) Calculate values for the correcting charges.

(vii) Embed the cluster in the field of point charges.

Whilst (i) and (ii) would be appropriate for typical bare cluster modelling, stages (iii)-(vii) embody the embedded cluster model, with their novel nature warranting particular comment. From the viewpoint of a zeolite modeller used to bare cluster models, the determination of the point charges will naturally be unfamiliar. However, the model which is generated after (vii), whilst requiring some additional care, is as easily handled as a bare cluster model because of the ease with which point charges are incorporated into molecular SCF codes.

3.2.3 - Cluster selection

A number of criteria must be considered in the selection of the cluster which is to be used in the calculations. As is usual in Hartree-Fock studies, the size of the cluster which can be studied is determined by the basis set chosen and the computational resources available. Another constraint imposed by the method we have suggested is that the correction to the potential from a given set of potential derived charges (PDC) is

only strictly appropriate for the basis set at which the difference potential was evaluated. Thus, the level at which the periodic Hartree-Fock calculation can be carried out largely determines the basis set which can be used for the embedded cluster studies. The possibility does exist, however that charges derived from one basis set may still provide a convincing representation of the zeolite electrostatics when applied in conjunction with another basis set. The degree to which this approach is successful is explored later.

Cluster selection is also influenced by the geometry of the zeolite under study, in that if zeolite-substrate interactions are to be treated, accessibility by the substrate must be considered. In this work, due to computational restrictions, the clusters used contain either 2 or 3 T sites, though the method can be readily extended to larger clusters.

3.2.4 - Cluster termination procedure

It is both desirable and convenient when modelling zeolites *via* small clusters to apply termination procedures to generate neutral molecular clusters. This can be accomplished in a variety of ways[9], though most work uses either Si-H or Si-OH schemes. The approach is based on the concept that the electronic structure of an O-H or Si-H bond is sufficiently close enough to that of an O-Si bond to allow for reasonable modelling. The use of such termination methods is, however likely to cause poor representation of the properties of the infinite zeolite, especially in the cases of small cluster models in which the termination lies close to the region of interest. Examples of T3 clusters using both Si-H and Si-OH termination procedures are shown in figure 3.1, having stoichiometry $Si_3O_4H_8$ and $Si_3O_{10}H_8$, respectively.

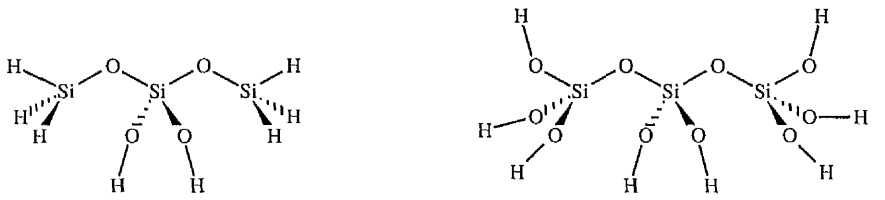

(a) Si-H terminated T3 cluster ($Si_3O_4H_8$). *(b) Si-OH terminated T3 cluster ($Si_3O_{10}H_8$).*

figure 3.1 - Hydrogen terminated T3 clusters.

Rather than unduly compromising the electronic structure in the centre of the Si-H terminated cluster by attaching terminating hydrogen atoms directly to the central silicon, Si-OH termination is retained here.

For reasons of simplicity, coupled with our interest in high-silica zeolites, the periodic Hartree-Fock calculations we have used for the derivation of the point charges have been carried out for purely siliceous forms of the zeolites. The inclusion of aluminium with the corresponding counterions (often sodium) has no benefit within the method we suggest, whilst substantially complicating the periodic calculation as a result of the increased computational demands imposed by the inclusion of metallic species.

Our method assumes additionally that the set of point charges fitted to the all-silica difference potential remain applicable after an aluminium substitution is made into the terminated cluster. The assumption behind this approach is that the substitution of a silicon site by aluminium will have a predominantly local effect, not exerting a substantial polarising influence on more distant T sites, which remain, to a first approximation, the same as for the all-silica zeolite.

3.2.5 - Sampling grid selection

The sampling grid used in the derivation of the set of point charges must necessarily include the whole of the cluster, as it is one of the pre-requisites of the model that the electronic structure within the cluster is reproduced correctly. The terminating atoms, and any region of space inside which an accurate representation of the electrostatic potential is required were both included within the sampling grid. Points in the sampling grid in the vicinity of the termination region are omitted as it is not possible, or desirable, for the potential to be accurately modelled in this region. This can be readily rationalised by considering that the terminating hydrogen atoms of the cluster model, which are not present within the periodic zeolite, will be surrounded by an electrostatic potential which has no periodic counterpart. Further consideration to a screening procedure designed to remove this problem will subsequently be given.

The disposition of the grid and the set of sampling points within it is, however entirely arbitrary. It would be possible, for example to include a relatively large number of points in the region in which a substrate molecule was likely to dock, with fewer sampling grid points more distant from the cluster. In the first instance though, simple 3D meshes of equally spaced sampling grid points are used.

3.2.6 - Difference potential evaluation

Provided the electrostatic potential has been evaluated on the same grids in both the periodic and molecular cases, we can easily generate the difference potential, $\left(P_{crystal} - P_{cluster}\right)$. A problem that can arise at this stage is that molecular SCF codes may re-orientate the molecular cluster to make maximum use of any molecular symmetry present. Such a problem was encountered in our use of the GAMESS-UK code, but may be circumvented by the use of the 'nosym' directive or explicit use of the appropriate transformation matrix.

The point charge representation has a possible detrimental effect because the fitting procedure can be biased unduly, as sampling points in close proximity to fitting grid sites penetrate substantially the charge density of the periodic system, and become unsuitable for representation by an atom-centred point charge model. This undesirable effect can be lessened by removing points from the sampling grid which lie in close proximity to fitting grid sites. In this way, there is an increase in the number of sampling grid points in the region of interest, at the expense of sampling grid points in regions where such an accurate potential is not required. More detailed consideration of this screening procedure and the effect it has on calculated chemical properties will be given subsequently.

3.2.7 - Fitting grid selection

As the point charges within the model we are developing are merely a convenient way of representing the potential of the infinite system, the sites at which they are located are also not physically constrained. It is therefore possible to generate fitting grids which do not necessarily reflect the geometry of the zeolite they represent. We are, however attempting to reproduce the electrostatic potential from a crystal in which, to a first approximation, the electrostatics can be represented by a set of atom-centred charges. For this reason, it was decided to use a set of fitting grid points comprised of atomic sites within the crystal structure. In this work the fitting grid was defined as the set of crystal sites lying within a spherical boundary, typically centred on the central T site of the chosen cluster.

To reduce the problem of point charges polarising the electronic structure of the cluster, an additional screening procedure was incorporated, whereby any fitting grid sites which lie close enough to the cluster to cause undue polarisation are excluded from the charge fitting procedure. In this thesis, fitting grid sites in the first shell of atoms outside the terminating hydrogens were removed.

3.2.8 - Point charge evaluation

The point charges which best generate the correcting potential are derived by a least-squares method. This has the advantage of being easily implemented, as well as fast compared to the timescale of the subsequent Hartree-Fock embedded cluster studies.

The criteria used for the quality of the fitting procedure is the minimisation of the standard deviation, σ, between, the ideal correcting potential and that from the set of calculated charges.

$$\sigma = \sqrt{\frac{\sum_{n} \left(P_n^{charges} - P_n^{calculated} \right)^2}{n}} \qquad (3.3)$$

where n is the number of sampling grid points, $P_n^{charges}$ is the exact correcting potential defined in equation 3.2 at sampling point n and $P_n^{calculated}$ is the classical electrostatic potential at the same point due to the calculated set of charges, given simply as

$$P_n^{calculated} = \sum_{m} \frac{Z_m}{r_{nm}} \qquad (3.4)$$

where Z_m is the value of the charge at fitting grid point m and r_{nm} is the separation of sampling grid site n and fitting grid point m. A standard matrix diagonalisation scheme is used in the least-squares solution of the resulting set of equations.

It is also possible at this stage to determine the value of the shift parameter, discussed in chapter 2, which arises as a result of the possibility of different zero values of the electrostatic potential for the cluster and periodic systems. More specifically, the value obtained for a periodic potential depends on the method used in the summation technique adopted in it's evaluation. The zero value of electrostatic potential, an unambiguous quantity within molecular calculations, is undefined in a periodic solid as an infinite displacement still lies formally within the crystal. This shift parameter is determined simply as an additional variable in the least-squares fitting procedure. In the same manner, it is possible to incorporate extra constraints into the fitting procedure. For instance, it may be desirable to generate a field of charges in which the net charge or

dipole is zero, or where the magnitude of the charges is restricted to a user-defined tolerance.

3.2.9 - Model construction and nomenclature

After the PDC field within which the cluster is to be embedded has been generated, there are a number of points which should be borne in mind when constructing the model prior to use within calculations.

If geometry optimisations are to be performed, it should be remembered that the correction provided by the PDC field will only be valid if the relative orientation of the cluster and charges are maintained. In effect, this means that the cluster must have some form of spatial constraint. If no such constraint is placed on the position of the cluster, there is a tendency for it to drift into the PDC field. Within both GAMESS-UK and Gaussian 92, a carefully constructed z-matrix can be used to maintain the orientation of the cluster with respect to the charge field, whilst allowing portions of the model to relax. As the terminating hydrogen atoms are not a part of the real zeolite which is being modelled, they can be used to generate a fixed 'net' of atoms from which the sections of the system which are to be relaxed can be defined.

When describing the calculations carried out within the embedded cluster formalism, the following system of nomenclature, based on that of Pople[12], is adopted. Periodic calculations are described as normal (e.g. Periodic/STO-3G). The cluster calculations are denoted by the termination method employed followed by the basis set used in the calculation and that used in the determination of the PDC field (where

appropriate). Thus, Si-OH/STO-3G/STO-3G denotes a calculation on an Si-OH terminated cluster using the STO-3G basis set, embedded in a field of PDC determined at the STO-3G basis set.

3.3 - Model validation

3.3.1 - Selecting a system for validation

The embedded cluster model described in general terms in the previous section can now be validated using the results of periodic Hartree-Fock calculations or values predicted by previous calculations as a benchmark.

Although we are interested in high-silica zeolites, and particularly those of industrial interest (e.g. zeolite Y and H-ZSM-5), such systems often have large primitive cells making them difficult to study at a periodic *ab initio* level. Silicalite, the purely siliceous analogue of the zeolite H-ZSM-5, for example, is particularly difficult to study at a periodic Hartree-Fock level because of the very large unit cell (288 atoms), as well as the relatively low symmetry P_{nma} space group. Although a periodic Hartree-Fock calculation has been carried out on this zeolite at the minimal basis set level[3], to allow for the use of the larger basis sets needed for quantitative studies, a medium-pore zeolite with a substantially smaller unit cell, cancrinite[13], was chosen. Cancrinite has pores with free channel diameters of 5.9 Å, compared with the 5.2 x 5.7 Å and 5.3 x 5.6 Å channels of ZSM-5. The crystal structure used is of the space group $P6_3$ and for the purposes of the periodic Hartree-Fock calculation, all aluminium sites were replaced with silicon, allowing the sodium counterions to be neglected. The CRYSTAL input deck used for the

calculation of the PHF wavefunction, with a representation of the primitive cell of the resultant system, are included as appendix A(1) and A(2) respectively.

A number of properties can be used to determine the relative performance of the bare and embedded cluster models, falling into two primary areas:

(a) Cluster properties

(b) Cluster-substrate interactions

The cluster properties which can be compared are electrostatic potentials, geometries and the vibrational properties of the Brønsted hydroxyl group in aluminium substituted clusters. It should be noted that the choice of cancrinite as a model system for which to prototype the embedded cluster model means there is no experimental IR data which can be used to assess the relative performance of the embedded and bare cluster models. The calculated harmonic vibrational frequencies for the Brønsted sites of aluminated forms of the clusters are included as they help to show the effect of the embedding procedure on the properties of the clusters.

Two types of substrate interactions are considered in this chapter. In the first series of calculations, detailed in section 3.3.5, binding energy evaluations were performed within a periodic supercell formalism, using credible though non-optimal geometries with which cluster results, both bare and embedded could be compared. Such calculations allow for the direct comparison of bare and embedded cluster models relative to periodic interaction energies, an important test if future studies of zeolite catalysis are to be made.

The second series of substrate interactions, described in section 3.4.4, involve the geometry optimisation of a substrate, water in this case as it provides a good probe of

the acidity of the cluster, and are included primarily as a test to ensure that no unforeseen problems or unphysical effects preclude the use of the embedded cluster model in the representation of zeolite-substrate interactions. It should again be noted that since cancrinite is not a genuine high-silica zeolite, we can only really consider the crystal structure used here as a model. For this reason, there is no experimental data which can be used to determine the relative performance of the embedded and bare cluster models, in terms of binding energies. Also, since the computational demands which would have arisen as a result of the use of split valence basis sets, such calculations were not performed at a periodic Hartree-Fock level, and no comparisons could therefore be made. The binding motifs determined, both in the presence and absence of the PDC field are included because of the substantial differences they exhibit compared to the results of previous calculations.

3.3.2 - Computational details of model generation

Calculations considering the electrostatic potential and interaction energies were carried out at the minimal (STO-3G)[14] basis set level, whilst investigations of optimised cluster geometries and O-H vibrational frequencies were carried out at the 3-21G basis set level, also investigating the effect of addition of polarisation functions[15,16,17,18]. The periodic Hartree-Fock calculations at both the STO-3G and 3-21G basis set levels used ITOL 1-5 values, as described in chapter 2, of 5, 5, 5, 6, and 12 with the reciprocal space RTOL1 parameter set at 4. Level shifting of 10^{-3} Hartree was used to accelerate wavefunction convergence[19].

T3 clusters were used as they provide a cluster sufficiently large to allow for the possibility of studying zeolite-substrate interactions, as well as having been used in large numbers of previous studies. The effect of termination using both the Si-H and Si-OH methods, as well as the incorporation of point charge fields was investigated.

The Si-H terminated cluster (shown as figure 3.2(a)), of stoichiometry $Si_3O_4H_8$, had the Si-H terminators set at a distance of 2.80 bohr along the direction of the terminated Si-O bond vector. The Si-OH terminated cluster, shown in figure 3.2(b), of stoichiometry $Si_3O_{10}H_8$, had the terminating hydrogens set along the O-Si bond vectors to give OH bond lengths of 1.90 bohr. These values were arbitrarily chosen as 'sensible' lengths in the context of previous studies. The co-ordinates of both clusters used for the study, are included as appendix A(3) (Si-H termination) and A(4) (Si-OH termination).

The electrostatic potential was determined from the converged wavefunction by generating a cubic grid large enough to encompass the clusters, of side length 20 bohr, with 18 points along each side. The co-ordinates of the corners of the sampling grid used are included as appendix A(5). For these calculations to investigate the plausibility of the embedded cluster model, the fitting procedure was carried out with a set of parameters which, although essentially arbitrary, provided intuitively reasonable values which could be optimised through later work. The sampling grid used, as described above, initially contained 5832 points. A cut-off scheme was used where any fitting grid points lying within a sphere of radius 3.5 bohr of the cluster sites, including the hydrogen terminators, were excluded from the fitting procedure. This value was sufficient to remove the first co-ordination sphere of atoms close to the terminating hydrogens. A second cut-off scheme, used to remove any sampling grid points lying close to fitting grid sites was also

employed, whereby any sampling grid points lying within a sphere of 2.5 bohr of any remaining fitting grid point or terminating hydrogen were deleted.

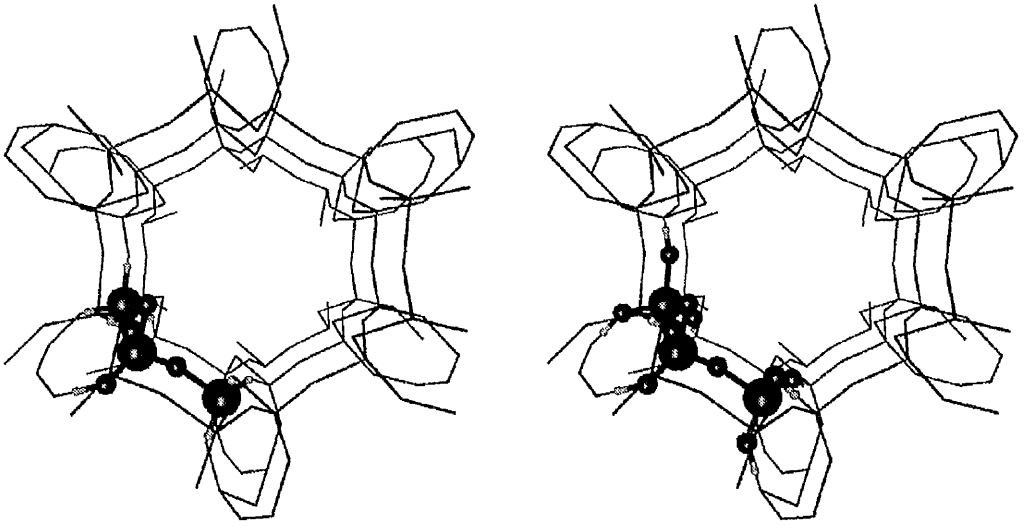

(a) Si-H termination. *(b) Si-OH termination.*

figure 3.2 - T3 molecular clusters in relation to the cancrinite channel system.

The fitting grid was based on a sphere of crystal sites lying within a 19 bohr sphere, centred on the middle T site of the T3 cluster. After the sampling and fitting grids were screened, the Si-H model contained 4562 sampling grid points and 197 points in the fitting grid, whilst the Si-OH terminated model contained 4644 points in the sampling grid and 189 fitting grid sites. In both cases, the fitting of the potential derived charges on the fitting grid sites was carried out including the calculation of the shift parameter discussed in chapter 2, with no constraints imposed on either the total charge or the total dipole of the system. The sampling grid volume and the set of fitting grid points are shown in relation to the cancrinite channel system as figure 3.3(a) and (b), respectively.

The cubic volume encompassing the cluster shows the spatial extent of the sampling grid, with the fitting grid sites represented by spheres.

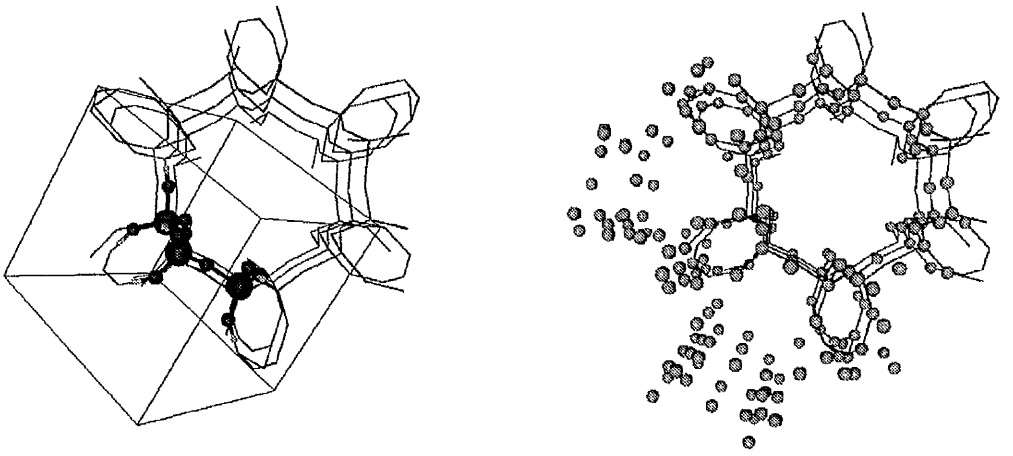

(a) Sampling grid volume. *(b) Fitting grid sites.*

figure 3.3 - Sampling and fitting grids in relation to the cancrinite channel system.

3.3.3 - Electrostatic potentials

The model is designed to correctly reproduce the electrostatic environment in the region of the cluster and cancrinite pore system. The degree to which the modification of the cluster potential by the point charge field has been successful in reproducing the periodic potential is the first and most important test of the efficacy of the model. For the determination of the potential, the following five systems were considered.

(a) Periodic/STO-3G

(b) Si-H/STO-3G/NONE

(c) Si-H/STO-3G/STO-3G

(d) Si-OH/STO-3G/NONE

(e) Si-OH/STO-3G/STO-3G

Figure 3.4 shows the STO-3G electrostatic potential for the five systems, (a)-(e) described above, in the plane of an Si-O-Si group. This particular plane was chosen as this site was preferred, for reasons of accessibility to substrates within the pores, as the site at which protonation would occur to form a Brønsted site in subsequent aluminated cluster studies. The plane was chosen so that it lay entirely within the sampling grid volume, with the potential evaluated at 4000 points on a 20 x 20 grid. All cluster potentials have been adjusted by the appropriate shift parameter to the same zero point. A noteworthy feature within the periodic potential, (a), is a well of negative potential in the region of the bridging oxygen of depth ~95 kcal mol^{-1}, a feature which has been noted in previous bare cluster calculations[20]. The gradient of the electrostatic potential towards the centre of the zeolite channel (the upper-right of the plot) is a particularly important property when the energetics and geometry of docked substrates is to be considered. The bare cluster models, (b) and (d), give a particularly poor representation of the gradient of the potential across the zeolite channel, which is substantially improved in the embedded cluster models (c) and (e). Visual inspection suggests the quality of models is in the order (e) > (c) > (d) > (b).

A quantitative measure of the similarity of the electrostatic potentials can be evaluated by considering the value of the standard deviation of the cluster potential compared to the periodic potential, in a given volume of the sampling space. The standard deviation over the entire sampling space is not a meaningful measure of the quality of the model as regions are deliberately omitted during the fitting procedure. This is reflected in the standard deviations of the electrostatic potentials over the entire fitting volume which were 60.5, 21.8, 56.8 and 21.4 kcal mol^{-1} for (b) to (e), respectively. A more meaningful measure is the standard deviation in the region of the active site. Standard deviations were evaluated for the Si-OH terminated models (d) and (e), which provided the most convincing representation of the electrostatics of the infinite system, within an approximately cubic region of side ~1Å containing 8000 points on a grid of 20 x 20 x 20 points. In this more important region of the sampling volume, the standard deviation of model (e) is reduced to 1.6 kcal mol-1, compared to 7.7 kcal mol-1 for model (d), after an optimised shift potential for the smaller volume has been incorporated.

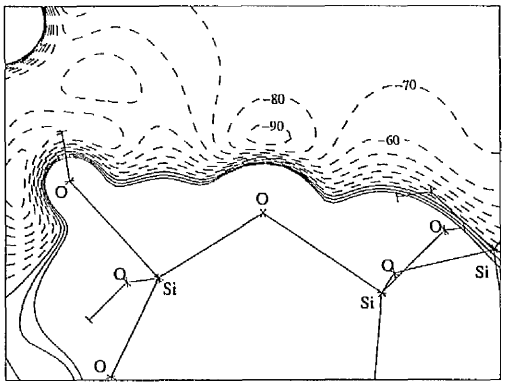

(a) Crystal potential.

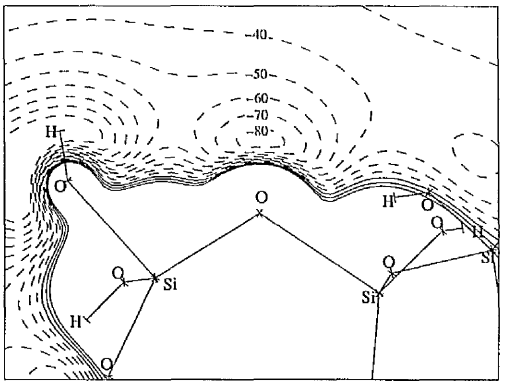

(d) Si-OH/STO-3G/None potential.

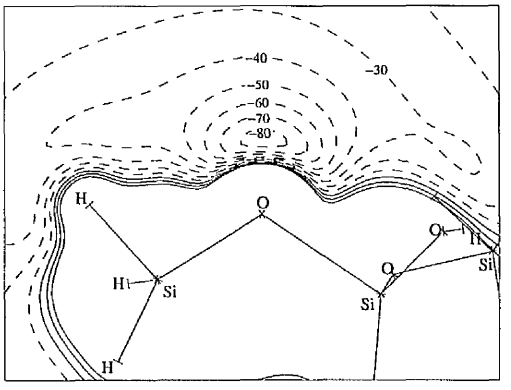

(b) Si-H/STO-3G/None potential.

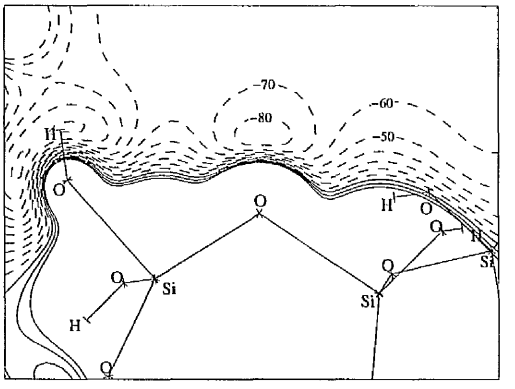

(e) Si-OH/STO-3G/STO-3G potential.

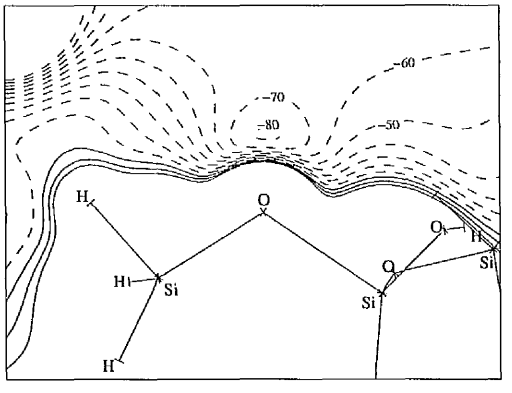

(c) Si-H/STO-3G/STO-3G potential.

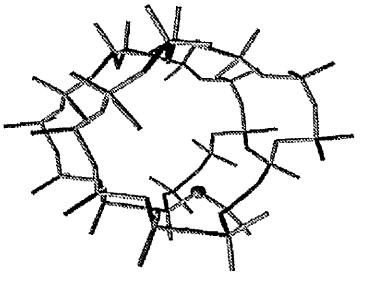

(f) Bridging oxygen site and Si-O-Si plane.

figure 3.4 - 2D slices through the STO-3G electrostatic potential in the plane of the channel-directed bridging Si-O-Si group. Contours shown are from -100 to +20 kcal mol^{-1} at 10 kcal mol^{-1} intervals. Dotted lines indicate regions of negative electrostatic potential. In each case, a wireframe projection of the relevant cluster is shown, except for the periodic system where, for reasons of clarity, the Si-OH terminated cluster is included. (f) Shows a section of the cancrinite channel with the bridging oxygen, denoted by a sphere, through which the Si-O-Si plane passes.

3.3.4 - Cluster geometries

3.3.4.1 - Computational details

A Brønsted acidic site, the geometry of which could be used to judge the performance of the embedded cluster model, was generated by substituting the silicon at the central T site for aluminium, and adding a hydrogen atom to the bridging oxygen directed into the zeolite pore. As noted previously, it is necessary to spatially constrain the positions of the terminating hydrogens and the terminal regions of the cluster. Inside the constrained periphery of the cluster, the positions of the aluminium defect, all four attached oxygens and the acidic hydrogen were allowed to optimise. Whilst the ability of zeolites to structurally relax is undoubtedly an important facet of their catalytic activity, the constrained optimisation scheme adopted appears to provide a reasonable approximation, allowing the model to include the salient features of the zeolite acidic site. It should be noted at this point that this is an area of the model in which substantial improvements could be envisaged, but are beyond the scope of this thesis. A more complete model would address the problems of framework relaxation in conjunction with an improved representation of the electrostatic potential. The use of such a constrained optimisation scheme, however prevents the characterisation of the stationary points. Thus, all stationary points reported subsequently in this thesis are assumed to be minima.

The point charges were fitted to a difference potential evaluated at the 3-21G basis set, but a series of geometry optimisations were carried out using the 3-21G basis set, then a 3-21G basis set augmented by d functions on Si and Al (3-21G(*)) with exponents 0.45. and 0.325 respectively, and the latter augmented by p functions with

exponent 1.1 on the acidic hydrogen (3-21G(*)*). At each of these three basis sets, a constrained geometry optimisation was carried out, both with and without the point charges, for both the acidic and anionic forms of the zeolite. Additionally, harmonic vibrational frequencies were determined for the acidic zeolites by a 3 point finite-differences approach in which the Brønsted hydrogen was displaced ±0.002 bohr. Unless otherwise noted, all lengths and angles in subsequent tables are given in angstroms and degrees, respectively.

3.3.4.2 - Computational results

Optimised geometries for the acidic and anionic forms of the clusters, subject to the constraints described previously, are reported in tables 3.1 and 3.2, respectively. The effect of the PDC field is to increase the harmonic frequency, at each of the three basis sets considered, an effect due to the substantial weakening of the Al_2-O_5 bond and the simultaneous strengthening of the O_5-H_6 bond. The inclusion of polarisation functions on the hydrogen significantly shortens the O_5-H_6 bond, to a greater degree than the inclusion of the PDC field. We observe the same trends in structural parameters with changing basis sets as those found by Ugliengo, Saunders and Garrone[21] in a study of $SiH_3(OH)$, where the inclusion of p functions on the acidic hydrogen is dominant in the shortening of the O-H length, whilst the addition of d functions to silicon results in contraction of the Si-O bond. The PDC field has opposite effect in the acidic and anionic clusters, causing a marked increase in the Si-O length for the acidic cluster and a slight decrease for the deprotonated system.

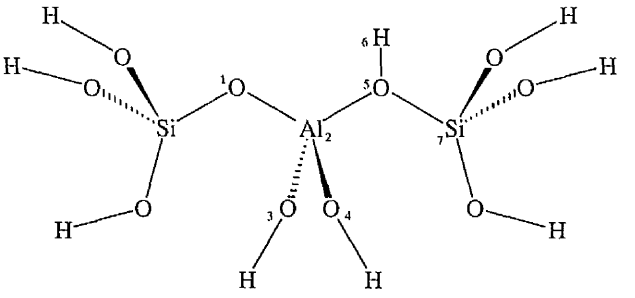

figure 3.5 - Atom numbering for structures used in cluster geometry optimisations.

	O_5-H_6	Al_2-O_1	Al_2-O_5	Si_7-O_5	Si_7-O_5-H_6	Si_7-O_5-Al_2	ν_{OH}
3-21G/NONE	0.985	1.664	1.849	1.642	128.9	129.1	3542
3-21G/3-21G	0.979	1.701	1.945	1.684	117.1	127.3	3671
3-21G(*)/NONE	0.983	1.678	1.880	1.629	127.0	128.6	3570
3-21G(*)/3-21G	0.981	1.714	1.985	1.660	116.4	127.4	3634
3-21G(*)*/NONE	0.956	1.678	1.888	1.631	125.5	128.5	3855
3-21G(*)*/3-21G	0.955	1.712	1.996	1.661	115.7	127.3	3881

table 3.1 - Optimised acidic cluster geometries - numbering corresponds to figure 3.5 - harmonic frequencies (cm^{-1}) are unscaled.

	Al_2-O_1	Al_2-O_5	Si_7-O_5	Si_7-O_5-Al_2
3-21G/NONE	1.721	1.762	1.595	134.7
3-21G/3-21G	1.754	1.779	1.591	134.8
3-21G(*)/NONE	1.742	1.781	1.569	134.9
3-21G(*)/3-21G	1.777	1.796	1.564	134.2

table 3.2 - Optimised anionic cluster geometries - numbering corresponds to figure 3.5.

The bond lengths of the acidic cluster at the 3-21G(*)* basis set (O-H, 0.955 Å; Si-O, 1.661 Å; Al-O, 1.996 Å) are in close agreement with predictions made by Sauer[22], who suggested bond lengths of O-H, 0.965 ± 0.01 Å; Si-O, 1.685 ± 0.05 Å; Al-O, 1.94 ± 0.05 Å for a zeolite Brønsted site.

3.3.5 - Interaction energies

3.3.5.1 - Computational details

An additional test of the quality of the four models, (b)-(e), considered in the previous section is the representation of interaction energies of substrates within the channel. Accurate representation of the energetics of molecules sorbed near Brønsted sites is a vital pre-requisite in the quantitative modelling of reactivity. For this reason, a single Brønsted site was incorporated into the periodic cancrinite system, against which substrate molecules, in this case water and the hydroxonium ion, could be docked. Due to the present lack of geometry optimisation facilities within CRYSTAL, it was not possible to produce optimal periodic zeolite-substrate geometries. We are, however only interested in how well the periodic interaction energy is reproduced, so the use of credible geometries for the zeolite-substrate interaction provides useful information on the relative performance of embedded and bare cluster models.

Due to the small primitive cell size of cancrinite, the possibility exists that substrate molecules may lie close to each other in the periodic system giving rise to substantial substrate-substrate interactions which are not present in the cluster models. To reduce this effect, a periodic supercell approach was applied in which the cancrinite

primitive cell size was doubled along the c axis, along which the distance between water molecules in neighbouring cells was smallest. This increase in the size of the primitive cell, as well as the drop in symmetry associated with the incorporation of the substrate, precluded the calculation being performed at anything other than the minimal (STO-3G) level. The interaction energy was obtained as

$$E_{interaction} = E_{periodic+substrate} - \left(E_{periodic} + E_{substrate}\right) \qquad (3.5)$$

Where $E_{substrate}$ corresponds to the energy of a periodic array of substrate molecules for the periodic system, or the energy of an isolated substrate molecule for the cluster models. For the case of the hydroxonium ion, the interaction energies are reported relative to periodic water and the neutral zeolite as CRYSTAL is unable to perform calculations on ionic systems. As an aside, a possible method of circumventing this difficulty could be to apply a similar strategy to that used in a recent Car-Parinello study of zeolite structure[23], where charge neutrality for the anionic zeolite was maintained by delocalising a positive charge throughout the unit cell.

3.3.5.2 - Computational results

The geometry for the systems used was obtained by incorporating the optimised framework geometry from an Si-OH terminated, T3 STO-3G cluster optimisation, for both the neutral and anionic zeolite, into the periodic system and cluster models. The substrates were docked visually to give reasonable interaction motifs, based on previous work[24]. In this way, credible structures were generated. However, it should be noted that the Al_3-O_4 distance of 1.493 Å is very short, a result of allowing the positions of atoms

O_4 and O_5 to optimise in the cluster calculation, highlighting the difficulty involved in incorporating optimised cluster geometries into periodic systems. Whilst this may affect the absolute energies of the interactions, the short bond length is replicated in all systems, so the resulting interaction energies are still comparable.

A fuller description of the details of the construction of the periodic cluster, water and hydroxonium models, including co-ordinates, is included as appendix A(6). Stereoviews showing the disposition of the acidic cluster, water and hydroxonium ion within the periodic supercell are shown as figure 3.7, 3.8 and 3.9, respectively.

	neutral cluster	**neutral cluster + H_2O**	**anionic cluster + H_3O^+**
Si_1-O_2	1.648	1.640	1.636
O_2-Al_3	1.712	1.738	1.775
Al_3-O_4	1.493	1.511	1.534
Al_3-O_5	1.642	1.653	1.674
Al_3-O_6	1.996	1.921	1.849
O_6-Si_7	1.661	1.637	1.605
O_6-H_8	0.955	1.047	1.434
H_8-O_9	-	1.644	1.029
O_9-H_{10}	-	0.946	0.948
O_9-H_{11}	-	0.943	0.960
H_{11}-O_2	-	2.336	1.629

table 3.3 - Bond lengths of systems used in determining interaction energies of H_2O.....H and H_3O^+ systems. Atom numbering corresponds to figure 3.6.

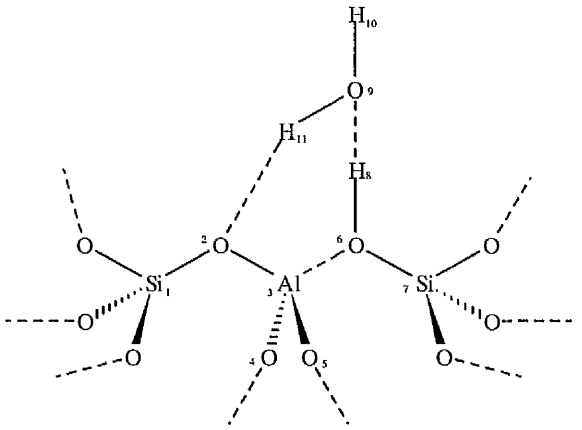

figure 3.6 - Atom numbering for structures used for interaction energy calculations.

model	H_2O.....H	H_3O^+
Periodic/STO-3G	-18.3	-21.9
Si-H/STO-3G/NONE	-6.1	11.9
Si-H/STO-3G/STO-3G	-11.0	-8.6
Si-OH/STO-3G/NONE	-9.5	1.2
Si-OH/STO-3G/STO-3G	-13.8	-15.4
Si-OH/STO-3G/3-21G	-16.0	-21.6

table 3.4 - Energies, in kcal mol^{-1}, of structures with H_2O and H_3O^+ interacting with zeolite, relative to H_2O and protonated zeolite.

The possibility of incorporating point charge fields fitted to a difference potential evaluated at another basis set is explored by using a STO-3G basis set for the cluster within a PDC field fitted to a 3-21G difference potential. The excellent agreement with the STO-3G periodic interaction energies suggests this approach to be useful.

The presence of an accurate representation of the potential is shown to be most crucial for modelling the interaction of protonated species. This is not surprising as the mode of zeolite catalysis is thought, in many cases, to rely on the selective stabilisation of

protonated species, transition states and intermediates by the electrostatic potential within the zeolite channel.

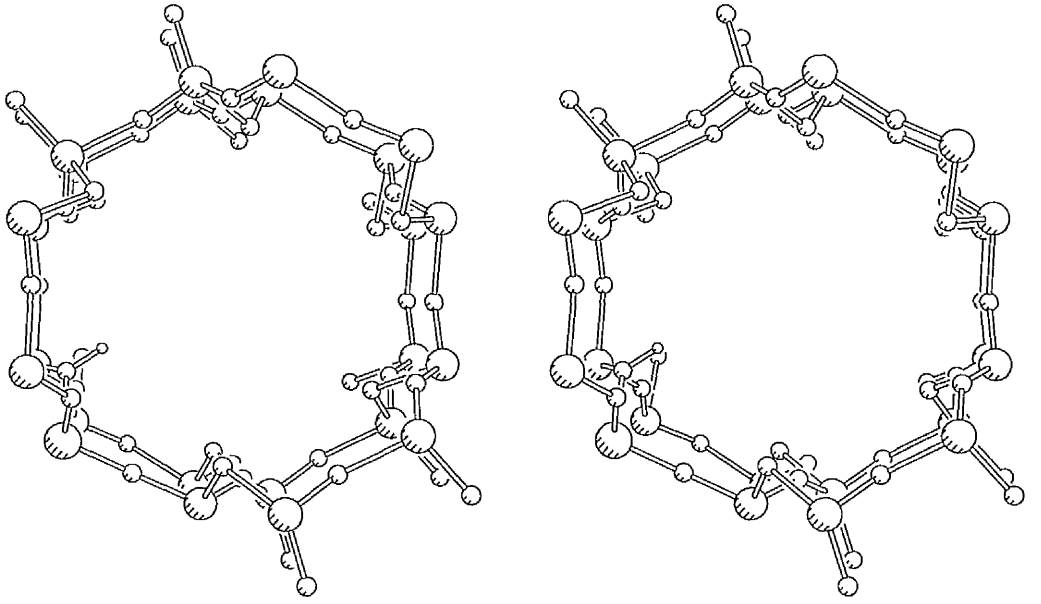

figure 3.7 - Stereoview showing periodic supercell containing Brønsted acidic site.

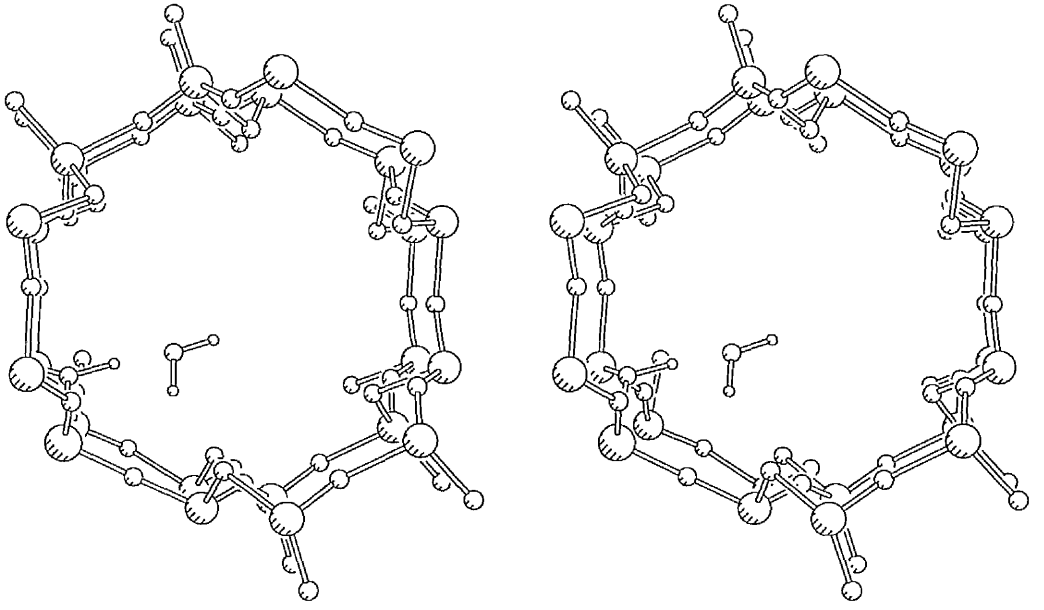

figure 3.8 - Stereoview showing periodic supercell with H_2O.....H system.

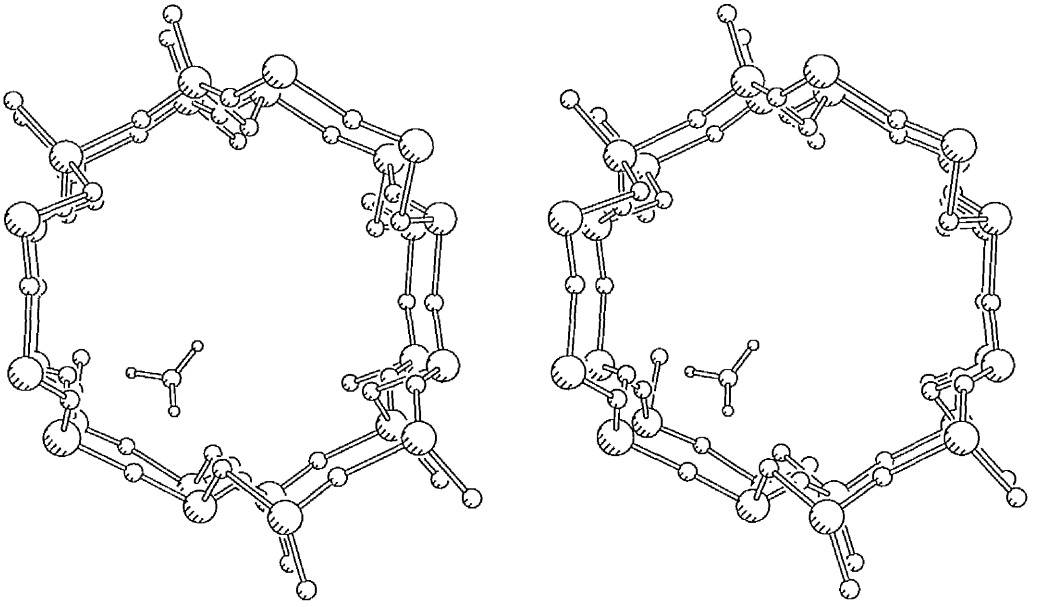

figure 3.9 - Stereoview showing periodic supercell with H_3O^+ species.

3.4- Refinement of the fitting procedure

3.4.1 - Determining the optimum charge field

One of the most important variables in the embedded cluster model is the radius of the sphere used in the generation of the sampling grid. In an attempt to determine the optimum sphere size, a study of the interaction energy for the Si-OH terminated cluster, previously found to give the best interaction energies and potential representation, is considered. The sphere of charges used is centred on the middle T site of the cluster. The optimisation of the point charge field can be considered in tandem with the selection of the optimum difference potential from which it is derived, described in the following section.

3.4.2 - Determining the optimum difference potential

It is possible to determine a set of charges which are fitted to an 'acidic' difference potential, in which the periodic calculation is performed on a zeolite containing the Brønsted site geometry. A comparison of the interaction energies obtained using charges fitted to the acidic and siliceous difference potentials can be used to investigate the approximation of incorporating aluminium into a cluster within a charge field corresponding to a siliceous zeolite.

Clearly the interaction energies, reported in tables 3.5 and 3.6, which result from the bare cluster models, regardless of the cluster termination method employed, are substantially in error when compared to the periodic values. For the H_2O...H systems, the energy difference between the system within the 19 bohr sphere of charges and the periodic value is around 1 kcal mol^{-1} for the embedded Si-H and Si-OH terminated clusters, in contrast with the bare clusters in which the difference is around 5 kcal mol^{-1}. In the case of the H_3O^+ ion systems, the error is especially evident with the bare cluster models, which give interaction energies differing from the periodic value by 48 to 68 kcal mol^{-1}, dependent on the cluster used.

A substantial improvement in these energies can be obtained, even with moderately small charge fields, with the 19 bohr sphere of charges giving interaction energies for the Si-OH cluster which are within 4 kcal mol^{-1} of the periodic value. For the Si-H terminated cluster, larger errors are obtained, with the interaction energies differing from the periodic values by some 10 kcal mol^{-1}.

	$H_2O...H$ (Si)	$H_2O...H$ (Al)	H_3O^+ (Si)	H_3O^+ (Al)
Periodic/STO-3G	-10.1	-10.1	41.2	41.2
Si-OH/STO-3G/NONE	-6.4	-6.4	89.5	89.5
Si-OH/STO-3G/STO-3G 11au	-7.7	-7.7	68.1	68.6
Si-OH/STO-3G/STO-3G 12au	-7.7	-7.7	67.7	68.0
Si-OH/STO-3G/STO-3G 13au	-8.1	-8.3	63.9	64.0
Si-OH/STO-3G/STO-3G 14au	-8.5	-8.7	55.4	55.4
Si-OH/STO-3G/STO-3G 15au	-9.4	-9.7	49.4	49.2
Si-OH/STO-3G/STO-3G 16au	-10.8	-11.1	46.9	46.3
Si-OH/STO-3G/STO-3G 17au	-10.8	-11.1	47.0	46.4
Si-OH/STO-3G/STO-3G 18au	-10.8	-11.2	46.4	45.8
Si-OH/STO-3G/STO-3G 19au	-11.0	-11.3	45.3	44.7

table 3.5 - Interaction energies, in kcal mol^{-1} for Si-OH terminated clusters + water and hydroxonium ion. Si or Al denotes the difference potential to which the charges (if any) were fitted.

	$H_2O...H$ (Si)	$H_2O...H$ (Al)	H_3O^+ (Si)	H_3O^+ (Al)
Periodic/STO-3G	-10.1	-10.1	41.2	41.2
Si-H/STO-3G/NONE	-5.2	-5.2	109.7	109.7
Si-H/STO-3G/STO-3G 11au	-7.5	-7.6	76.0	76.9
Si-H/STO-3G/STO-3G 12au	-6.5	-6.7	70.8	71.6
Si-H/STO-3G/STO-3G 13au	-7.9	-8.1	62.8	63.3
Si-H/STO-3G/STO-3G 14au	-8.0	-8.3	60.8	61.0
Si-H/STO-3G/STO-3G 15au	-9.1	-9.4	55.2	55.4
Si-H/STO-3G/STO-3G 16au	-10.8	-11.1	51.2	51.0
Si-H/STO-3G/STO-3G 17au	-10.8	-11.2	51.5	51.1
Si-H/STO-3G/STO-3G 18au	-10.9	-11.2	51.2	50.8
Si-H/STO-3G/STO-3G 19au	-10.8	-11.2	51.3	50.9

table 3.6 - Interaction energies, in kcal mol^{-1}, for Si-H terminated clusters + water and hydroxonium ion. Si or Al denotes the difference potential to which the charges (if any) were fitted.

In all cases, the interaction energy is seen to converge rapidly, with the larger spheres of charges giving interaction energies closest to those of the periodic system. Also, the larger Si-OH cluster is found to give interaction energies which are significantly better than those from the Si-H system. This seems reasonable in view of the increased distance from the substrate to the terminal regions of the cluster and the field of point charges.

The very small differences in the interaction energies obtained for the same cluster and substrate using charges fitted to siliceous and acidic difference potentials,

which differ by only around 1 kcal mol^{-1}, shows the calculation of charges for a fully siliceous zeolite with the incorporation of aluminium occurring at the embedding stage to be an excellent approximation. This result is particularly useful as it shows the cheaper siliceous calculation provides results comparable to those from the substantially more expensive periodic calculation containing an acidic site.

3.4.3 - Optimising the screening procedures

The use of a screening procedure to prevent polarisation of the cluster has obvious merit. To determine a radius which can be generally applicable for a range of zeolites is, however somewhat difficult as the number of atoms which are deleted within a given cut-off radius does not increase smoothly with distance. For this reason, the cut-off scheme to remove fitting grid sites remains at 3.5 bohr, sufficient to remove the first co-ordination sphere outside of the terminating atoms. The screening procedure designed to remove sampling grid points which lie close to fitting grid sites has, however been optimised using the interaction of water with cancrinite as a benchmark. Within this model, for which the interaction energy within the periodic zeolite is known, the interaction energy within the embedded cluster model, using the Si-OH terminated T3 cluster embedded within a 19 bohr sphere of point charges, was evaluated as a function of the screening distance.

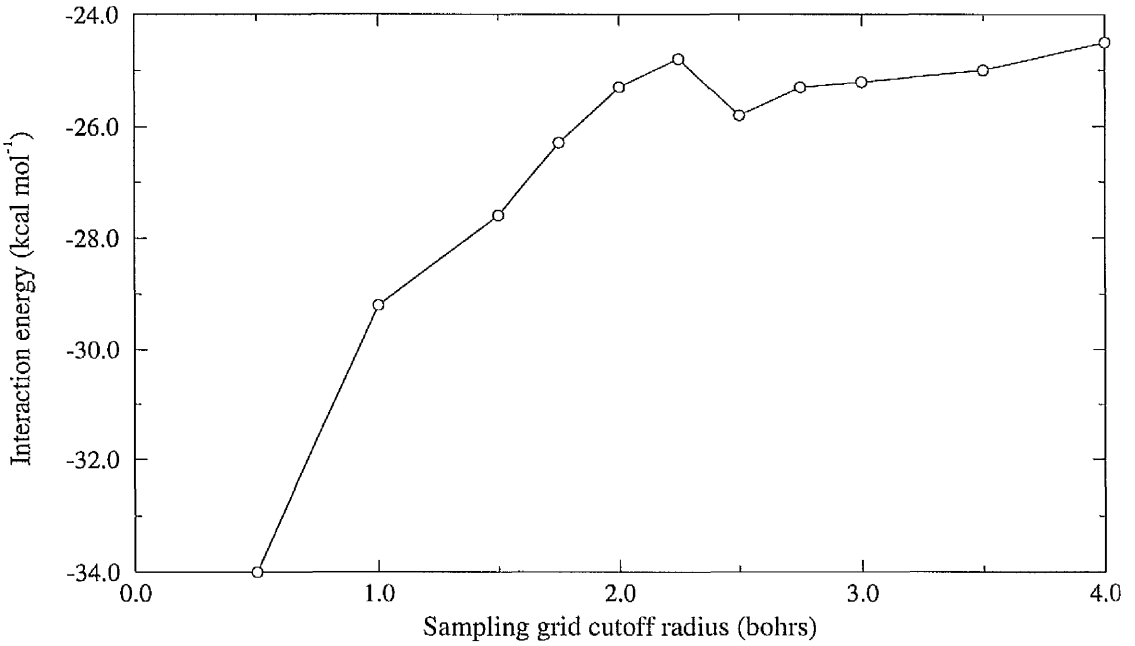

figure 3.10 - Graph of interaction energy, in kcal mol^{-1}, against sampling grid radius, in bohr, for Si-OH terminated T3 cluster + H_2O.

The sharp decrease in the calculated interaction energy shown in figure 3.10 until a cut-off radius of around 2.0 bohr and the subsequent stability up to cut-off parameters of 4.0 bohr, suggests that a radius of 2.0-3.5 bohr will perform well in preventing the fit from becoming excessively biased in the regions of the fitting grid sites. Caution must, however be applied in that setting the cut-off parameter to large values ($\geq$ 3.5 bohr), will introduce an additional problem in that the relative number of points in the sampling and fitting grids can cause severe errors in the least-squares fitting procedure. For this reason, all future fittings of PDC presented in this thesis will use a sampling grid cut-off of 2.0 bohr.

3.4.4 - Cluster-substrate optimisations

To investigate the plausibility of using the embedded cluster model in the study of zeolite-substrate interactions, the interaction of water with cancrinite was used as a model system to determine likely difficulties

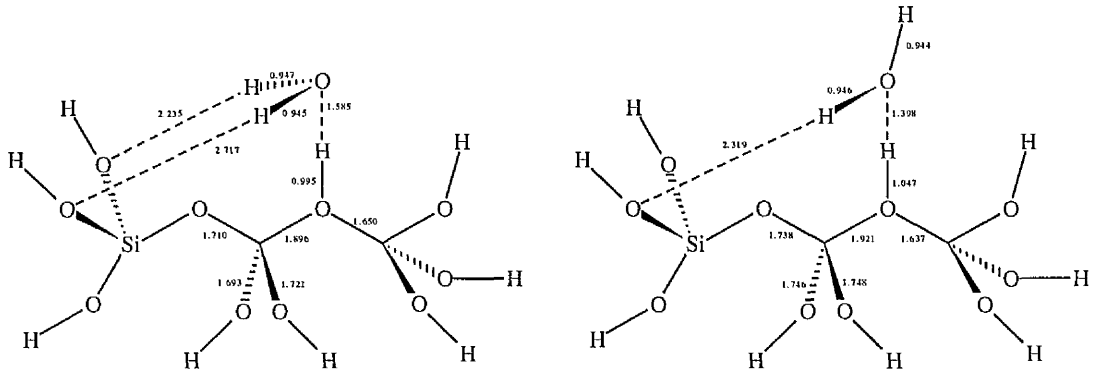

(a) No PDC field *(b) 3-21G PDC field*

figure 3.11 - Stationary points determined at the 3-21G(*) basis set, starting from water and T3 Si-OH terminated acidic zeolite.*

The binding motifs determined, whether or not the PDC were present, were surprising, as the hydrogen bonding occurred to oxygens in the terminal regions of the cluster. The geometries adopted were particularly unexpected in view of the bifurcated geometries obtained in previous studies[24], especially as the geometry optimisations were started with the water substrate adopting a bifurcated hydrogen bonding motif. It should, perhaps be borne in mind that previous studies of water interaction with bare cluster models of zeolites have used clusters in which the termination is *via* Si-H bonds, and the terminal O-H groups involved in the hydrogen-bonding interaction are simply not

present. Implicit in this statement is the possibility that the hydrogen bonding is occurring to an oxygen which is not necessarily realistically represented. The degree to which the oxygens attached directly to the terminal hydrogens are realistic, especially within the constrained optimisation scheme employed, is open to question. The geometry adopted by the water is certainly interesting enough, however that additional work, beyond the scope of this thesis, be carried out. The use of unconstrained Si-OH terminated bare clusters in such a study would be a useful first step determining whether the failure to detect a stationary point for the bifurcated bound water was a result of a compromise of the inherent flexibility of the zeolite or a real effect. Ideally, single-point energy determinations using a periodic Hartree-Fock approach could be used to determine whether hydrogen-bonding motifs of the type obtained within the constrained cluster optimisations are more stable than bifurcated geometries.

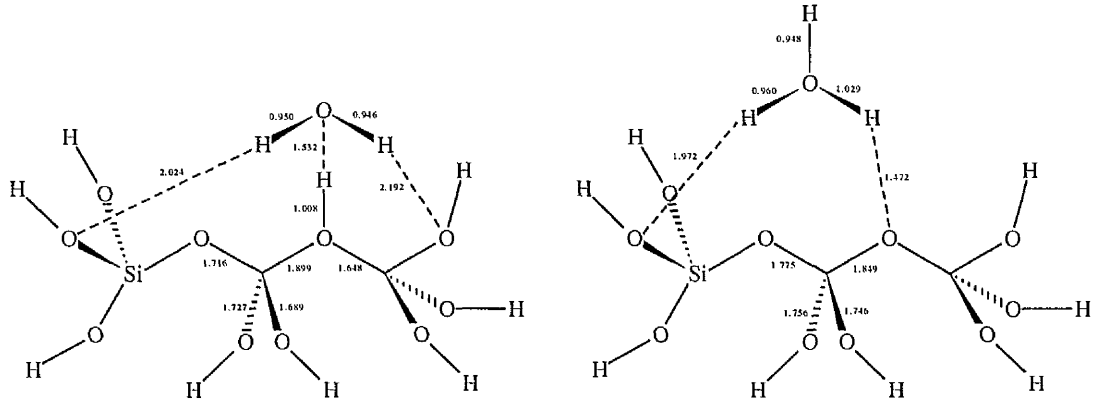

(a) No PDC field *(b) 3-21G PDC field*

figure 3.12 - Stationary points determined at the 3-21G(*) basis set, starting from hydroxonium ion and T3 Si-OH terminated anionic zeolite.*

3.5 - Conclusions

The use of bare cluster models in the representation of zeolite properties, including electrostatics, interaction energetics and geometry has been shown to provide results which can be substantially improved by the simple inclusion of an embedding scheme. This scheme has the benefit of being based on the familiar bare cluster model, yet providing a demonstrably enhanced representation of the zeolite properties

Although the embedded cluster model as described relies on a somewhat subjective and arbitrary choice of both sampling and fitting grids, the method has been shown to be remarkably tolerant of the grids chosen, with little change in calculated interaction energies, even for moderate sized fitting grids.

Clear improvements in calculated interaction energies upon inclusion of the PDC have also been demonstrated, with clear improvements upon incorporation of two simple cut-off schemes. The removal of sampling grid points in the region of fitting grid sites was found to result in both better calculated interaction energies of a substrate within the model, as well as better results from the fitting procedure. Prevention of excessive polarisation of the zeolite cluster by nearby charges was accomplished by adopting an additional screening procedure in which fitting grid sites close to the terminated cluster were deleted. It has been found that both screening procedures are required for the best representation of the properties of the periodic zeolite.

Whilst zeolite cluster geometry is seen to be better represented within an embedded cluster model, preliminary binding studies of water at the 3-21G(*)* basis set

showed the formation of extremely interesting interaction geometries, substantially different from those determined in previous studies[24]. In the next chapter, structural and catalytic properties calculated using the embedded cluster model of the industrially important zeolite Y are reported.

3.6 - References

[1] Vetrivel, R.; Catlow, C. R. A.; Colbourn, E. A., *Proc. R. Soc. London (A)*, **1988**, 417, 81

[2] Vetrivel, R.; Catlow, C. R. A.; Colbourn, E. A., *J. Am. Chem. Soc.*, **1989**, 93, 4594

[3] White, J.; Hess, A. C., *J. Phys. Chem.*, **1993**, 97, 8703

[4] White, J. C.; Hess, A. C., *J. Phys. Chem.*, **1993**, 97, 6398

[5] Kassab, E.; Seiti, K.; Allavena, M., *J. Phys. Chem.*, **1991**, 95, 9425

[6] Pisani, C.; Dovesi, R.; Nada, R.; Kantorovich, L. N., *J. Chem. Phys.*, **1990**, 92, 7448

[7] Pisani, C.; Orlando, R.; Corá, F., *J. Chem. Phys.*, **1992**, 97, 4195

[8] Kramer, G. J.; van Santen, R. A.; Emeis, C. A.; Nowak, A. K., *Nature*, **1993**, 363, 529

[9] Sauer, J., *Chem. Rev.*, **1989**, 89, 199

[10] Gaussian 92, Revision A, M. J. Frisch, G. W. Trucks, M. Head-Gordon, P. M. W. Gill, M. W. Wong, J. B. Foresman, B. G. Johnson, H. B. Schlegel, M. A. Robb, E. S. Replogle, R. Gomperts, J. L. Andres, K. Raghavachari, J. S. Binkley, C. Gonzales, R. L. Martin, D. J. Fox, D. J. Defrees, J. Baker, J. J. P. Stewart and J. A. Pople, Gaussian, Inc., Pittsburgh PA, 1992.

[11] GAMESS-UK is a package of *ab initio* programs written by M. F. Guest, J. H. van Lenthe, J. Kendrick, K Schoffel, P. Sherwood and R. J. Harrison, with contributions from R. D. Amos, R. J. Buenker, M. Dupuis, N. C. Handy, I. H. Hillier, P. J. Knowles, V. Bonacic-Koutecky, W. von Niessen, V. R. Saunders and A. J. Stone. The package is derived from the original GAMESS code due to M. Dupuis, D. Spangler and J. Wendoloski, NRCC Software Catalog, Vol. 1, Program No. QG01 (GAMESS), 1980.

[12] Hehre, W. J.; Radom, L.; Schleyer, P. v. R.; Pople, J. A., *"Ab Initio Molecular Orbital Theory"*, Wiley-Interscience, New York, **1985**

[13] Barrer, R. M.; Cole, J. F.; Villiger, H., *J. Chem. Soc. A.*, **1970**, 1523

[14] Hehre, W. J.; Stewart, R. F.; Pople, J. A., *J. Chem. Phys.*, **1969**, 51, 2657

[15] Pietro, W. J.; Francl, M. M.; Hehre, W. J.; DeFrees, D. J.; Pople, J. A.; Binkley, J. S., *J. Am. Chem. Soc.*, **1982**, 104, 5039

[16] Binkley, J. S.; Pople, J. A.; Hehre, W. J., *J. Am. Chem. Soc.*, **1980**, 102, 939

[17] Gordon, M. S.; Binkley, J. S.; Pople, J. A.; Pietro, W. J.; Hehre, W. J., *J. Am. Chem. Soc.*, **1982**, 104, 2797

[18] Francl, M. M.; Pietro, W. J.; Hehre, W. J.; Binkley, J. S.; Gordon, M. S.; DeFrees, D. J.; Pople, J. A., *J. Chem. Phys.*, **1982**, 77, 3654

[19] Saunders, V. R.; Hillier, I. H., *Int. J. Quant. Chem.*, **1973**, 7, 699

[20] Brand, H. V.; Curtiss, L. A.; Iton, L. E., *J. Phys. Chem.*, **1993**, 97, 12773

[21] Ugliengo, P.; Saunders, V. R.; Garrone, E., *J. Phys. Chem.*, **1989**, 93, 5210

[22] Sauer, J., *J. Phys. Chem.*, **1987**, 91, 2315

[23] Campana, L.; Selloni, A.; Weber, J.; Pasquarello, A.; Papai, I.; Goursot, A., *Chem. Phys. Lett.*, **1994**, 226, 245

[24] Sauer, J.; Horn, H.; Häser, M.; Ahlrichs, R., *Chem. Phys. Lett.*, **1990**, 173, 26

Chapter 4

Studies of catalysis in Zeolite Y

4.1 - Introduction

Many industrially important chemical processes occur in zeolite Y, and as a consequence, much experimental data exist concerning the behaviour of substrates interacting with it. The interactions of water[1], methanol[2] and ammonia[3] are frequently studied as they provide an increasing scale of proton affinity which can be used as a means of probing the proton transfer from the acidic Brønsted site. The nature of the substrate within the zeolite cavity, whether neutral or protonated, depends on the balance between the proton affinity of the anionic zeolite, the proton affinity of the substrate, and the degree of stabilisation which occurs on binding the substrate to the zeolite framework. It has been suggested that the vibrational spectra and NMR shifts of substrates within the zeolite can be used as a sensitive measure of the degree of proton transfer, and hence the acidity of the zeolite[4,5,6,7], though there is debate over the assignment of bands in the spectra of adsorbed water which have been used as evidence for both chemisorption[5] and physisorption[8,9]. Because of the range of experimental information which exists for the interaction of substrates with zeolite Y, it provides a suitable system with which to judge the quality of models. This chapter will be concerned with the study of both framework properties and the properties of substrates bound within zeolite Y, comparing the predictions of the embedded cluster model described in chapter 3 with the bare cluster approach.

To determine the optimum cluster size and termination method for embedded cluster studies, clusters of three different sizes have been considered. Firstly, the geometric and vibrational properties of the crystallographically distinct oxygen sites

within zeolite Y have been studied using T3 clusters with Si-OH termination. Secondly, the interaction of water, methanol and ammonia substrates with a T3 cluster using the Si-H termination procedure, including the effects of electron correlation using both perturbative and density functional methods, was considered. Finally, the effects of higher basis sets were investigated by consideration of the sorption of ammonia and the geometric properties of a smaller T2 cluster, using the Si-OH termination procedure.

4.2 - Periodic Hartree-Fock study of zeolite Y

The framework of zeolite Y, shown in figure 4.1, is comprised of sodalite cages interconnected through their hexagonal faces *via* double-6 ring SBU's, giving rise to a very open framework topology containing 'supercages'. It is the interaction of substrate molecules, and particularly bases, within the larger cage system which is of primary interest to us since it offers better accessibility than the restricted small sodalite cages.

Prior to the determination of a set of point charges for use in embedded cluster studies of zeolite-substrate interactions, a periodic Hartree-Fock study of zeolite Y was performed. For the purposes of the PHF calculation, the Fd3m space group crystal structure for zeolite Y[10,11] was converted to a purely siliceous form to allow the sodium counterions associated with the aluminium sites to be neglected. Additionally, an extra-framework water oxygen site at the reciprocal space origin was omitted to give an asymmetric unit containing one silicon and four oxygens.

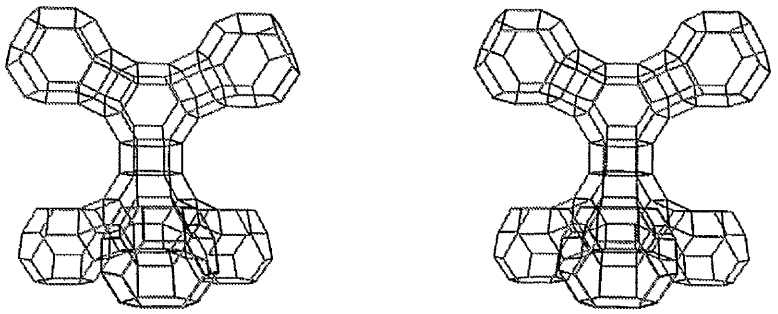

figure 4.1 - Stereoview showing the zeolite Y structure (oxygens omitted for clarity).

In view of the fact that zeolite Y can exist with Si:Al ratios greater than 30, with very little framework reorganisation[12] (typical changes in the unit cell of the order 1 to 1.5%), the neglect of the aluminium and counterions is justified. Zeolite Y in the siliceous form used here has a large primitive cell containing 144 atoms. As a consequence, the highest basis set which could be used for the PHF calculation, limited by the available on-line disk resources, was 3-21G.

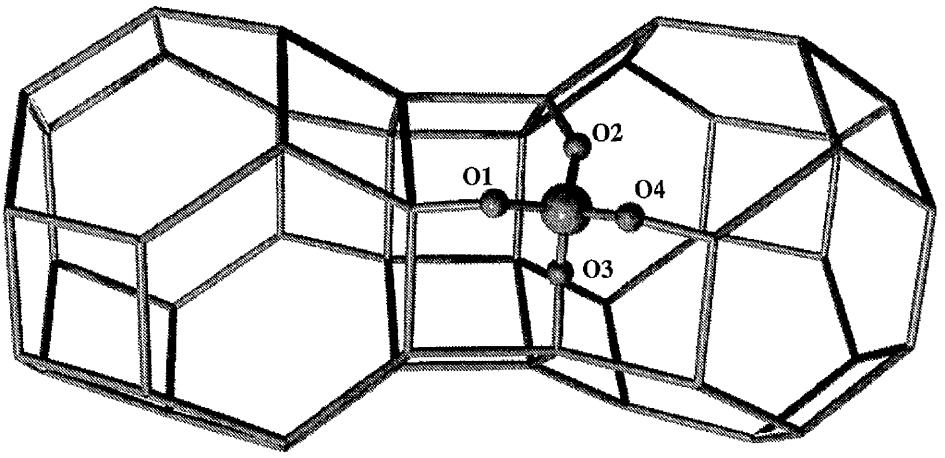

figure 4.2 - The four crystallographically distinct oxygen sites in relation to a sodalite cage and D6R SBU of zeolite-Y

In the form described above, zeolite Y has only 1 type of T site, each of which has 4 crystallographically distinct oxygen neighbours. The position of these 4 oxygen sites, using the numbering system adopted elsewhere[6] is shown as figure 4.2.

The periodic Hartree-Fock calculation was performed using parameters of 5, 5, 5, 6 and 12 for the real space ITOL values, and 4 for RTOL 1, the reciprocal space shrinking factor, with other important computational parameters set at the defaults. Wavefunction convergence was specified as 10^{-7} in both the energy and eigenvalues, with level shifting of 10^{-3} Hartree applied to accelerate convergence. After 11 cycles, the final SCF energy was -20955.4238 Hartree, with Mulliken populations on the four oxygen sites, O1-O4 in figure 4.2, of 9.07, 9.08, 9.13, 9.09, respectively and 11.81 at the silicon T sites.

4.3 - Si-OH terminated T3 clusters

4.3.1 - Cluster selection and fitting details

We now consider properties of the crystallographically distinct sites of zeolite Y through the use of T3 clusters using the Si-OH termination procedure. For these calculations, two T3 clusters were selected, each containing 2 of the 4 possible bridging sites at which protonation could occur. In this way, only 2 different sets of point charges need to be evaluated for the study of all 4 bridging oxygen sites. The clusters were terminated using the Si-OH scheme, which has been found in chapter 3 to provide the

best representation of the properties of the periodic zeolite. The resulting clusters, having stoichiometry $Si_3O_{10}H_8$, and their relation to the primitive cell of zeolite Y are shown in figure 4.3.

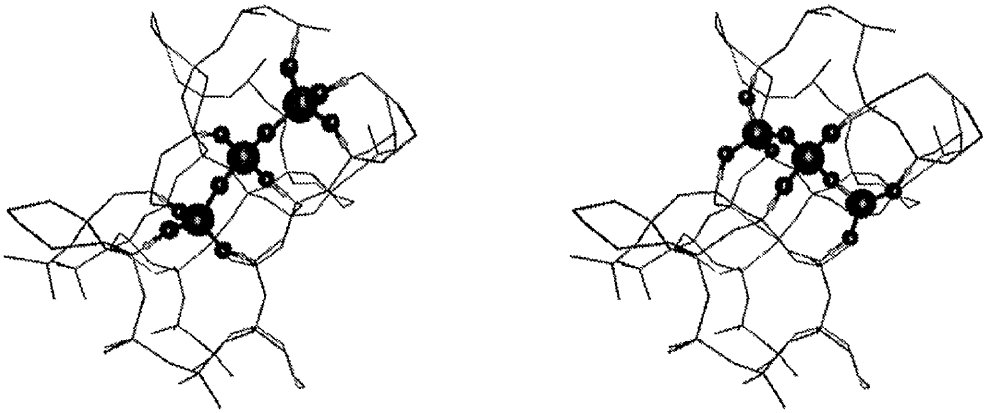

(a) C_{14} cluster. *(b) C_{23} cluster.*

figure 4.3 - Zeolite Y primitive cell with selected clusters[†] .

The use of the 3-21G basis set for the periodic Hartree-Fock calculation and the subsequent need to perform the embedded cluster modelling using the same basis set, to ensure consistency in the point charges, allowed the use of relatively large T3 clusters. In the same manner as for the cancrinite calculations used in the calibration of the model, additional polarisation functions, important in obtaining accurate representation of the cluster bonding, were incorporated into the subsequent cluster optimisations. The two clusters are referred to henceforth as C_{14}, shown in figure 4.3(a), and C_{23}, shown in figure 4.3(b), co-ordinates of which are included as appendix B(1) and B(2) respectively.

[†] The nomenclature adopted for the clusters indicates the pair of oxygen sites through which the cluster passes. Thus, C_{14} denotes the cluster containing the 1 and 4 oxygen sites, using the numbering shown in figure 4.2.

The details of the fitting procedure have been described in chapter 3, and will only be outlined here. The central T site in both the C_{14} and C_{23} clusters was used as the origin of a sphere of crystal sites at which the fitting grid points were sited. The sampling volume for both the C_{14} and C_{23} clusters, (co-ordinates of the corners of which are included as appendix B(3) and B(4), respectively), used an 18 x 18 x 18 grid. The fitting procedure was carried out with the total charge constrained to zero, but no dipole constraint was imposed. The screening cut-offs for the sampling and fitting grids were also used here. It was decided that a sphere of crystal sites of radius 17 bohr would be used for the subsequent embedded cluster optimisations, as it provided the best balance between the standard deviation of the potential and the absolute magnitude of the charges.

The effect of the correcting charges on both the geometrical and vibrational properties of the zeolite clusters can be investigated by optimising the acidic site region of each of the clusters which result from protonation at the O1, O2, O3, and O4 sites in turn, with and without the PDC field. In order to ensure that the cluster was orientated correctly with respect to the point charge field and that the electronic structure of the cluster was correctly maintained during the geometry optimisation, the constrained optimisation scheme was applied here (see chapter 3). Only a small region of the cluster near the acidic site was relaxed, corresponding to allowing the central T site and all 4 attached oxygen sites, as well as the acidic hydrogen, to have complete freedom, allowing all associated lengths, angles and dihedrals to optimise, whilst fixing the positions of the other atoms.

Optimisation of each of the four clusters, generated by isomorphously replacing the central silicon of each of the two clusters with aluminium and protonating each of the O1, O2, O3 and O4 sites, was carried out within the constrained optimisation scheme described above. In all cases, the 3-21G(*)* basis set was used. Harmonic vibrational frequencies, ν_{OH}, were determined *via* a finite-differences method using displacements of 0.002 bohr. It is assumed that the zeolite cluster is of large mass, enabling the reduced mass of the system, μ, to be given by the mass of the proton. The vibrational frequency of the acidic O-H group was then calculated within the simple harmonic approximation.

$$\nu_{OH} = \frac{1}{2\pi c}\sqrt{\frac{k}{\mu}} \qquad (4.1)$$

To ensure accurate vibrational frequencies, high accuracy integral generation was specified, along with a more stringent SCF convergence tolerance of 10^{-8} Hartree. In subsequent discussion, optimised cluster geometries, with or without the PDC field, refer to figure 4.4. A subscript, OH, after an oxygen denotes it as the bridging oxygen to which the acidic proton is attached. Thus, Al-O represents the distance between the aluminium and the non-Brønsted oxygen, whereas Al-O_{OH}-Si refers to the angle between the aluminium, the Brønsted bridging oxygen and the attached (fixed) silicon.

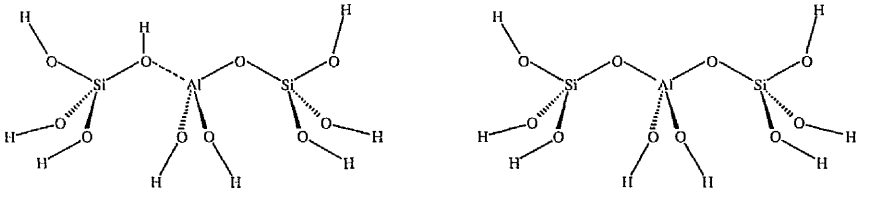

(a) Acidic cluster. *(b) Anionic cluster.*

figure 4.4 - Si-OH terminated T3 clusters.

4.3.2 - Computational results

	$H\text{-}O_{OH}$[a]	$Al\text{-}O_{OH}$	$Si\text{-}O_{OH}$	$Al\text{-}O_{OH}\text{-}Si$	$Al\text{-}O_{OH}\text{-}H$	$Si\text{-}O_{OH}\text{-}H$
O1/3-21G(*)*/NONE[b]	0.945	1.873	1.666	121.5	116.7	120.3
O1/3-21G(*)*/3-21G	0.947	1.858	1.663	119.1	120.4	119.7
O2/3-21G(*)*/NONE	0.948	1.903	1.675	131.7	107.0	121.3
O2/3-21G(*)*/3-21G	0.944	1.846	1.669	122.3	117.6	117.9
O3/3-21G(*)*/NONE	0.953	1.877	1.648	139.4	97.6	122.3
O3/3-21G(*)*/3-21G	0.949	1.874	1.661	132.2	107.9	116.7
O4/3-21G(*)*/NONE	0.948	1.892	1.659	130.8	108.8	120.2
O4/3-21G(*)*/3-21G	0.951	1.897	1.660	126.5	110.6	126.5

table 4.1 - Optimised geometrical parameters for acidic clusters.

[a] *Labelling refers to figure 4.4(a).*

[b] *The nomenclature adopted here denotes the oxygen site at which protonation occurs, followed by the basis at which the PDC field, if appropriate, was derived.*

	$Al\text{-}O_{OH}$[a]	$Si\text{-}O_{OH}$	$Al\text{-}O_{OH}\text{-}Si$
O1/3-21G(*)*/NONE	1.748	1.577	136.5
O1/3-21G(*)*/3-21G	1.735	1.582	128.4
O2/3-21G(*)*/NONE	1.752	1.586	145.1
O2/3-21G(*)*/3-21G	1.719	1.582	131.5
O3/3-21G(*)*/NONE	1.752	1.576	149.4
O3/3-21G(*)*/3-21G	1.757	1.580	147.4
O4/3-21G(*)*/NONE	1.738	1.565	142.4
O4/3-21G(*)*/3-21G	1.761	1.567	151.6

table 4.2 - Optimised geometrical parameters for anionic clusters.

[a] *Labelling refers to figure 4.4(b). Subscript OH shows the oxygen to which the Brønsted hydrogen was attached.*

Optimised geometries for each of the clusters, after substitution of Al at the central T site, and the addition of hydrogen at each of the O1-O4 sites are reported in table 4.1 for the acidic clusters and table 4.2 for the corresponding anionic systems.

	Deprotonation energy / kJ mol^{-1}	**ν_{OH} / cm^{-1}[a]**
O1/3-21G(*)*/NONE	1463	3585
O2/3-21G(*)*/NONE	1443	3464
O3/3-21G(*)*/NONE	1416	3523
O4/3-21G(*)*/NONE	1440	3523

table 4.3 - Deprotonation energies and harmonic frequencies for oxygen sites without PDC

[a] Harmonic frequencies scaled by 0.885

	Deprotonation energy[a] / kJ mol^{-1}	**Corrected deprotonation energy[b] / kJ mol^{-1}**	**ν_{OH} / cm^{-1}[c]**
O1/3-21G(*)*/3-21G	1328	1343	3553
O2/3-21G(*)*/3-21G	1104	1439	3552
O3/3-21G(*)*/3-21G	1049	1452	3556
O4/3-21G(*)*/3-21G	1291	1311	3464

table 4.4 - Deprotonation energies and harmonic frequencies for oxygen sites with PDC.

[a] Deprotonation energy with no electrostatic correction.

[b] Deprotonation energy including electrostatic solvation of the acidic hydrogen.

[c] Harmonic frequencies scaled by 0.885.

4.3.2.1 - Cluster geometry

The calculated geometries of the clusters compare well with those suggested by other work, including predictions made by Sauer[13], small cluster calculations[14], a recent Car-Parrinello molecular dynamics simulation of a bulk zeolite[15] and a PHF optimisation of a zeolite acidic site at the STO-3G basis set[16]. The behaviour of the geometries on deprotonation is also consistent with previous studies, with the expected shortening of the Al-O_{OH} bond. Some comparisons with geometries obtained in chapter 3 for cancrinite T3 clusters at the 3-21G(*)* basis set are useful. Firstly, the acidic hydroxyl length, whilst somewhat shorter within zeolite Y, shows the same behaviour observed in cancrinite at this basis, of remaining essentially the same length whether or not PDC are present. Secondly, both the Si-O-H and Si-O-Al angles show the same general behaviour of decreasing upon addition of the PDC field. The Si-O_{OH} distances for the O3 and O4 sites lengthen on addition of PDC, mirroring the behaviour observed within cancrinite, whilst opposite behaviour is exhibited by the O1 and O2 sites. This difference is not, however surprising, given the range of electrostatic environments within zeolites so that the effect of the PDC field may vary in different zeolites, and by extension, why distinct sites within the same zeolite should exhibit different behaviour.

4.3.2.2 - Brønsted site vibrational frequencies

The conventional view on the structure and geometry of acidic sites is that shorter bond lengths are associated with higher harmonic frequencies and higher deprotonation energies. This has been investigated by a number of workers who have observed correlations between the hydroxyl bond length and the harmonic frequency of the Brønsted hydroxyl group[17]. Figure 4.5 shows the harmonic frequency against the bond length of the Brønsted hydroxyl.

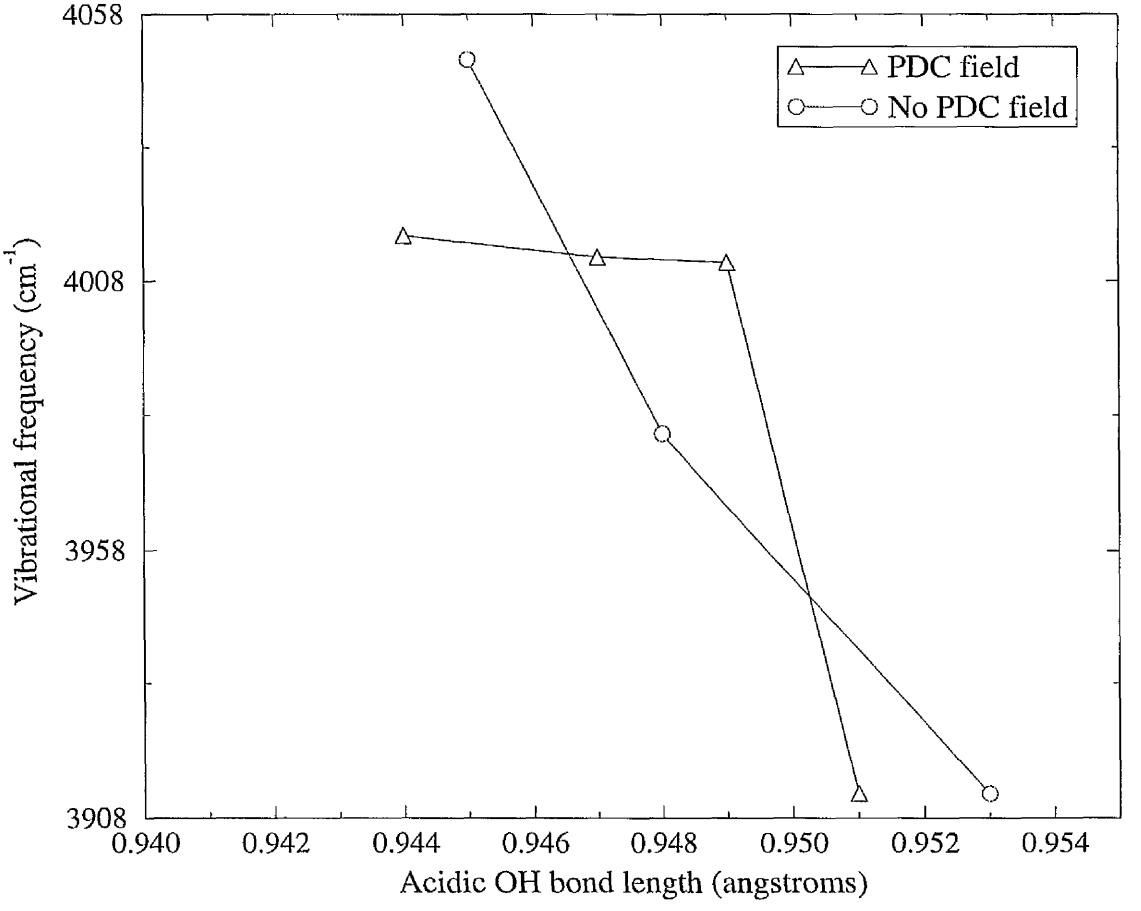

figure 4.5 - Relation between harmonic vibrational frequency of the acidic OH group (cm^{-1}) and OH length (angstrom) with and without PDC.

It is worth noting that we find a lack of any direct correlation between the hydroxyl bond length and the harmonic vibrational frequency for the embedded cluster model. This result is perhaps not surprising in view of the different environments at each of the oxygen sites in the real zeolite, arising through a combination of local geometrical deformations (included in both the PDC and bare clusters) and long-range electrostatic effects, included only in the PDC calculations. Thus, the potential experienced by the acidic proton within the zeolite is not likely to be solely a function of the local geometry of the cluster, and simple correlations should not necessarily be expected.

Experimental determinations have been made of the vibrational spectra of HY zeolites of varying Si:Al ratio[18,19], which may serve to measure the quality of the representations obtained with both the embedded and bare cluster models. OH stretching bands are found experimentally at 3640 cm^{-1} and 3545 cm^{-1} for HY zeolites[8]. Although the Si:Al ratio within the embedded and bare models is considerably higher than in the periodic zeolite, it has been recognised by Barthomeuf[20] that the acid strength of zeolites reaches a maximum at Si:Al ratios ~7. Using this observation, we take the vibrational properties of the highly siliceous zeolite Y used in the cluster calculations to be comparable with those reported for zeolite Y with an Si:Al ratio of 7.02. The calculated vibrational frequencies, after scaling by a factor of 0.885, are summarised in table 4.5 (frequencies taken from table 4.3 and 4.4).

Whilst the scaled frequencies fall substantially below those determined experimentally, regardless of whether the PDC field is present or absent, the difference of 95 cm^{-1} between the high and low-frequency experimental peaks can be observed within the PDC field, though not for the bare clusters. Also, there are essentially only two

distinct frequencies within the embedded cluster model, as in experiment, though three separate frequencies appear without the PDC.

	NO PDC	PDC
O1/3-21G(*)*	3585	3553
O2/3-21G(*)*	3464	3552
O3/3-21G(*)*	3523	3556
O4/3-21G(*)*	3523	3464

table 4.5 - Calculated harmonic vibrational frequencies, in cm^{-1}, for the four crystallographically distinct oxygen sites of zeolite Y, with and without PDC. All frequencies scaled by 0.885.

4.3.2.3 - Deprotonation energies

In all cases considered here, the deprotonation energy, $E_{deprotonation}$, of the oxygen site of the cluster is evaluated as

$$E_{deprotonation} = E_{acidic} - E_{anionic} \qquad (4.2)$$

where E_{acidic} and $E_{anionic}$ are the energies of the geometry optimised acidic and anionic clusters respectively. The deprotonation energies of the bare cluster models (table 4.3) fall well within the range determined experimentally, typically in the range 1300 to 1450 kJ mol^{-1}. It must, however be borne in mind that there is a difference in the embedded and bare cluster models which needs to be addressed. This arises because the proton affinity within the PDC field must take account of an additional contribution from the solvation of the proton by the PDC. This is evaluated as the electrostatic energy, due to

the point charge field in the absence of the cluster, at the position adopted by the proton, calculated simply as

$$E_{solv} = \sum_{i=1}^{n} \frac{q_i}{r_{hi}} \qquad (4.3)$$

where n is the number of point charges, q_i the magnitude of the i'th charge and r_{hi} it's distance from the acidic hydrogen. The importance of this correction can be clearly seen by considering the correlation between the harmonic vibrational frequency of the Brønsted hydroxyl group and the deprotonation energy of the anionic cluster. In the absence of the electrostatic correction, proton affinities determined within the embedded cluster model clearly fail to follow the clear correlation shown by Brand[21] where an increase in the hydroxyl frequency is accompanied by an increase in the proton affinity. This behaviour, where one would intuitively expect a cluster with a higher deprotonation energy to have a more tightly bound Brønsted hydrogen with a high vibrational frequency, is largely given after incorporation of the electrostatic correction.

The same study[21] also considered the behaviour of deprotonation energies as a function of cluster size, observing a decrease in the deprotonation energy with larger clusters. At the 3-21G basis set, the difference in deprotonation energies determined by Brand[21], between small T2 clusters and larger clusters containing 28 T sites was of the order of 50 kJ mol^{-1}. Calculated deprotonation energies within the PDC field, reported in table 4.4, generally fall below those of the bare cluster model, except the O4 site which demonstrates a deprotonation energy some 36 kJ mol^{-1} higher in the embedded cluster, compared to the bare model. In spite of this anomaly, these results do suggest that the embedded model is again more useful than bare clusters.

An experimental study of the Brønsted acidity of hydrogen ultra-stable zeolite Y[22] determined deprotonation energies covering a range of 80±29 kJ mol^{-1}. Calculated deprotonation energies for the four sites within the PDC field span ~140 kJ mol^{-1}, substantially larger than the 47 kJ mol^{-1} range calculated within the bare cluster model. A large cluster semi-empirical study of deprotonation energies of all 48 oxygen sites in H-ZSM-5[23], which provides useful comparison with the highly siliceous zeolite Y structure used, gave a range of 116 kJ mol^{-1}, in better agreement with the embedded cluster results for zeolite Y. The experimental range of deprotonation energies of the oxygen sites in H-ZSM-5[24] is 142 kJ mol^{-1}, again in excellent agreement with the embedded cluster results.

It is worth noting at this point that it is not experimentally possible to directly obtain values for the proton affinity of zeolites and indirect methods are used instead. Typically proton affinities are determined by perturbation of the acidic site with a weak base[22], e.g. CO. The resulting shift (cm^{-1}) in the OH stretch, $\Delta\nu_{OH}$, is correlated with the required proton affinity (kJ mol^{-1}), $E_{pa(Z)}$, *via* an empirical relationship (equation 4.4), to the corresponding values ($\Delta\nu_{OH(SiOH)}$, $E_{pa(SiOH)}$) in SiO_2.

$$E_{pa(Z)} = E_{pa(SiOH)} - 442.5 \log \frac{\left(\Delta\nu_{OH(Z)}\right)}{\left(\Delta\nu_{OH(SiOH)}\right)} \qquad (4.4)$$

4.4 - Si-H terminated T3 clusters

4.4.1 - Cluster selection and fitting details

We now describe calculations of the interaction of water, methanol and ammonia with Si-H terminated T3 clusters. Due to the computational cost associated with the use of Si-OH terminated T3 clusters, especially when substrates are included in the geometry optimisation, a compromise was made in using Si-H terminated T3 clusters. It has been shown in chapter 3, however, that Si-H clusters are only slightly inferior to Si-OH terminated ones when compared with the properties of the periodic zeolite. The Si-H terminated T3 cluster selected is shown in figure 4.6, in relation to the zeolite Y primitive cell.

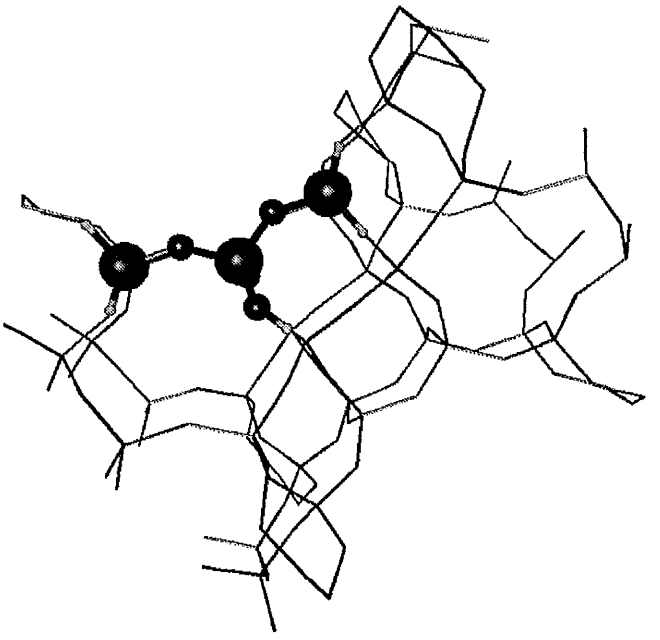

figure 4.6 - Si-H terminated T3 cluster in relation to the zeolite Y primitive cell.

Our primary interest is the degree to which protonated species are stabilised within the channel of zeolite Y, and the implications of the modification of the electrostatics using the embedded cluster model. For convenience, each of the optimisations was started from the anionic zeolite with the protonated substrate in an appropriate doubly hydrogen bonded binding geometry of the type found by other workers[25], to search for a stationary point corresponding to the chemisorbed system. For these calculations the interaction of water, ammonia and methanol with the zeolite Y O1 site, which offers the best access to substrates within the supercage, was considered. Geometry optimisations were performed both at the 3-21G and 6-31G** basis set level with binding energies evaluated at both the Hartree-Fock and correlated levels. The effect of the presence of point charges was examined at each of these levels.

The cluster used (co-ordinates in appendix B(5)), shown in relation to the zeolite Y primitive cell in figure 4.6, was terminated using the Si-H scheme described in chapter 3, giving a cluster of stoichiometry $Si_3O_4H_8$. The sampling grid, co-ordinates in appendix B(6), contained 5832 points, on an 18 x 18 x 18 grid, prior to screening. The cut-off parameters used were those described in chapter 3. The fitting grid was defined as a sphere of radius 15 bohr of crystal sites within the zeolite Y framework, using the central T site of the cluster as the origin. This fitting grid was chosen as it provided the best balance between the standard deviation of the potential and the absolute magnitude of the resultant fitted charges. After screening, the sampling grid contained 4815 points, with 67 fitting grid sites remaining.

4.4.2 - Cluster optimisations

Constrained optimisations were performed on both the acidic and anionic forms of the Si-H terminated T3 cluster. The central T site (AlO_4) at which aluminium substitution was carried out, and the Brønsted hydrogen, where appropriate, were allowed full freedom to optimise. It is worth noting that we were unable to perform the PHF calculation at the 6-31G** level, so the PDC used for the embedded cluster optimisations at the 6-31G** level are those determined with the 3-21G basis set. Optimised geometries for the clusters are reported as table 4.6 and 4.7.

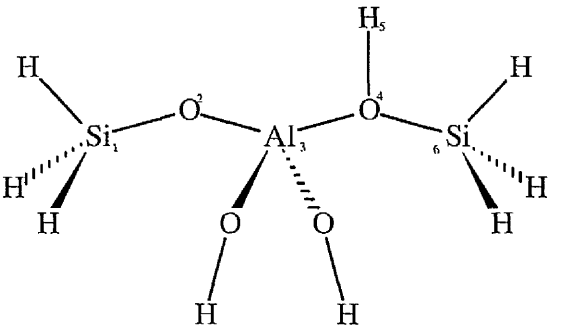

figure 4.7 - Si-H terminated T3 cluster.

	Si_1-O_2	O_2-Al_3	Al_3-O_4	O_4-H_5	O_4-Si_6
3-21G/NONE	1.639	1.694	1.834	0.967	1.715
3-21G/3-21G	1.647	1.706	1.839	0.970	1.715
6-31G/NONE**	1.614	1.716	1.948	0.949	1.683
6-31G/3-21G**	1.632	1.745	1.932	0.952	1.697

table 4.6 - Optimised bond lengths for acidic forms of clusters - numbering corresponds to figure 4.7.

	Si_1-O_2	O_2-Al_3	Al_3-O_4	O_4-Si_6
3-21G/NONE	1.606	1.705	1.722	1.617
3-21G/3-21G	1.630	1.733	1.727	1.634
6-31G/NONE**	1.584	1.752	1.768	1.589
6-31G/3-21G**	1.609	1.808	1.760	1.601

table 4.7 - Optimised bond lengths for anionic forms of clusters - numbering corresponds to figure 4.7.

It is useful to compare the results for the Si-H terminated clusters with those previously obtained using the Si-OH termination procedure. Although both basis set and PDC field differ in these two cases, the changes in geometry obtained upon deprotonation, from the acidic to the anionic form of the zeolite, may indicate the robustness of the method.

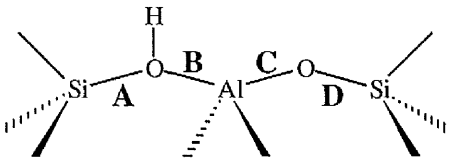

figure 4.8 - Schematic representation of cluster backbone and bond lengths used in comparison.

	A	B	C	D
3-21G(*)*/Si-OH(NONE)	-0.089	-0.124	+0.032	-0.023
3-21G/Si-H(NONE)	-0.098	-0.112	+0.011	-0.033
3-21G(*)*/Si-OH(PDC)	-0.081	-0.123	+0.052	-0.014
3-21G/Si-H(PDC)	-0.081	-0.112	+0.027	-0.017

table 4.8 - Changes, in bond lengths (shown in figure 4.8) on deprotonation for different models in the presence and absence of PDC.

The changes in the bond lengths upon deprotonation are very similar for both termination procedures and basis sets, suggesting that our use of the smaller cluster is justified. We now describe calculations of substrate-zeolite interactions using such an Si-H termination procedure.

4.4.3 - Interaction of water with zeolite Y T3 clusters

We first describe results at the smaller 3-21G basis set level. The structures resulting from the geometry optimisations are shown in figure 4.9 (co-ordinates in appendix B(7) and B(8), respectively).

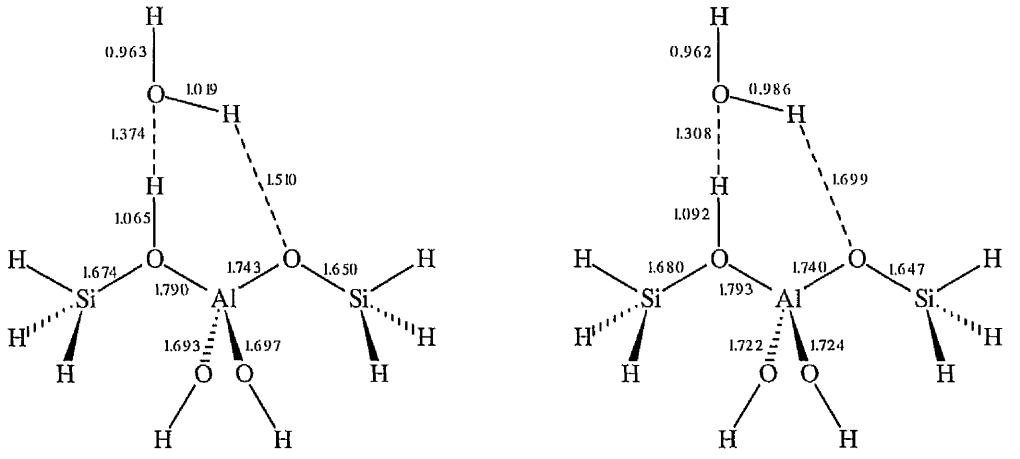

(a) 3-21G/NONE. *(b) 3-21G/3-21G.*

figure 4.9 - Optimum 3-21G geometries for the zeolite Y-water system.

The bifurcated hydrogen bonding motif for water found in previous work[25] was obtained, both with and without the PDC field. However, no stationary point corresponding to a bound hydroxonium ion could be found, either with or without the PDC field. This contrasts with the very different binding geometries obtained in cancrinite, where binding occurred to oxygen atoms in the terminal regions of the cluster. Such interactions are of course only possible with Si-OH and not Si-H terminated clusters. Both with and without the PDC field, the incorporation of water resulted in lengthening of the Brønsted O-H bond, with an associated shortening of the Al-O_H bond.

Although both structures exhibit a pair of hydrogen bonds, their geometry is somewhat different. Within the point charges, the hydrogen bond between the water oxygen and the hydrogen of the Brønsted site is somewhat shorter than that found in the bare system, though the other hydrogen bond is longer than that in the bare cluster model, by almost 0.2 Å, with other geometric parameters remaining comparable.

Using these structures, binding energies were calculated at the Hartree-Fock level using both the 3-21G and 6-31G** basis sets, and including correlation effects at the density functional theory level using a B-LYP functional (chapter 2). Substantial difference between the interaction energies evaluated at the 3-21G and 6-31G** basis set levels are found (table 4.9) and can be attributed to a number of factors. Firstly, the 3-21G basis set is particularly prone to substantial basis set superposition errors which affect calculated interaction energies. A second, and perhaps less important effect, is that the use of 6-31G** single-point energies calculated at the 3-21G geometries will contain errors, particularly in the deprotonation energy of the zeolite, resulting from the geometries being non-optimal.

	3-21G	**6-31G****	**6-31G**/B-LYP**
3-21G/NONE[a]	-130.4	-42.0	-92.9
3-21G/3-21G[a]	-115.2	-28.2	-70.6
6-31G/NONE[a]**	-	-61.8 (12.2)	-86.2
6-31G/3-21G[a]**	-	-56.1 (8.8)	-71.4

*table 4.9 - Binding energies for water, in kJ mol^{-1}, evaluated at the 3-21G and 6-31G** optimised geometries. BSSE corrections in parentheses. Column headings denote level at which energy evaluation was performed.*

(a) Optimisation level

Optimisations were then carried out using a 6-31G** basis. At the higher basis set, whether or not PDC were present, there was a distinct change in the binding motif of the substrate molecule, shown in figure 4.10 (co-ordinates in appendix B(9) and B(10)). The hydrogen bond from the oxygen of the water to the hydrogen of the framework underwent a substantial lengthening from ~1.3 Å at the 3-21G basis set to ~1.7 Å at 6-31G**. In the presence of the PDC field, only a single hydrogen bond formed, from the oxygen of the water to the Brønsted hydrogen. The negligible lengthening of the acidic hydroxyl group within the PDC, relative to that of the acidic cluster, shows this stationary point to have no hydroxonium character. In contrast, without PDC, the bifurcated geometry of previous studies was generated. The two hydrogen bond lengths of 1.677 Å and 1.979 Å obtained in the absence of PDC are very similar to those obtained by Sauer[25], where the use of a DZP basis gave lengths of 1.698 Å and 2.05 Å for a similarly sized cluster. The substantial lengthening of the acidic hydroxyl without the PDC, and the simultaneous shortening of the Al-O bond suggests a greater degree of proton transfer than within the embedded model, and more hydroxonium ion character in the bound substrate. Additional optimisations were performed, starting from the protonated form of the substrate and the anionic zeolite, to search for the existence of stationary points corresponding to binding of a hydroxonium ion. Whether or not the PDC field was present, no such stationary point could be located.

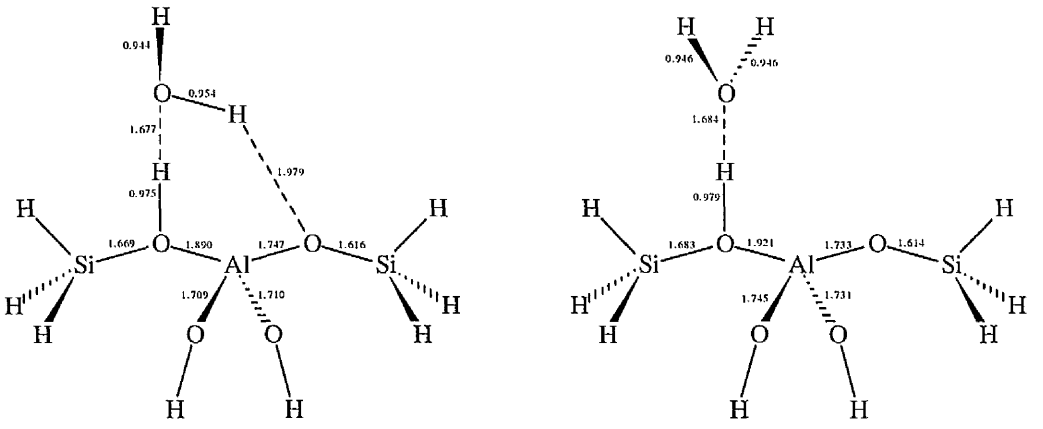

*(a) 6-31G**/NONE.* *(b) 6-31G**/3-21G.*

*figure 4.10 - Optimised water geometries at 6-31G** in the presence and absence of PDC.*

Calorimetric data for the adsorption of water on zeolites gives binding energies of 51±4 kJ mol^{-1} on H-ZSM-5[26], close enough in composition to the highly siliceous zeolite Y studied here to provide useful comparison, in light of the lack of thermodynamic data for water interaction on Y zeolites. There is sufficient uncertainty in the quality of the geometries obtained at the 3-21G basis set, with substantially different binding geometries obtained at the extended 6-31G** basis set level, that the former be treated with caution.

At both the 3-21G and 6-31G** level, the binding energy is greater without the PDC (table 4.9). At the 6-31G** geometries, this effect can be clearly attributed to the different binding motifs adopted by the substrate, with the doubly hydrogen-bonded structure obtained in the absence of the PDC field the more strongly bound. The effect of including electronic correlation effects is to increase the calculated binding energies in all

cases, though somewhat less in the presence of the PDC field (table 4.9). The inclusion of correlation is seen to be particularly important for the 3-21G optimised geometries where the calculated binding energies are increased by some 50 kJ mol^{-1}. Whilst a number of effects have been neglected, particularly zero point terms, the binding energies obtained in the absence of the PDC field appear to be systematically too high when compared with experiment, whilst the embedded cluster model fares substantially better. Estimates of the magnitude of the basis set superposition error (BSSE) were calculated at the Hartree-Fock level for the 6-31G** optimised geometries using the standard counterpoise correction (CPC) method of Boys[27]. Here, the CPC is given by

$$E_{CPC} = \left(E^{B}_{cluster} + E^{B}_{substrate}\right) - \left(E^{S}_{cluster} + E^{S}_{substrate}\right) \qquad (4.5)$$

Where $E^{B}_{cluster}$ and $E^{B}_{substrate}$ are the energies of the cluster and substrate respectively, at the geometries adopted within the zeolite-substrate complex. $E^{S}_{cluster}$ and $E^{S}_{substrate}$, are the corresponding energies in the presence of the basis functions of both cluster and substrate. After modification of the binding energies by the BSSE, the embedded cluster model shows substantially better agreement with experiment than the bare cluster model. The relatively small BSSE corrections, which have only been evaluated at the Hartree-Fock level for the optimised 6-31G** structures, are reported in table 4.9. It should be remembered, however that zero-point effects are still neglected and the experimental binding energies correspond to a different zeolite.

The vibrational spectra of water and methanol adsorbed on acidic zeolites show a triplet of bands at 2900-2800, 2550-2400 and 1700-1600 cm^{-1}. Two distinct interpretations have been proposed which lead to different conclusions about the nature

of the adsorbed substrate. One interpretation assumes the formation of protonated species, H_3O^+ and $CH_3OH_2^+$, with the spectral features due to the motion of the two hydrogens of the protonated species, due to the symmetric and antisymmetric H-O-H stretch and H-O-H bend of the substrate, respectively. An alternative interpretation assigns the three bands in terms of the so-called A-B-C pattern, well known for strong hydrogen-bonded complexes[9]. This effect arises from resonant interactions between the ν(OH) stretch and the δ(OH) and γ(OH) overtones of the strongly perturbed Brønsted hydroxyl group. In view of the failure to determine any stationary points corresponding to the zwitterionic structure in any of the calculations described previously, the latter explanation is favoured.

Using the geometries described previously, we now report calculated vibrational properties of water bound within zeolite Y at both the 3-21G and 6-31G** levels. At the 3-21G level, two hydrogen-bonds are formed whether or not the PDC are present. It would be expected that the calculated frequencies with no PDC field, where a substantial lengthening (~0.05 Å) of one of the water OH groups is observed (figure 4.9), would differ considerably from those of isolated water. In contrast, frequencies calculated within the PDC field, where there is substantially less disparity in the two OH bond lengths of the water (figure 4.9), would be expected to be closer to those of isolated water. With no PDC field at the 6-31G** basis set level, there is a lengthening (~ 0.01 Å) of the water OH bond directed toward the framework (figure 4.10). In the presence of the PDC field, however both OH bonds of the bound water are the same length and neither interacts with the zeolite framework, suggesting the calculated frequencies should be essentially those of isolated water.

Although it is not possible to characterise the nature of stationary points within the constrained optimisation scheme adopted, a study of the vibrational properties of the sorbed species within the zeolite can provide useful comparison with experimental data. A calculation of the second derivatives of the energy for the entire zeolite-substrate system would prove unnecessarily costly, so an alternative method was applied instead. In this procedure, the substrate and Brønsted hydrogen were considered to be vibrating against the zeolite, considered as an essentially fixed, infinite mass. Within this approximation, it was possible to generate a Hessian for the subset of the system under study by successively displacing each atom a fixed distance (0.002 bohr in this instance) along each axis, determining analytically the set of gradients at the displaced geometry. Finite-differences of the analytical gradients were then used in the generation of the Hessian. This method has the advantage that the presence of the zeolite is reflected in the Hessian, *via* the gradients, though the vibrational analysis can be considered simply as a treatment of the isolated protonated substrate. The presence of the zeolite framework, however removes the translational and rotational invariance of the protonated substrate and we assume that these modes are small enough to allow them to be projected out.

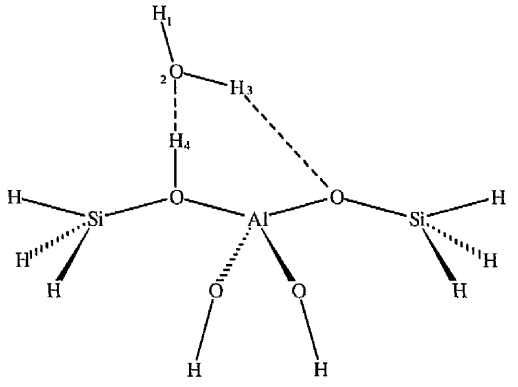

figure 4.11 - Atom numbering for adsorbed water.

	3-21G/NONE	3-21G/3-21G	6-31G**/NONE	6-31G**/3-21G
O_2-H_1 stretch	3943	3979	4205	4228
O_2-H_3 stretch	2990	3528	4011	4123
O_2-H_4 stretch	1810	1868	3249	3197
H_1-O_2-H_3 bend	1599	1452	1780	1774

*table 4.10 - Unscaled harmonic frequencies, in cm^{-1}, at 3-21G and 6-31G** geometries for adsorbed water. Numbering corresponds to figure 4.11.*

Whilst the zeolitic OH stretch does not appear as an internal co-ordinate within the scheme used, the stretching frequencies of the adsorbed water provide useful comparison with experiment. The zeolite HY is unstable and is readily hydrolysed by water vapour at concentrations of greater than a single water molecule per zeolite aluminium, resulting in a loss of Brønsted acidity. A study of the interaction of water with HY by Parker[8] gave a peak at 3745 cm^{-1}, assigned to the hydroxyl stretch of the water directed away from the zeolite framework. This vibration is observed in both the bare and embedded cluster models, and can be used to determine scaling factors appropriate for both systems. After scaling the frequencies, the water bending mode in both the bare and embedded cluster systems were substantially lower than that observed experimentally at 1636 cm^{-1}. The implication of this finding, reinforced by the substantial differences in binding geometry obtained at the 6-31G** basis set, is that the geometries determined at the 3-21G basis set are not sufficiently realistic that they be used to compare with experiment or comment on the differences in binding geometry resulting from the presence or absence of the PDC field. At the 6-31G** basis set level, shifts of

the water OH stretching frequencies from the OH stretches of isolated water can be used as a measure of the strength of hydrogen bonding to the framework and provide useful comparison with experiment. When no PDC field is present, the slight lengthening of the water hydroxyl involved in hydrogen-bonding to the framework is accompanied by a decrease in the stretching frequency. In the presence of the PDC field, however there is a lack of hydrogen bonding interactions between the water OH groups and the zeolite. The calculated frequencies for the sorbed water molecule, given in table 4.10, were indeed found to be closer to the OH stretches at 4264 and 4147 cm^{-1} calculated for isolated water. The adsorbed water is perturbed to such a small degree that there is considerable coupling between the symmetric and antisymmetric OH stretching modes, as observed in isolated water. In all other cases, the water is sufficiently perturbed that this coupling is not observed and the OH stretching modes correspond to single, pure internal co-ordinates. It should be noted that experimental spectra contain frequencies which correspond to perturbed water OH stretches which clearly cannot be produced by the model at the 6-31G**/3-21G level. Thus, it appears that the embedded cluster model, fails to describe the adsorption geometry of the water molecule satisfactorily. This is a problem of cluster models in general, however and no model has yet proved capable of providing both accurate calculated binding energies and vibrational frequencies. The effect of the PDC on the binding geometry adopted by the adsorbed substrate molecule has been found to be quite substantial, and the use of a consistent set of PDC determined at the 6-31G** basis set level may provide substantially different binding geometries. Geometry optimisation at a correlated level may also be required to correctly model the zeolite-substrate interaction.

4.4.4 - Interaction of methanol with zeolite Y T3 clusters

We now report calculations in which the interaction of a methanol substrate with zeolite Y is considered. We first report optimised geometries determined at the 3-21G basis set level. Only stationary points corresponding to physisorbed methanol are obtained, whether or not the PDC field is incorporated (figure 4.12 - co-ordinates in appendix B(11) and B(12)). The optimised geometries show a doubly hydrogen bonded motif for the bare cluster model and a single hydrogen bond interaction for the embedded cluster model. The presence of only a single hydrogen bond is a somewhat surprising result, contrary to the results of previous calculations[28]. In order to ensure that the novel singly hydrogen bonded interaction motif exhibited by methanol within the PDC field at 3-21G does not have a lower energy bifurcated counterpart, the doubly hydrogen-bonded geometry obtained in the absence of point charges was embedded within the PDC field and a geometry optimisation performed. Similarly, the singly hydrogen-bonded structure obtained within the PDC was optimised in the absence of the PDC field. In the presence of the PDC, interaction of the methanol *via* a single hydrogen bond was more stable than the bifurcated motif by 66 kJ mol^{-1}. In the absence of PDC, the bifurcated hydrogen bonding geometry was more stable than the single hydrogen bonded system by some 47.5 kJ mol^{-1}. These values were obtained by omitting or including the PDC, as appropriate. During the course of these optimisations, the singly hydrogen-bonded system was regenerated within the point charges, and a bifurcated motif in their absence.

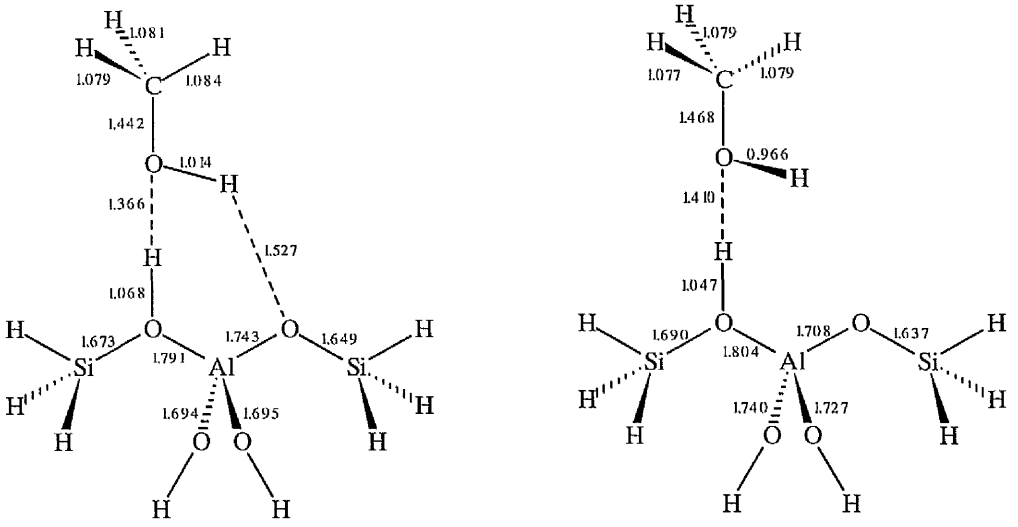

(a) 3-21G/NONE. *(b) 3-21G/3-21G.*

figure 4.12 - Optimised geometries for the zeolite Y T3 cluster-methanol interaction, with and without PDC.

Noteworthy points regarding the geometries adopted with and without the point charges are the substantial lengthening of both the hydrogen bond from the Brønsted hydrogen to the methanol oxygen and the C-O bond of the methanol within the point charge model, relative to the bare cluster model (table 4.6). Also, the shorter Al-O bond to the non-Brønsted oxygen within the point charges is consistent with the single hydrogen bonded geometry adopted by the methanol molecule, where the stronger acidic OH bond within the point charges results in a weaker Al-O bond to the Brønsted oxygen, and a consequent strengthening of the other Al-O bond. Without the PDC, this effect is enhanced by the hydrogen bond to the non-Brønsted oxygen which also plays a role in the weakening of the Al-O bond. In the absence of the PDC, the lengthening of the methanol hydroxyl group associated with the formation of the second hydrogen bond is quite marked, with a sufficient change from the PDC system that their vibrational

properties are likely to be substantially different, using the characteristic O-H stretch as an indicator of the degree of proton transfer. To determine the effect of incorporating larger basis sets, we now report geometry optimisations of the methanol-zeolite system at the 6-31G** level.

At the larger 6-31G** basis set, the orientation of the substrate relative to the cluster differs substantially from that determined at the 3-21G level, whether or not PDC are present. The optimised geometries are shown as figure 4.13 (co-ordinates in appendix B(13) and B(14)). Within the PDC field, methanol interacts with the zeolite framework through a single hydrogen bond, as shown previously for the interaction of water. In the absence of the PDC field, a bifurcated motif was found to be the lowest stationary point. In the presence of the PDC, interaction through a single hydrogen bond was found to be ~68 kJ mol^{-1} more favourable than the doubly hydrogen bonded motif. In the absence of the PDC field, interaction *via* two hydrogen bonds was more favourable by ~36.6 kJ mol^{-1} than the singly hydrogen bonded situation.

Clearly, at the 6-31G** basis set the oxygen of the methanol is reasonably remote from the Brønsted hydrogen, and at some distance, the second hydrogen bond to the framework will weaken to the point where it can 'unclip', but the role played by the electrostatic potential in the orientation of the methanol is presently unclear, though the methanol appears distant enough from the walls of the zeolite that any undue repulsive interaction is substantially involved.

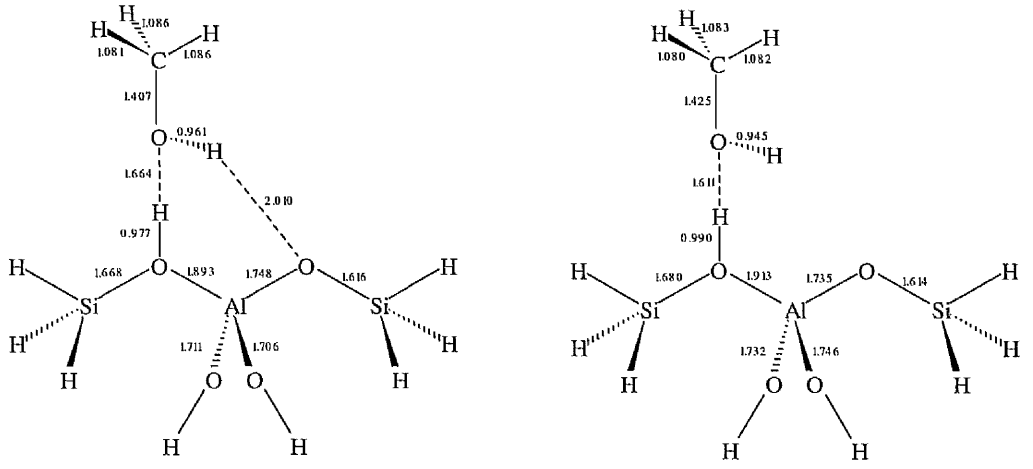

*(a) 6-31G**/NONE.* *(b) 6-31G**/3-21G.*

*figure 4.13 - 6-31G** optimised geometries for the zeolite Y T3 cluster-methanol interaction, with and without PDC.*

Whilst there are clear differences with previous work[28] with regard to the hydrogen bonding geometry adopted by the methanol molecule within the PDC field, it is worth drawing attention to similarities which exist. The failure to locate stationary points for adsorbed methoxonium cation, either with or without PDC is in agreement with a density functional study by Gale[28]. Whilst previous studies by Sauer[29] and Bates[30] indicated the formation of distinct physisorbed and chemisorbed stationary points for methanol, these findings have been shown to depend on the imposition of symmetry constraints[28]. In the absence of PDC, the geometry adopted by the methanol molecule is very similar to that obtained by Bates[30], with a 6-31G* basis set and C_s symmetry constraints.

Using the 3-21G optimised geometries described above, vibrational properties of the sorbed methanol were calculated, both with and without the point charges, using the finite-differences method described previously. Comparison between the calculated frequencies for the methanol (table 4.11) with and without the PDC and previous high-level calculations at the DFT level of theory[28] is particularly informative (we assume that the A-B-C triplet, observed at similar frequencies to those in water, are attributed to similar resonant interactions).

	3-21G/NONE	3-21G/3-21G
C-H stretch	3303	3337
C-H stretch	3264	3321
C-H stretch	3208	3239
C-O stretch	1113	1049
O-H stretch (methanol)	3056	3912

table 4.11 - Unscaled harmonic vibrational frequencies, in cm^{-1}, for the interaction of methanol with the Si-H terminated T3 cluster, with and without PDC at 3-21G.

These values can be used to additionally investigate the plausibility of the substantially different binding geometries obtained with and without the PDC by comparison with experimental spectra. A particular noteworthy feature from the study by Mirth[2] is the presence in the experimental spectrum of a frequency in the region ~3660 cm^{-1}. At the low coverages considered, this peak is attributed to the O-H stretch of a methanol molecule (the more acidic OH groups of the zeolite are substantially weaker, lying in the region of ~3400 cm^{-1}). The stretch observed in the spectrum lies very close to

the OH stretch of free methanol, implying a lack of hydrogen bonding *via* the hydroxyl hydrogen, suggesting the possibility of a singly hydrogen-bonded interaction motif. Other features within the calculated frequencies remain the same with and without the PDC, and indeed, similar to previous calculations. Whilst there is a slight decrease in the C-O stretch of the methanol molecule within the embedded cluster model, this is in line with the slight increase in bond length observed. The three C-H frequencies, and indeed bond lengths remain essentially the same whether or not PDC are present.

Calculated binding energies at the Hartree-Fock and correlated levels, for both the 3-21G and 6-31G** geometries, relative to the neutral zeolite and methanol, are reported in table 4.12. BSSE corrections were calculated for the 6-31G** structures at the Hartree-Fock level and are also included in table 4.12. Incorporating electron correlation *via* the B-LYP density functional causes an increase in the calculated binding energy of ~47 kJ mol^{-1} over the 6-31G** result in the absence of the PDC and ~22 kJ mol^{-1} in their presence.

	3-21G	**6-31G****	**6-31G**/B-LYP**
3-21G/3-21G	-142.4	-81.1	-103.7
3-21G/NONE	-122.2	-40.3	-87.4
6-31G/3-21G**	-	-59.2 (9.9)	-75.2
6-31G/NONE**	-	-58.6 (10.8)	-80.2

*table 4.12 - Binding energies for methanol, in kJ mol^{-1}, evaluated at the 3-21G and 6-31G** optimised geometries. Column headings denote level at which single-point energy evaluation was performed. BSSE corrections in parentheses.*

At the 6-31G** optimised geometries, tighter binding is again obtained in the presence of the PDC field. The effect of correlation *via* the B-LYP functional is again to increase the calculated binding energy, with a smaller increase observed within the PDC field.

Surprisingly, even though the chemistry of methanol within zeolites is of considerable economic importance, there is still a paucity of clear thermodynamic data concerning the interaction of methanol with zeolites. For this reason, the binding energies calculated can only be judged against previous calculations. A considerable range of calculated binding energies have been reported in the literature, with the DFT study of Gale[28] determining values in the range 63.5-79 kJ mol^{-1} for various cluster sizes. At the Hartree-Fock level, a value of 55.8 kJ mol^{-1} at the 6-31G* basis set level was reported by Bates[30] with an estimate by Sauer[29] of 73 kJ mol^{-1}. Rather than speculate about the likely magnitudes of the corrected binding energies and the relative performance of the bare and embedded cluster models, it should be noted that there are surprisingly many areas in which thermodynamic data are contradictory, sketchy or simply absent. An additional difficulty arises in this case as the difference of interaction energies of only 19 kJ mol^{-1} between the bare and embedded cluster models is small enough that given the considerable range of previously calculated and speculated values, no definitive comment be made on their relative merit.

4.4.5 - Interaction of ammonia with zeolite Y T3 clusters

As has been remarked previously, there are presently few areas in the study of zeolites where a full range of unambiguous experimental data for well characterised systems exist, which can be used in the calibration of theoretical models. One of the most widely studied systems, largely because of the interest in proton transfer reactions from Brønsted sites, is the adsorption of ammonia. Fortunately, the reasonable range of experimental data which exists for ammonia adsorption, both IR and thermodynamic, allows for better comparison to be made between the embedded and bare cluster models. Experimental[6] and theoretical[6,31,32,33] consensus is that within hydrogen forms of zeolites, ammonia is protonated and exists as an ammonium ion co-ordinated to the lattice *via* hydrogen bonds.

We first report geometry optimisations performed at the 3-21G basis set level. In the absence of the PDC field at 3-21G, stationary points corresponding to both physisorbed and chemisorbed ammonia were obtained on geometry optimisation, shown in figure 4.14 (co-ordinates in appendix B(15) and B(16), respectively). Although two distinct stationary points were obtained, physisorption was found to be more favourable than chemisorption by ~10.3 kJ mol^{-1}. Geometry optimisation within the PDC field yielded only a single stationary point corresponding to the proton-transferred chemisorbed ammonium ion, shown in figure 4.15 (co-ordinates in appendix B(17)). It is worth noting that within the PDC, the physisorbed structure shows a degree of hybrid character in that the Brønsted O-H length of 1.344 Å is certainly in the range of a strong

hydrogen bond, whilst the N-H distance of 1.149 Å is somewhat long, but could still reasonably be considered to be a true bond rather than a hydrogen bond. It is worth noting that in the PDC field, the chemisorbed ammonium ion adopts a doubly hydrogen bonded binding geometry, in contrast to the triply hydrogen-bonded geometry adopted by the ammonium ion when no PDC are present.

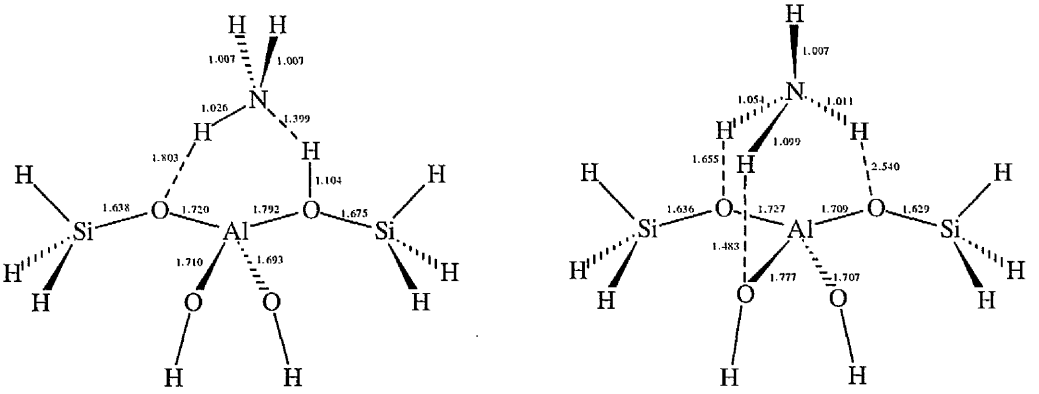

(a) Physisorption (NH_3). *(b) Chemisorption (NH_4^+).*

figure 4.14 - Optimised 3-21G geometries for physisorbed and chemisorbed ammonia without PDC.

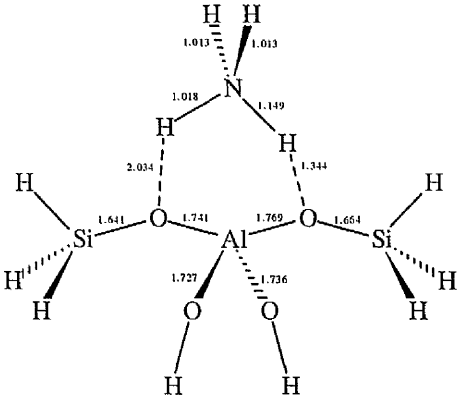

figure 4.15 - Optimised 3-21G geometry for chemisorption (NH_4^+) within PDC.

A recent DFT study of ammonia adsorption on zeolites[34] found that in bare cluster models, the favoured interaction motif involves three hydrogen bonds between the ammonium ion and the zeolite. After including the Madelung potential as a perturbation to the Kohn-Sham Hamiltonian, the doubly hydrogen-bonded interaction is found to be preferentially stabilised.

In order to investigate basis set effects and determine quantitatively better estimates of the binding energies, geometry optimisations were performed with the larger 6-31G** basis set. At the 6-31G** level, whether or not PDC were present, stationary points corresponding to both physisorbed and chemisorbed ammonia were obtained (figures 4.16 and 4.17 - co-ordinates in appendix B(18) to B(21)). In the absence of the PDC field, the bound NH_4^+ substrate adopts a 3-fold hydrogen bonding motif, shown in figure 4.16, in agreement with, previous work by Teunissen[35] and Kyrlidis[34]. In the absence of the PDC field, chemisorption of ammonia was found to be more favourable than physisorption by some 3.6 kJ mol^{-1}, showing behaviour opposite to that of the 3-21G calculations. On incorporation of electronic correlation *via* the B-LYP density functional, the chemisorbed structure was calculated to be some 16.2 kJ mol^{-1} more stable than the corresponding physisorbed system.

In the presence of the PDC field, however, the ammonium ion adopts a distinctly different interaction geometry with the zeolite framework. Geometry optimisation located stationary points for both physisorption and chemisorption in which the interaction with the zeolite was *via* a single hydrogen bond, shown in figure 4.17. This considerable difference from the 3-21G geometries can be rationalised by noting that it has been demonstrated previously for water and methanol that larger basis sets result in

the substrates docking more distantly from the cluster. Also, the inclusion of more realistic zeolite electrostatics has been shown to result in a decrease in the co-ordination of the docked substrate[34]. It is worth noting that although the H-O distance of 2.344 Å is included in figure 4.17, this cannot be regarded as a hydrogen bond in view of both the direction in which the N-H bond vector is orientated and the distance involved. Within the PDC field, chemisorption was found to be more favourable than physisorption by 12.2 kJ mol^{-1} at both the Hartree-Fock and correlated levels, in good agreement with a value of 10 kJ mol^{-1} previously calculated[34].

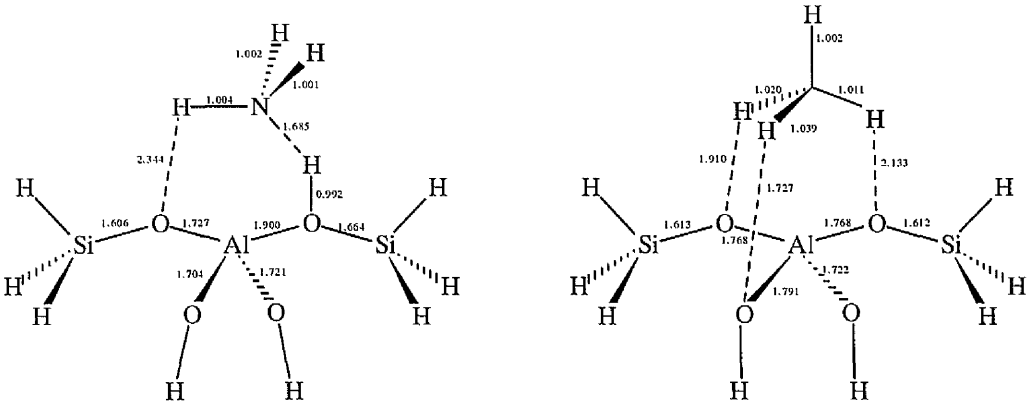

(a) Chemisorption (NH_3). *(b) Physisorption (NH_4^+).*

*figure 4.16 - Optimised geometries at 6-31G**, of adsorbed NH_3 and NH_4^+ with no PDC field.*

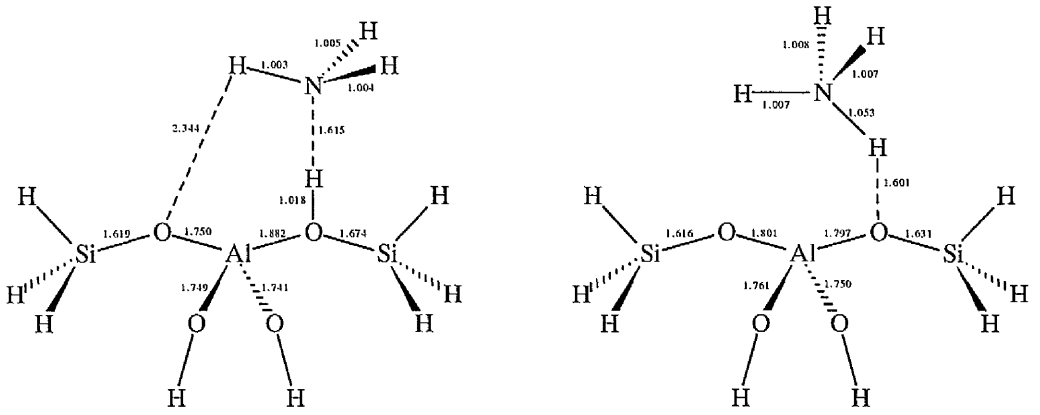

(a) Chemisorption (NH_3). *(b) Physisorption (NH_4^+).*

*figure 4.17 - Optimised geometries at 6-31G** of adsorbed NH_3 and NH_4^+ within PDC field.*

Using the 3-21G and 6-31G** optimised geometries described previously, we now report calculated binding energies for ammonia, which can be compared with adsorption enthalpies determined using either calorimetric[36,37] methods or temperature programmed desorption[38] (TPD) techniques. Here, a considerable range of values has been suggested, 100 to 150 kJ mol^{-1}.

Binding energies were determined initially at the 3-21G optimised geometries, with energy evaluations performed at the Hartree-Fock level using both the 3-21G and 6-31G** basis sets. The effect of correlation was investigated by performing binding energy calculations at the 6-31G** basis set, using the B-LYP density functional. The calculated binding energies, reported in table 4.13, are relative to the neutral zeolite and ammonia.

	3-21G	6-31G**	6-31G**/B-LYP
3-21G/NONE	-154.8	-103.0	-35.0
3-21G/3-21G	-125.3	-57.3	-149.7

table 4.13 - Binding energies for ammonia, in kJ mol^{-1}, evaluated at the 3-21G optimised geometries.

More extensive consideration has been afforded to the geometries calculated at the 6-31G** basis set, and determinations of the binding energy have been performed at both the Hartree-Fock and correlated levels, using both a density functional (B-LYP) and perturbational (MP2) approach. Binding energies, summarised in table 4.14, were calculated for the chemisorption and physisorption geometries, both with and without PDC. At the 'best' level of theory considered here, with single-point energy evaluations using the 6-31G** basis set in conjunction with the B-LYP density functional, the binding energy calculated within the PDC field is seen to be in far better agreement with experimental values (table 4.14).

	$\Delta H_{binding}$(HF)	$\Delta H_{binding}$(B-LYP)	$\Delta H_{binding}$(MP2)
6-31G/NONE**†	-68.2 (9.7)	-90.5	-92.9
6-31G/3-21G**†	-98.0 (10.2)	-125.9	-124.5
6-31G/NONE**‡	-71.8 (7.9)	-106.7	-115.5
6-31G/3-21G**‡	-110.2 (5.8)	-138.2	-144.9

*table 4.14 - Binding energies, in kJ mol^{-1}, for ammonia at 6-31G** optimised geometries. † denotes physisorption (NH_3) and ‡ denotes chemisorption (NH_4^+). BSSE corrections in parentheses.*

The use of the better 6-31G** basis set, interaction energies for which are shown in table 4.14, shows the same effects exhibited at 3-21G, of increased binding when both correlation or PDC are incorporated, with binding energies of -138.2 kJ mol^{-1} in the presence of the PDC and -106.7 kJ mol^{-1} without (this corresponds to the 'best' calculation considered, using the 6-31G** optimised geometries and the B-LYP density functional). Inclusion of electronic correlation, either through the use of standard Møller-Plesset perturbation theory or density functionals, is seen to be very important in the accurate determination of binding energies, in agreement with a recent study by Teunissen[39]. In all cases, the absence of correlation results in an underestimation of the binding energy by some 30 kJ mol^{-1}. The inclusion of the PDC field is also seen to have an influence of the same order and both corrections are required in order to obtain binding energies in agreement with experiment. CPC estimates of the basis set superposition error have been determined at the Hartree-Fock 6-31G** level and are included in table 4.14. The small CPC contributions (in the range 5.8 to 10.2 kJ mol^{-1}) can be attributed to the quality of the basis set used and are far smaller than those determined recently with a mixed basis set[39]. After incorporation of the CPC, which results in a reduction in the binding energies, it can be seen that the absence of PDC results in binding energies which fall outside the experimentally accepted range, whilst the binding energies within the PDC are in better agreement with experiment. Zero-point terms, which should also be considered in a full determination of the binding energies, however cannot be easily calculated as a result of the constrained optimisation scheme adopted, but it is expected that both bare and embedded cluster models will be affected to a similar degree.

4.4.6 - Thermochemistry of ammonia binding in zeolite Y

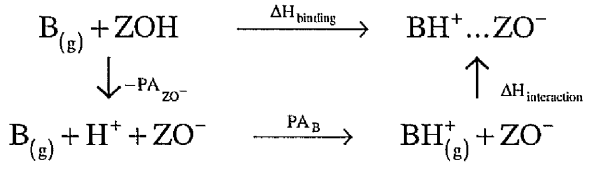

figure 4.18 - Thermodynamic cycle for base adsorption on zeolite acidic sites - from Parrillo[36].

Whilst there is still a paucity of solid thermochemical data which can be used to assess the quality of quantum chemical treatments of zeolites, Parrillo[37] recently noted an extremely useful result that for the zeolite H-ZSM-5 and a series of simple amines, the sum of the zeolitic proton affinity and the zeolite-substrate ion pair interaction energy was a constant +712±10 kJ mol^{-1}, giving a linear relationship with slope unity, between the heat of adsorption ($\Delta H_{binding}$) and the proton affinity of the base. Indeed, they suggest the likely use of this value in the calibration of theoretical treatments.

Whilst their method of determining this value requires the summation of the two vertical 'legs' of the thermodynamic cycle shown in figure 4.18, closer inspection reveals that since

$$\Delta H_{binding} = -PA_{zo^-} + PA_B + \Delta H_{interaction} \qquad (4.6)$$

The intercept of their plot, E_I, is given by

$$E_I = -PA_{zo^-} + \Delta H_{interaction} \qquad (4.7)$$

Clearly, this value can then be expressed as

$$E_I = E_{BH^+ZO^-} - E_{ZOH} - E_{BH^+(g)} \qquad (4.8)$$

This result is particularly surprising because neither the proton affinity of the base nor the zeolite plays a part. Another useful feature of this value is that the proton affinity within the embedded cluster model is not involved and useful comparisons can be made between the embedded and bare cluster models. The magnitude of E_I has been calculated, using the relation shown in equation 4.8, at both the 3-21G and 6-31G** optimised geometries described earlier and reported in table 4.15.

	Physisorption (NH_3)	**Chemisorption (NH_4^+)**
3-21G/3-21G/NONE	824	835
3-21G/3-21G/3-21G	-	795
6-31G/6-31G**/NONE**	851	847
6-31G/6-31G**(MP2)/NONE**	827	804
6-31G/6-31G**(B-LYP)/NONE**	820	805
6-31G/6-31G**/3-21G**	821	809
6-31G/6-31G**(MP2)/3-21G**	796	775
6-31G/6-31G**(B-LYP)/3-21G**	786	773

*table 4.15 - Determinations of E_I in kJ mol^{-1} at both 3-21G and 6-31G** optimised geometries.*

Clearly, the effect of the PDC field is to produce values which are closer to the experimental intercept (712±10 kJ mol^{-1}) determined by Parrillo[37]. As a result of substantial differences in the geometries adopted by the adsorbed substrates at the 3-21G and 6-31G** levels, a more in-depth study of E_I has been performed at the larger basis set. Clearly, the incorporation of PDC results in a better determination of E_I than the bare cluster models. Whilst the value is substantially over-estimated in all cases, it is worth noting that basis set superposition effects and the neglect of zero-point terms may considerably affect the computed values, particularly at the smaller 3-21G basis set.

The effect of incorporating correlation is to reduce the calculated value of E_I in all cases. The incorporation of the PDC field also reduces the calculated E_I by a similar amount, as expected from the changes in the binding energies.

4.5 - Si-OH terminated T2 clusters

4.5.1 - Cluster selection and fitting details

We now investigate the possible use of small T2 clusters to study zeolite-substrate interactions within the embedded cluster model developed within this thesis. The use of T2 clusters has the advantage that it facilitates the use of higher basis sets and the inclusion of correlation corrections, either by perturbative methods or the use of density functionals, necessary for quantitative modelling, at moderate computational cost. The interaction of ammonia with the O1 site of zeolite Y is considered at both the 3-21G and 6-31G** basis sets. The Si-OH terminated T2 cluster and its relationship to the zeolite Y primitive cell is shown in figure 4.19 (co-ordinates in appendix B(22)).

The determination of the point charge values used in the T2 cluster calculations was based on the 3-21G periodic wavefunction described previously. The sampling grid (co-ordinates in appendix B(23)), was selected using the criteria detailed in chapter 3. The fitting grid was a 15 bohr sphere of crystal sites centred on the central bridging oxygen of the cluster, chosen because it gave a small standard deviation in the potential

and a reasonable magnitude of the resultant charges. The total charge of the system was constrained to zero, with no net dipole constraint.

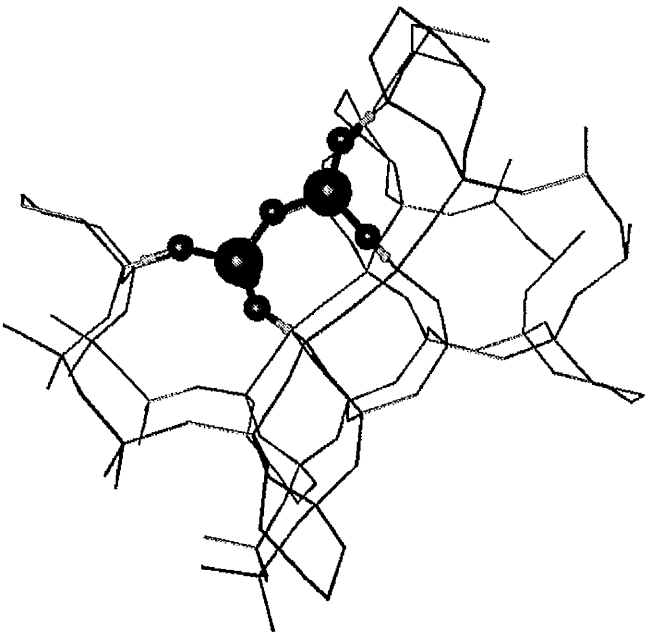

figure 4.19 - Si-OH terminated T2 cluster in relation to the zeolite Y primitive cell.

A constrained geometry optimisation scheme was adopted in which the position of the central oxygen (and attached proton in the case of the acidic clusters) was allowed to optimise within the constrained terminating hydrogens and T sites. The resulting geometries are given in table 4.16 and 4.17.

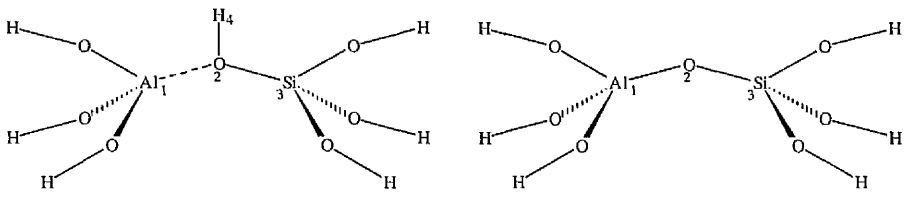

(a) Acidic cluster. *(b) Anionic cluster.*

figure 4.20 - Si-H terminated T2 clusters.

	Al_1-O_2	O_2-Si_3	O_2-H_4	Al_1-O_2-Si_3	Al_1-O_2-H_4	Si_3-O_2-H_4
3-21G/NONE	1.839	1.690	0.969	128.4	112.1	119.4
3-21G/3-21G	1.839	1.690	0.969	128.4	112.1	119.4
6-31G/NONE**	1.891	1.683	0.948	127.9	115.2	116.7
6-31G/3-21G**	1.890	1.683	0.948	128.0	115.2	116.7

table 4.16 - Selected optimised bond lengths for Si-OH terminated acidic T2 clusters. Atom numbering corresponds to figure 4.20 (a).

	Al_1-O_2	O_2-Si_3	Al_1-O_2-Si_3
3-21G/NONE	1.701	1.579	132.2
3-21G/3-21G	1.701	1.578	132.2
6-31G/NONE**	1.734	1.562	127.9
6-31G/3-21G**	1.734	1.562	127.9

table 4.17 - Selected optimised parameters for Si-OH terminated anionic T2 clusters. Atom numbering corresponds to figure 4.20 (b).

The lack of any significant differences in the geometries with and without the PDC arrays is in marked contrast to those obtained with larger T3 clusters. Although the effects associated with the use of a polarised basis set, the lengthening of the Al-O bond and a shortening of the acidic O-H bond, were observed upon increasing the basis set from 3-21G to 6-31G**, no changes in geometry were observed upon the addition of PDC. In view of the substantial changes observed within both Si-H and Si-OH terminated T3 cluster models, it appears that the T2 model is an unrealistic model for zeolite structure as the constraints, necessary in maintaining the orientation of the cluster with respect to the point charges, have the side effect of removing the flexibility within

the model, vital to the accurate description of zeolite properties. Whilst the use of T2 clusters appears inappropriate for the study of zeolite Brønsted site geometry, it may be the case that they can still play a useful role in the study of zeolite-substrate interactions. This possibility is now investigated.

4.5.2 - Interaction of ammonia with zeolite Y T2 clusters

The interaction of ammonia with the T2 clusters was considered by optimising the structure of the anionic zeolite-ammonium ion complex. The ammonium ion atoms were given complete freedom to optimise, with the cluster subject to the constraints described previously. The resulting geometries are given in table 4.18, co-ordinates of which are included as appendix B (24) to B(27) respectively.

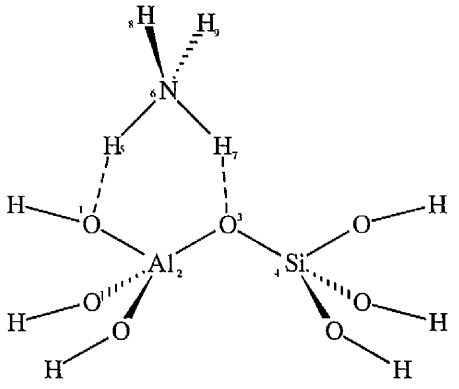

figure 4.21 - Ammonium ion bound to zeolite-Y T2 cluster.

	3-21G/NONE	3-21G/3-21G	6-31G**/NONE	6-31G**/3-21G
O_1-H_5	1.412	1.521	1.484	1.670
H_5-N_6	1.132	1.087	1.095	1.048
N_6-H_7	1.074	1.055	1.027	1.021
H_7-O_3	1.531	1.622	1.784	1.871
Al_2-O_3	1.739	1.731	1.754	1.752
O_3-Si_4	1.624	1.613	1.604	1.592
N_6-H_8	1.008	1.011	1.003	1.005
N_6-H_9	1.009	1.011	1.003	1.005

table 4.18 - Optimised distances for the ammonium ion-anionic zeolite Y T2 cluster system (figure 4.21).

There are substantial differences in the calculated geometries using the T2 cluster when compared with the larger Si-H terminated T3 cluster. For the smaller cluster, the ammonium ion docks in a bifurcated interaction motif in all cases. The triply hydrogen-bonded interaction geometries determined for ammonium in the absence of the PDC for the larger cluster are absent in this case. Also, the tendency for the ammonium ion to interact with the zeolite cluster through one hydrogen bond, as observed within the PDC for the larger cluster is not observed for the smaller T2 cluster. The tendency for the substrate to be sited further away from the cluster at the larger basis set is, however demonstrated within the Si-OH terminated T2 cluster, though to a far smaller degree than shown for the larger cluster. These substantial differences in the optimised geometries suggest that the constraints on the T2 cluster unrealistically and unacceptably repress the flexibility of the zeolite.

As described previously, the interaction of ammonia with zeolites is one of the few areas in the study of zeolite catalysis in which there is a full range of both

thermodynamic and spectroscopic data. Microcalorimetry and thermally programmed desorption (TPD) studies have both been used in the determination of binding energies for ammonia within zeolites, giving a range of values of -120 to -145 kJ mol^{-1}, on zeolite $Y^{40,}$ and -100 to -150 kJ mol^{-1} on H-ZSM-5. The relative performance of the bare and embedded cluster models may be gauged from how well binding energies compare with those determined experimentally.

	$\Delta H_{binding}$
3-21G/NONE	-160.5
3-21G/3-21G	-170.9
6-31G/NONE**	-74.3
6-31G/3-21G**	-109.5

*table 4.19 - Binding energies, in kJ mol^{-1}, for optimised 3-21G and 6-31G** T2 clusters with ammonia.*

We first note that there are factors which may have a substantial influence on the calculated binding energies, reported in table 4.19, which are not included here, particularly the basis set superposition error which will result in a reduction of the binding energies (particularly at the 3-21G basis set), and zero point effects, difficult to calculate within the constrained optimisation scheme adopted. Correlation corrections have also not been considered for this small cluster. At the 3-21G basis set, the calculated binding energy in the absence of the PDC field is within 5 kJ mol^{-1} of that determined with an Si-H terminated T3 cluster (table 4.13). In the presence of the PDC field, however there is a substantial difference in the binding energies, with ammonia

bound some 45 kJ mol^{-1} more tightly than in the larger cluster. The binding energies calculated at the Hartree-Fock 6-31G** basis set level (table 4.19) are in better agreement, lying within 3 kJ mol^{-1} of the larger cluster results (table 4.14) in the absence of the PDC and 1 kJ mol^{-1} in their presence. Thus calculations for the T2 cluster at the 6-31G** basis set may be valuable for predicting binding energies, the corresponding geometries should be viewed with caution.

4.6 - Conclusions

The use of point charge fields, designed to include accurate representation of the electrostatic effects of the periodic zeolite within traditional small cluster models, has been investigated using a range of cluster types, for a number of properties. Where possible, these values have been compared to experimental and previous theoretical results. The use of a relatively small 3-21G(*)* basis set for the optimisation of the local geometries of each of the four crystallographically distinct T sites in zeolite Y, using an Si-OH terminated T3 cluster, provided excellent agreement with experimental IR data, reproducing well the shift between the high and low frequency OH stretching bands The need to correct the deprotonation energies of the different sites by including the classical electrostatic solvation of the proton was also highlighted.

The use of Si-H terminated T3 clusters in the study of zeolite-substrate interactions appears to provide an acceptable compromise between the Si-OH terminated

T3 clusters, prohibitively expensive for interaction studies, and the smaller Si-OH T2 clusters in which the quality of representation in the terminal regions may be inadequate.

Particularly interesting conclusions relating to the use of PDC embedding using T3 Si-H terminated models are the substantially different hydrogen bonding motifs, relative to the bare cluster model, of all substrates studied. In the case of each of the three substrates considered, longer hydrogen bonds were obtained within the PDC fields, with the substrates preferentially sited further from the acidic site. This is perhaps not surprising when viewed in the context of the earlier cancrinite calculations, where a much shallower potential in the zeolite cavity was obtained after embedding. Additionally, the bonds within the substrates directed toward the zeolite were shorter in all cases. The transfer of the Brønsted proton to the substrate was found only to occur for the most basic compound, ammonia.

The optimised geometry for the methanol molecule was surprising in that the bifurcated hydrogen bonding motif previously predicted was not obtained. This finding is, however, consistent with the vibrational spectrum of methanol adsorbed on zeolite Y which shows the presence of an essentially free methanol hydroxyl stretch, suggesting the possibility of only a single hydrogen bond to the framework.

Ammonia provides the greatest range of experimental thermodynamic data, and a more extensive theoretical study was performed. The heats of adsorption of ammonia on zeolite Y have been variously determined to lie in the range 100-150 kJ mol^{-1}. The very large range spanned here is of little use in determining the relative performance of the

embedded and bare cluster models, but the trend is towards the embedded cluster model performing better in all cases.

We find that a particularly useful test is the calculation of the property E_I, which allows for direct comparison with an experimental observable for which a direct knowledge of the deprotonation energy of the lattice is not required, and also allows for direct comparison between bare and embedded cluster models.

Determinations of the cluster geometry obtained using a constrained energy minimisation scheme with small Si-OH terminated T2 clusters showed the difficulty in striking a balance between including a realistic degree of cluster relaxation in the calculations and using clusters small enough to allow the use of large basis sets and high levels of theory. Clearly, the use of constrained optimisation schemes with clusters this small may lead to unrealistic and unacceptable constraints on the relaxational ability of the zeolite. The possibility of obtaining useful binding energy data from the interaction of T2 clusters with substrates was demonstrated.

4.7 - References

[1] Batamack, P.; Dorémieux-Morin, C.; Vincent, R.; Fraissard, J., *Chem. Phys. Lett.*, **1991**, 180, 545

[2] Mirth, G.; Kogelbauer, A.; Lercher, J. A., in *"Proceedings of the 7th International Conference on Zeolites, Montreal"* Butterworths, London, **1993**, 251

[3] Jacobs, W. P. J. H.; de Haan, V. O.; van Santen, R. A.; de Graaf, L. A., *J. Phys. Chem.*, **1994**, 98, 2180

[4] van Hooff, J. H. C.; Roelofsen, J. W., in *"An Introduction to Zeolite Science and Practice"* Elsevier, **1991**, 242

[5] Jentys, A.; Warecka, G.; Derewinski, M.; Lercher, J. A., *J. Phys. Chem.*, **1989**, 93, 4837

[6] Jacobs, W. P. J. H.; de Haan, J. W.; van de Ven, L. J. M.; van Santen, R. A., *J. Phys. Chem.*, **1993**, 97, 10394

[7] Batamack, P.; Dorémieux-Morin, C.; Fraissard, J.; Freude, D., *J. Phys. Chem.*, **1991**, 95, 3790

[8] Parker, L. M.; Bibby, D. M.; Burns, G. R., *Zeolites*, **1991**, 11, 293

[9] Pelmenschikov, A. G.; van Santen, R. A., *J. Phys. Chem.*, **1993**, 97, 10678

[10] Gallezot, P.; Beaumont, R.; Barthomeuf, D., *J. Phys. Chem.*, **1974**, 78, 1550

[11] This work benefited from the use of the Chemical Database Service at the Daresbury Laboratory.

[12] Szostak, R., in *"An Introduction to Zeolite Science and Practice"* Elsevier, **1991**, 153

[13] Sauer, J., *J. Phys. Chem.*, **1987**, 91, 2315

[14] Mortier, W. J.; Sauer, J.; Lercher, J. A.; Noller, H., *J. Phys. Chem.*, **1984**, 88, 905

[15] Campana, L.; Selloni, A.; Weber, J.; Pasquarello, A.; Papai, I.; Goursot, A., *Chem. Phys. Lett.*, **1994**, 226, 245

[16] Nicholas, J. B.; Hess, A. C., *J. Am. Chem. Soc.*, **1994**, 116, 5429

[17] O'Malley, P. J.; Dwyer, J., *J. Phys. Chem.*, **1988**, 92, 3005

[18] Jacobs, W. P. J. H.; van Wolput, J. H. M. C.; van Santen, R. A., *J. Chem. Soc. Faraday Trans.*, **1993**, 89, 1271

[19] Gil, B.; Broclawik, E.; Datka, J.; Klinowski, J., *J. Phys. Chem.*, **1994**, 98, 930

[20] Barthomeuf, D., in *"Catalysis by zeolites"* Elsevier, **1980**, 55

[21] Brand, H. V.; Curtiss, L. A.; Iton, L. E., *J. Phys. Chem.*, **1993**, 97, 12773

[22] Makarova, M. A.; Al-Ghefaili, K. M.; Dwyer, J., *J. Chem. Soc. Faraday Trans.*, **1994**, 90, 383

[23] Redondo, A.; P. J. Hay., *J. Phys. Chem.*, **1993**, 97, 11754

[24] Datka, J.; Boczar, M.; Rymarowicz, P., *J. Catal.*, **1988**, 114, 368

[25] Sauer, J.; Horn, H.; Häser, M.; Ahlrichs, R., *Chem. Phys. Lett.*, **1990**, 173, 26

[26] Ison, A.; Gorte, R. J., *J. Catal.*, **1984**, 89, 150

[27] Boys, S. F.; Bernardi, F., *Mol. Phys.*, **1970**, 19, 553

[28] Gale, J. D.; Catlow, C. R. A.; Carruthers, J. R., *Chem. Phys. Lett.*, **1993**, 216, 155

[29] Sauer, J.; Kölmel, C.; Haase, F.; Ahlrichs, R., in *"Proceedings of the 7th International Conference on Zeolites, Montreal"* Butterworths, London, **1993**, 679

[30] Bates, S.; Dwyer, J., *J. Mol. Struct. (THEOCHEM)*, **1994**, 306, 57

[31] Kassab, E.; Seiti, K.; Allavena, M., *J. Phys. Chem.*, **1991**, 95, 9425

[32] Teunissen, E. H.; Jansen, A. P. J.; van Santen, R. A.; Orlando, R.; Dovesi, R., *J. Chem. Phys.*, **1994**, 101, 5865

[33] Allavena, M.; Kassab, E.; Evleth, E., *J. Mol. Struct.*, **1994**, 325, 85

[34] Kyrlidis, A.; Cook, S. J.; Chakraborty, A. K.; Bell, A. T.; Theodorou, D. N., *J. Phys. Chem.*, **1995**, 99, 1505

[35] Teunissen, E. H.; van Duijneveldt, F. B.; van Santen, R. A., *J. Phys. Chem.*, **1992**, 96, 366

[36] Parrillo, D. J.; Gorte, R. J., *J. Phys. Chem.*, **1993**, 97, 8786

[37] Parrillo, D. J.; Gorte, R. J.; Farneth, W. E., *J. Am. Chem. Soc.*, **1993**, 115, 12441

[38] Tsutsumi, K.; Mitani, Y.; Takahashi, H., *Bull. Chem. Soc. Jpn.*, **1983**, 56, 1912

[39] Teunissen, E. H.; Jansen, A. P. J.; van Santen, R, A., *J. Phys. Chem.*, **1995**, 99, 1873

[40] Auroux, A.; Vedrine, J. C., *Stud. Surf. Sci. Catal.*, **1985**, 20, 311

Appendix A

(1) Input deck used for CRYSTAL calculation on cancrinite.

```
Cancrinite at STO-3G
3 0 0
5 5 5 6 12
0 0 0
173
12.670  5.190
6
14 0.07330 0.40970 0.75000
14 0.33320 0.41390 0.75200
8 0.21700 0.40300 0.64400
8 0.12310 0.56460 0.68900
8 0.03400 0.31640 0.01400
8 0.32790 0.34420 0.02800
14 3
1 0 3 2.0 0.0
1 1 3 8.0 0.0
1 1 3 4.0 0.0
8 2
1 0 3 2.0 0.0
1 1 3 6.0 0.0
99 0
30 0
7 7 0 0
4 4 4
```

(2) Stereoview of primitive unit cell of cancrinite system.

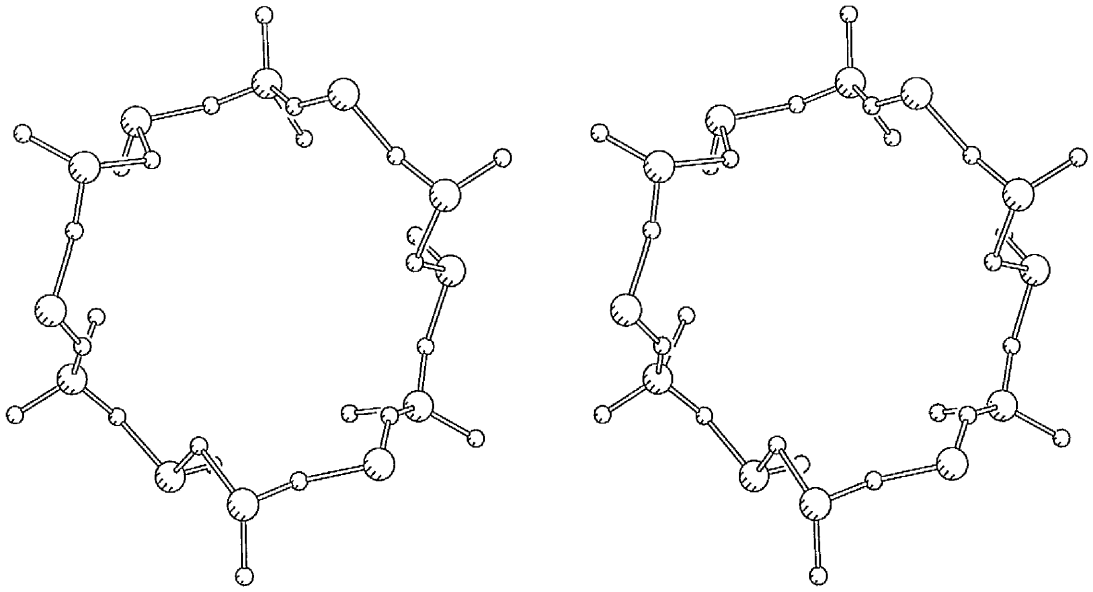

(3) Co-ordinates, in bohr, and stereoview of cancrinite Si-H terminated T3 cluster.

Si	-1.519883	-8.931876	2.451921
Si	-8.495173	-3.149681	-2.451921
Si	-6.908938	-5.921064	2.471536
O	-4.499518	-7.051166	1.412306
O	-9.028066	-8.159719	1.853652
H	-0.814989	-7.406512	4.691650
O	-6.560588	-2.973701	0.137308
H	-6.910100	-4.239349	-4.486661
O	-6.799042	-4.315697	5.178456
H	0.216333	-8.103997	0.417180
H	-7.874627	-3.576280	6.559173
H	-10.858733	-8.537050	2.194647
H	-8.389288	-0.466224	-3.244287
H	-2.387228	-11.546295	1.949402
H	-11.192999	-3.705747	-2.954439

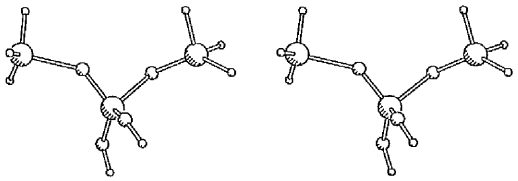

(4) Co-ordinates, in bohr, and stereoview of cancrinite Si-OH terminated T3 cluster.

Si	-1.519883	-8.931876	2.451921
Si	-8.495173	-3.149681	-2.451921
Si	-6.908938	-5.921064	2.471536
O	-4.499518	-7.051166	1.412306
O	-8.356248	0.371114	-3.491535
O	-2.552492	-12.044445	1.853652
O	-11.707042	-3.811700	-3.050189
O	-9.028066	-8.159719	1.853652
O	-0.704994	-7.168486	5.041149
O	-6.560588	-2.973701	0.137308
O	-6.799042	-4.315697	-4.629226
O	-6.799042	-4.315697	5.178456
O	0.337982	-8.045991	0.274615
H	-7.874627	-3.576280	6.559173
H	-10.858733	-8.537050	2.194647
H	-12.987729	-5.164623	-2.676773
H	-6.865348	-5.284297	-6.262449
H	-8.506169	2.130048	-2.788915
H	1.143661	-8.587714	-1.358608
H	0.491775	-8.061848	6.215733
H	-2.021170	-13.830014	2.227068

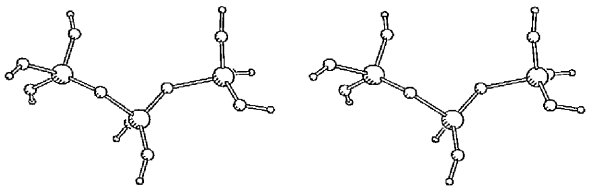

(5) Sampling grid corners, in bohr, for both the Si-OH and Si-H terminated cancrinite T3 clusters.

-1.792544	7.660465	-9.512825
11.499779	-3.652994	0.250362
-13.217175	8.389874	6.886740
0.075149	-2.923584	16.649927
-11.425402	-8.815990	-15.490653
1.866921	-20.129450	-5.727466
-22.850033	-8.086581	0.908912
-9.557709	-19.400040	10.672099

(6) Periodic geometries used in interaction energy studies.

The geometries for the three periodic systems, involving an acidic Brønsted site, water docked close to the acidic site and a hydroxonium ion docked close to the relaxed anionic zeolite can be generated as follows;
Generate a periodic supercell from the cancrinite input deck above by using the advanced geometric manipulation facilities within CRYSTAL 92, specifying the SUPERCELL keyword with the following expansion matrix

$$\begin{pmatrix} 1 & 0 & 0 \\ 0 & 1 & 0 \\ 0 & 0 & 2 \end{pmatrix}$$

From the resulting 72 atom primitive cell, the atoms below marked 'Delete' are removed from the supercell using the ATOMREMO keyword, with the atoms marked 'Add' included via the ATOMINSE command. The initial drop in symmetry which occurs upon formation of the periodic supercell and the further reduction which occurs on the addition of the relaxed Brønsted site and substrate are handled automatically by the code.

(a) Cluster system.

Delete				**Add**			
Si	-3.6561	-3.1333	1.3079	Al	-7.183695	-6.230472	2.766181
O	-2.3810	-3.7313	0.7474	O	-7.072396	-3.345124	0.339098
O	-3.4717	-1.5736	0.0727	O	-4.340363	-7.644905	2.150727
				H	-5.572149	-2.359404	0.525160

(b) H_2O.....H system.

Delete				Add			
Si	-3.6561	-3.1333	1.3079	Al	-7.183135	-6.141890	2.674564
O	-2.3810	-3.7313	0.7474	O	-7.002636	-3.453225	0.241487
O	-3.4717	-1.5736	0.0727	O	-4.307623	-7.623360	2.104485
				O	-2.031421	-2.406598	0.141522
				H	-5.091245	-2.942931	0.202442
				H	-2.078362	-3.990113	0.959584
				H	-0.341099	-1.855346	-0.051476

(c) H_3O^+ system.

Delete				Add			
Si	-3.6561	-3.1333	1.3079	Al	-7.190558	-6.028335	2.548823
O	-2.3810	-3.7313	0.7474	O	-4.233762	-7.520684	2.013740
O	-3.4717	-1.5736	0.0727	O	-6.992298	-3.484053	0.162077
				O	-2.628521	-3.610082	0.819870
				H	-4.301565	-3.372795	-0.140894
				H	-2.561274	-4.935665	2.056605
				H	-1.557842	-2.204918	1.122552

Appendix B

All co-ordinates in this appendix are reported in bohr.

(1) Co-ordinates and stereoview of zeolite Y Si-OH terminated T3 C_{14} cluster.

H	4.937286	-2.188316	2.373765
Si	5.790150	-2.503470	9.967262
H	-1.575571	1.002024	6.153700
H	1.575571	-6.153700	-1.002024
H	8.196142	-5.510598	12.685084
H	-4.937286	-2.373765	2.188316
H	-4.880371	-9.319443	2.827379
Si	-1.687628	-5.864741	2.503470
Si	1.687628	-2.503470	5.864741
H	5.501191	1.002024	13.230462
H	9.281126	-2.188316	6.717605
O	6.699231	-4.955659	11.654890
O	0.000000	-4.955659	4.955659
O	-0.093239	-0.093239	6.615316
O	5.039575	-0.093239	11.748130
O	0.093239	-6.615316	0.093239
O	8.191057	-1.687628	8.191057
O	3.463834	-1.687628	3.463834
O	-3.463834	-3.463834	1.687628
O	3.393904	-3.356608	8.260986
O	-3.393904	-8.260986	3.356608

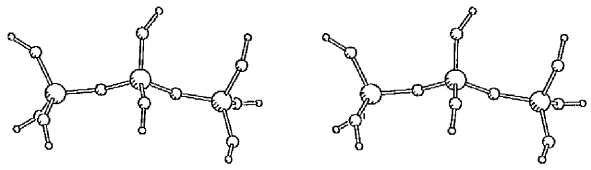

(2) Co-ordinates and stereoview of zeolite Y Si-OH terminated T3 C_{23} cluster.

Si	5.864741	-2.503470	1.687628
H	4.880371	-2.827379	9.319443
Si	-2.503470	1.687628	5.864741
H	3.458748	-5.510598	-1.030194
H	-5.510598	-1.030194	3.458748
H	-1.030194	-5.510598	3.458748
H	-2.188316	4.937286	2.373765
H	-2.827379	4.880371	9.319443
H	6.153700	1.002024	-1.575571
Si	1.687628	-2.503470	5.864741
H	9.319443	-2.827379	4.880371
O	4.955659	-4.955659	0.000000
O	-4.955659	0.000000	4.955659
O	0.000000	-4.955659	4.955659
O	-0.093239	-0.093239	6.615316
O	6.615316	-0.093239	-0.093239
O	3.463834	-1.687628	3.463834
O	-1.687628	3.463834	3.463834
O	-3.356608	3.393904	8.260986
O	3.393904	-3.356608	8.260986
O	8.260986	-3.356608	3.393904

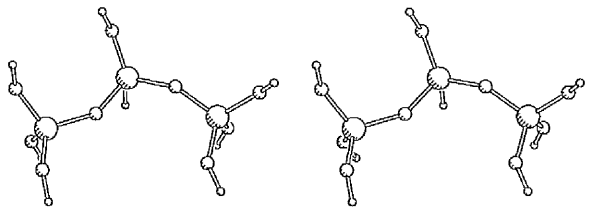

(3) Co-ordinates of sampling grid corners for C_{14} cluster.

-7.337180	-12.692523	-3.182767
10.495542	-12.818710	-3.143151
-7.211404	5.035169	-3.331903
10.621318	4.908981	-3.292287
-7.375959	-12.541352	14.754210
10.456762	-12.667540	14.793826
-7.250183	5.186339	14.605074
10.582539	5.060152	14.644691

(4) Co-ordinates of sampling grid corners for C_{23} cluster.

-7.245517	-9.491040	-4.721482
10.587693	-9.491041	-4.721482
-7.245518	8.237727	-4.721482
10.587692	8.237726	-4.721482
-7.245516	-9.491040	13.216177
10.587694	-9.491041	13.216177
-7.245517	8.237727	13.216177
10.587693	8.237726	13.216177

(5) Co-ordinates and stereoview of Si-H terminated zeolite Y T3 cluster.

Si	-1.519883	-8.931876	2.451921
Si	-8.495173	-3.149681	-2.451921
H	-7.874627	-3.576280	6.559173
H	-10.858733	-8.537050	2.194647
Si	-6.908938	-5.921064	2.471536
O	-4.499518	-7.051166	1.412306
H	-8.389288	-0.466224	-3.244287
H	-2.387228	-11.546295	1.949402
H	-11.192999	-3.705747	-2.954439
O	-9.028066	-8.159719	1.853652
H	-0.814989	-7.406512	4.691650
O	-6.560588	-2.973701	0.137308
H	-6.910100	-4.239349	-4.486661
O	-6.799042	-4.315697	5.178456
H	0.216333	-8.103997	0.417180

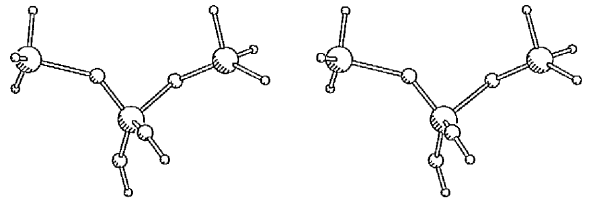

(6) Co-ordinates of sampling grid corners for Si-H terminated zeolite Y T3 cluster.

-9.236726	-13.265722	-2.676687
5.793134	-13.265722	-2.676687
-9.236726	0.731060	-2.676687
5.793134	0.731060	-2.676687
-9.236726	-13.265722	10.803562
5.793134	-13.265722	10.803562
-9.236726	0.731060	10.803562
5.793134	0.731060	10.803562

(7) Co-ordinates and stereoview of Si-H T3 cluster + H_2O at 3-21G/NONE.

Si	-5.790149	-9.967261	2.503468
H	-6.607953	-11.485441	4.709443
H	-5.109872	-11.581334	0.318978
H	-7.961552	-8.360844	1.765613
H	-4.937285	-2.373768	2.188313
H	1.575570	-6.153702	-1.002026
Si	1.687628	-2.503472	5.864739
H	0.073557	-0.318982	6.545015
H	3.294046	-1.765617	3.693335
H	3.247461	-3.283388	8.055322
O	0.008815	-5.013178	5.086920
Al	-1.612707	-5.749296	2.316901
O	-3.728274	-3.501787	1.478751
O	0.301591	-6.905477	0.018425
O	-3.263264	-8.410277	3.596719
H	-0.158004	-7.247795	6.853256
O	-0.782051	-8.998376	7.356888
H	-2.368224	-8.991282	5.302276
H	0.559479	-10.218519	7.516471

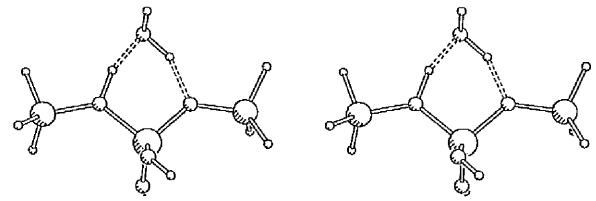

(8) Co-ordinates and stereoview of Si-H T3 cluster + H_2O at 3-21G/3-21G.

Si	-5.790149	-9.967261	2.503468
H	-6.607953	-11.485441	4.709443
H	-5.109872	-11.581334	0.318978
H	-7.961552	-8.360844	1.765613
H	-4.937285	-2.373768	2.188313
H	1.575570	-6.153702	-1.002026
Si	1.687628	-2.503472	5.864739
H	0.073557	-0.318982	6.545015
H	3.294046	-1.765617	3.693335
H	3.247461	-3.283388	8.055322
O	0.047138	-4.966509	4.898241
Al	-1.775378	-5.671564	2.254113
O	-4.651513	-4.148174	2.178579
O	-0.019183	-5.489744	-0.483199
O	-3.002848	-8.660632	3.276842
H	0.276536	-7.629022	6.678248
O	-0.251965	-9.415839	6.714498
H	-1.892668	-9.365924	4.867680
H	-0.030666	-10.353026	8.255744

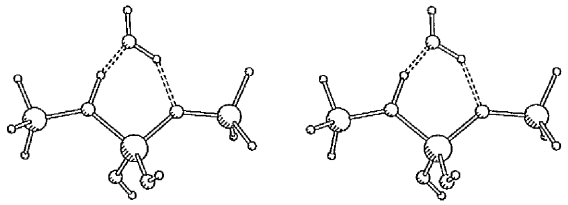

(9) Co-ordinates and stereoview of Si-H T3 cluster + H_2O at 6-31G/NONE.**

Si	-5.790148	-9.967261	2.503467
H	-6.607952	-11.485441	4.709443
H	-5.109872	-11.581333	0.318978
H	-7.961552	-8.360844	1.765612
H	-4.937284	-2.373767	2.188313
H	1.575569	-6.153702	-1.002025
Si	1.687628	-2.503471	5.864738
H	0.073556	-0.318981	6.545014
H	3.294046	-1.765617	3.693335
H	3.247460	-3.283387	8.055321
O	-0.042518	-4.871738	5.013150
Al	-1.590239	-5.475749	2.159355
O	-3.839519	-3.363285	1.199309
O	0.222531	-6.878549	-0.115178
O	-3.316311	-8.293950	3.514281
H	0.212812	-7.899180	7.195335
O	-0.398622	-9.587840	7.341360
H	-2.384269	-8.982950	4.946130
H	0.983699	-10.673036	7.030616

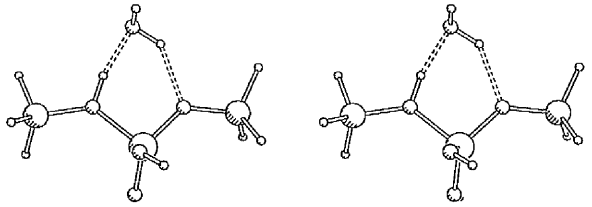

(10) Co-ordinates and stereoview of Si-H T3 cluster + H_2O at 6-31G/3-21G.**

Si	-5.790148	-9.967261	2.503467
H	-6.607952	-11.485441	4.709443
H	-5.109872	-11.581333	0.318978
H	-7.961552	-8.360844	1.765612
H	-4.937284	-2.373767	2.188313
H	1.575569	-6.153702	-1.002025
Si	1.687628	-2.503471	5.864738
H	0.073556	-0.3189815	6.545014
H	3.294046	-1.765617	3.693335
H	3.247460	-3.283387	8.055321
O	-0.048162	-4.745489	4.739773
Al	-1.734450	-5.396760	2.009889
O	-4.714927	-4.072278	1.761120
O	-0.021720	-5.413810	-0.807753
O	-3.044567	-8.546847	3.249005
H	-1.887672	-8.935702	9.287527
O	-1.932062	-10.041702	7.884402
H	-2.382025	-8.955905	4.927879
H	-1.207720	-11.591312	8.403253

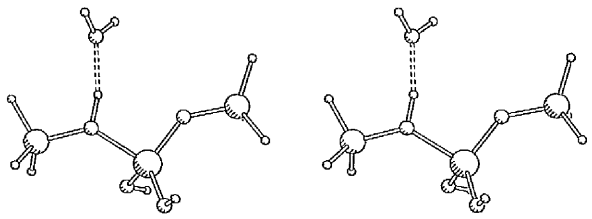

(11) Co-ordinates and stereoview of Si-H T3 cluster + CH_3OH at 3-21G/NONE.

Si	-5.790149	-9.967261	2.503468
H	-6.607953	-11.485441	4.709443
H	-5.109872	-11.581334	0.318978
H	-7.961552	-8.360844	1.765613
H	-4.937285	-2.373768	2.188313
H	1.575570	-6.153702	-1.002026
Si	1.687628	-2.503472	5.864739
H	0.073557	-0.318982	6.545015
H	3.294046	-1.765617	3.693335
H	3.247461	-3.283388	8.055322
O	-0.015881	-5.000203	5.102778
Al	-1.615685	-5.749454	2.323570
O	-3.726080	-3.496696	1.478015
O	0.274139	-6.883873	-0.000459
O	-3.296993	-8.380740	3.626748
H	-0.129221	-7.289134	6.856874
O	-0.890879	-8.950773	7.433054
H	-2.431020	-8.943028	5.361078
C	-1.674068	-9.045850	10.040583
H	-2.552692	-10.858426	10.355263
H	-3.010980	-7.557695	10.479645
H	-0.045207	-8.873722	11.261961

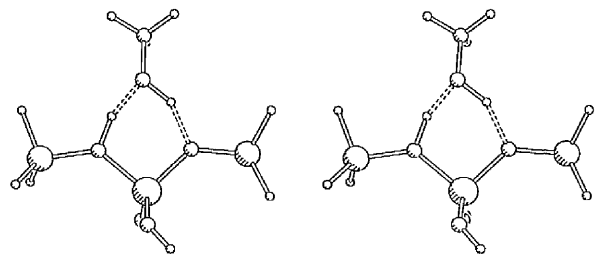

(12) Co-ordinates and stereoview of Si-H T3 cluster + CH_3OH at 3-21G/3-21G.

Si	-5.790149	-9.967261	2.503468
H	-6.607953	-11.485441	4.709443
H	-5.109872	-11.581334	0.318978
H	-7.961552	-8.360844	1.765613
H	-4.937285	-2.373768	2.188313
H	1.575570	-6.153702	-1.002026
Si	1.687628	-2.503472	5.864739
H	0.073557	-0.318982	6.545015
H	3.294046	-1.765617	3.693335
H	3.247461	-3.283388	8.055322
O	-0.015881	-5.000203	5.102778
Al	-1.615685	-5.749454	2.323570
O	-3.726080	-3.496696	1.478015
O	0.274139	-6.883873	-0.000459
O	-3.296993	-8.380740	3.626748
H	-0.129221	-7.289134	6.856874
O	-0.890879	-8.950773	7.433054
H	-2.431020	-8.943028	5.361078
C	-1.674068	-9.045850	10.040583
H	-2.552692	-10.858426	10.355263
H	-3.010980	-7.557695	10.479645
H	3.501395	-10.216559	7.526921

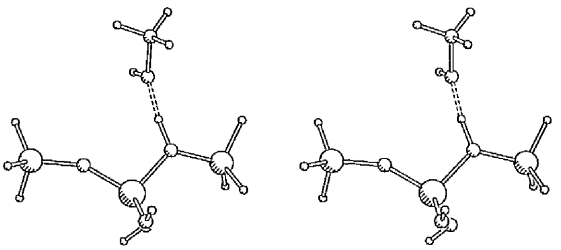

(13) Co-ordinates and stereoview of Si-H T3 cluster + CH_3OH at 6-31G/NONE.**

Si	-5.790148	-9.967261	2.503467
H	-6.607952	-11.485441	4.709443
H	-5.109872	-11.581333	0.318978
H	-7.961552	-8.360844	1.765612
H	-4.937284	-2.373767	2.188313
H	1.575569	-6.153702	-1.002025
Si	1.687628	-2.503471	5.864738
H	0.073556	-0.318981	6.545014
H	3.294046	-1.765617	3.693335
H	3.247460	-3.283387	8.055321
O	-0.055726	-4.863107	5.017284
Al	-1.592018	-5.476441	2.157404
O	-3.836497	-3.355992	1.197255
O	0.190116	-6.856952	-0.148272
O	-3.345507	-8.269359	3.541373
H	0.179770	-7.914075	7.268728
O	-0.720633	-9.435545	7.594261
H	-2.514965	-8.871958	5.075241
C	-1.592044	-9.496664	10.105894
H	-2.645171	-11.230387	10.351904
H	-2.820621	-7.905200	10.519473
H	-0.020747	-9.490301	11.422039

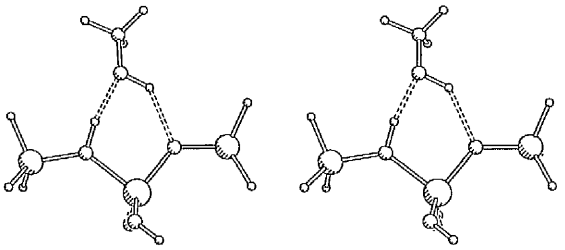

(14) Co-ordinates and stereoview of Si-H T3 cluster + CH_3OH at 6-31G/3-21G.**

Si	-5.790149	-9.967261	2.503468
H	-6.607953	-11.485441	4.709443
H	-5.109872	-11.581334	0.318978
H	-7.961552	-8.360844	1.765613
H	-4.937285	-2.373768	2.188313
H	1.575570	-6.153702	-1.002026
Si	1.687628	-2.503472	5.864739
H	0.073557	-0.318982	6.545015
H	3.294046	-1.765617	3.693335
H	3.247461	-3.283388	8.055322
O	-0.040049	-4.762652	4.763798
Al	-1.735429	-5.418377	2.035728
O	-4.711671	-4.080228	1.795020
O	-0.019849	-5.414940	-0.783285
O	-3.041666	-8.563473	3.246846
H	-1.497091	-8.670179	8.954816
O	-1.820356	-9.966766	7.771238
H	-2.366309	-9.013715	4.931339
C	-0.918513	-12.333768	8.683374
H	-1.515268	-13.761653	7.352731
H	-1.734775	-12.746583	10.511336
H	1.123448	-12.332038	8.812528

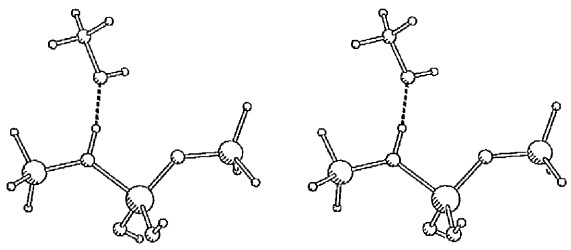

(15) Co-ordinates and stereoview of Si-H T3 cluster + NH_3 at 3-21G/NONE.

Si	-5.790149	-9.967261	2.503468
H	-6.607953	-11.485441	4.709443
H	-5.109872	-11.581334	0.318978
H	-7.961552	-8.360844	1.765613
H	-4.937285	-2.373768	2.188313
H	1.575570	-6.153702	-1.002026
Si	1.687628	-2.503472	5.864739
H	0.073557	-0.318982	6.545015
H	3.294046	-1.765617	3.693335
H	3.247461	-3.283388	8.055322
O	0.407225	-5.243922	5.004298
Al	-1.627690	-5.508272	2.365819
O	-3.260663	-2.691550	2.767630
O	-0.054456	-5.586581	-0.492740
O	-3.353518	-8.180889	3.204096
H	0.210436	-7.241522	6.560414
N	-0.345019	-9.084054	7.566009
H	-1.731542	-9.656590	6.360889
H	-1.044358	-8.778251	9.320746
H	1.083561	-10.352853	7.643330

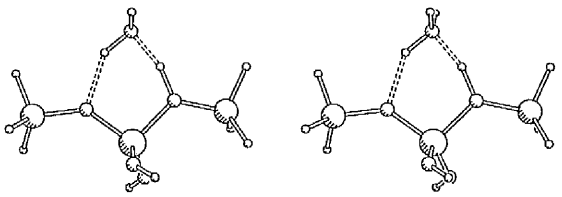

(16) Co-ordinates and stereoview of Si-H T3 cluster + NH_4^+ at 3-21G/NONE.

Si	-5.790149	-9.967261	2.503468
H	-6.607953	-11.485441	4.709443
H	-5.109872	-11.581334	0.318978
H	-7.961552	-8.360844	1.765613
H	-4.937285	-2.373768	2.188313
H	1.575570	-6.153702	-1.002026
Si	1.687628	-2.503472	5.864739
H	0.073557	-0.318982	6.545015
H	3.294046	-1.765617	3.693335
H	3.247461	-3.283388	8.055322
O	0.007579	-4.932767	4.996095
Al	-1.732304	-5.679331	2.379118
O	-3.684290	-3.346216	1.304641
O	0.590279	-6.923483	0.298058
O	-3.207520	-8.451469	3.271285
H	2.234843	-9.181632	5.144968
N	1.404993	-10.115806	3.699703
H	-0.564418	-9.977802	3.957259
H	2.043612	-11.899478	3.518309
H	1.539423	-8.947390	1.987250

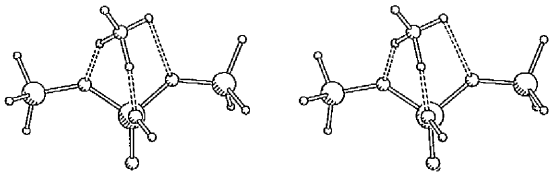

(17) Co-ordinates and stereoview of Si-H T3 cluster + NH_4^+ at 3-21G/3-21G.

Si	-5.790149	-9.967261	2.503468
H	-6.607953	-11.485441	4.709443
H	-5.109872	-11.581334	0.318978
H	-7.961552	-8.360844	1.765613
H	-4.937285	-2.373768	2.188313
H	1.575570	-6.153702	-1.002026
Si	1.687628	-2.503472	5.864739
H	0.073557	-0.318982	6.545015
H	3.294046	-1.765617	3.693335
H	3.247461	-3.283388	8.055322
O	0.407225	-5.243922	5.004298
Al	-1.627690	-5.508272	2.365819
O	-3.260663	-2.691550	2.767630
O	-0.054456	-5.586581	-0.492740
O	-3.353518	-8.180889	3.204096
H	0.210436	-7.241522	6.560414
N	-0.345019	-9.084054	7.566009
H	-1.731542	-9.656590	6.360889
H	-1.044358	-8.778251	9.320746
H	1.083561	-10.352853	7.643330

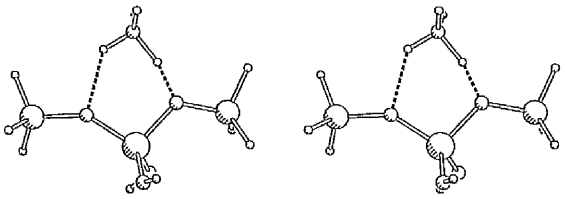

(18) Co-ordinates and stereoview of Si-H T3 cluster + NH_3 at 6-31G/NONE.**

Si	-5.790148	-9.967261	2.503467
H	-6.607952	-11.485441	4.709443
H	-5.109872	-11.581333	0.318978
H	-7.961552	-8.360844	1.765612
H	-4.937284	-2.373767	2.188313
H	1.575569	-6.153702	-1.002025
Si	1.687628	-2.503471	5.864738
H	0.0735565	-0.3189815	6.545014
H	3.294046	-1.765617	3.693335
H	3.247460	-3.283387	8.055321
O	0.0144363	-5.057616	5.113170
Al	-1.826491	-5.719739	2.103411
O	-3.357709	-2.904969	1.549766
O	0.285826	-6.874328	-0.035268
O	-3.496724	-8.198564	3.412342
H	0.065379	-6.537109	6.264344
N	-0.157904	-9.171516	8.038234
H	-1.618919	-9.876689	7.055258
H	-0.657538	-9.039334	9.858496
H	1.286463	-10.387973	7.908731

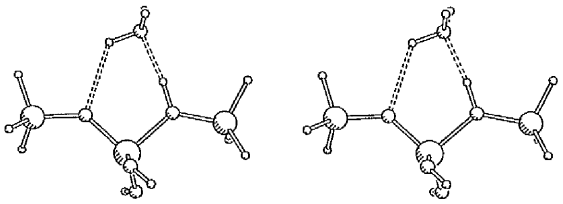

(19) Co-ordinates and stereoview of Si-H T3 cluster + NH_4^+ at 6-31G/NONE.**

Si	-5.790148	-9.967261	2.503467
H	-6.607952	-11.485441	4.709443
H	-5.109872	-11.581333	0.318978
H	-7.961552	-8.360844	1.765612
H	-4.937284	-2.373767	2.188313
H	1.575569	-6.153702	-1.002025
Si	1.687628	-2.503471	5.864738
H	0.073556	-0.318981	6.545014
H	3.294046	-1.765617	3.693335
H	3.247460	-3.283387	8.055321
O	0.050778	-4.940223	5.049412
Al	-1.751337	-5.597598	2.313640
O	-3.620504	-3.150414	1.263638
O	0.537144	-6.938972	0.210379
O	-3.324958	-8.369927	3.315238
H	1.923944	-8.495834	5.365282
N	1.535645	-9.899942	4.129707
H	-0.3627394	-10.193171	4.280972
H	2.570258	-11.459796	4.411825
H	1.720443	-9.107104	2.343383

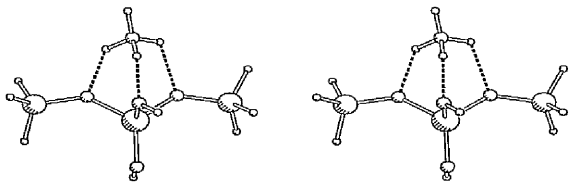

(20) Co-ordinates and stereoview of Si-H T3 cluster + NH_3 at 6-31G/3-21G.**

Si	-5.790148	-9.967261	2.503467
H	-6.607952	-11.485441	4.709443
H	-5.109872	-11.581333	0.318978
H	-7.961552	-8.360844	1.765612
H	-4.937284	-2.373767	2.188313
H	1.575569	-6.153702	-1.002025
Si	1.687627	-2.503472	5.864739
H	3.247460	-3.283389	8.055322
H	0.073556	-0.318982	6.545015
H	3.294045	-1.765618	3.693336
O	0.302974	-5.207349	4.985484
Al	-1.723352	-5.353874	2.066991
O	-3.205813	-2.453546	2.529721
O	0.213227	-5.107210	-0.598852
O	-3.440836	-8.051082	2.908226
H	0.096181	-6.561912	6.336328
N	-0.108319	-8.730069	8.473379
H	1.556003	-9.523970	8.923427
H	-1.210862	-10.116448	7.796889
H	-0.897884	-8.145776	10.098619

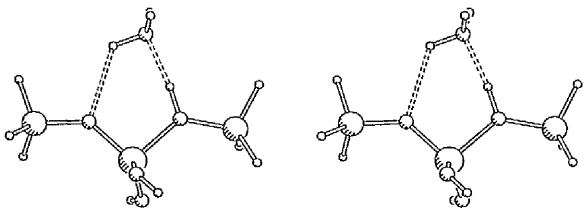

(21) Co-ordinates and stereoview of Si-H T3 cluster + NH_4^+ at 6-31G/3-21G.**

Si	-5.790148	-9.967261	2.503467
H	-6.607952	-11.485441	4.709443
H	-5.109872	-11.581333	0.318978
H	-7.961552	-8.360844	1.765612
H	-4.937284	-2.373767	2.188313
H	1.575569	-6.153702	-1.002025
Si	1.687628	-2.503471	5.864738
H	0.073556	-0.318981	6.545014
H	3.294046	-1.765617	3.693335
H	3.247460	-3.283387	8.055321
O	0.351620	-5.155933	5.039460
Al	-1.628734	-5.395762	2.290455
O	-3.245753	-2.535020	2.654591
O	0.027890	-5.392742	-0.594817
O	-3.426547	-8.151204	3.163486
H	-0.220420	-7.311681	7.083187
N	-0.817336	-8.832772	8.218191
H	-2.147163	-9.729928	7.193097
H	-1.571249	-8.214308	9.853798
H	0.621641	-10.019296	8.596477

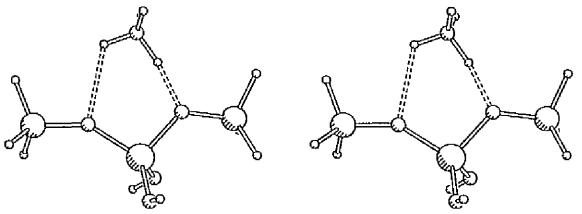

(22) Co-ordinates and stereoview of zeolite Y Si-OH terminated T2 cluster.

H	4.937286	-2.188316	2.373765
H	4.880371	-2.827379	9.319443
H	-1.575571	1.002024	6.153700
H	1.575571	-6.153700	-1.002024
H	-4.937286	-2.373765	2.188316
H	-4.880371	-9.319443	2.827379
Si	-1.687628	-5.864741	2.503470
Si	1.687628	-2.503470	5.864741
O	0.000000	-4.955659	4.955659
O	-0.093239	-0.093239	6.615316
O	0.093239	-6.615316	0.093239
O	3.463834	-1.687628	3.463834
O	-3.463834	-3.463834	1.687628
O	3.393904	-3.356608	8.260986
O	-3.393904	-8.260986	3.356608

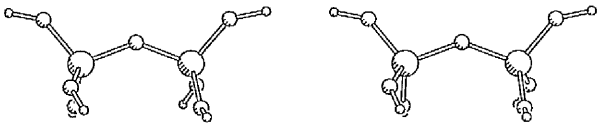

(23) Co-ordinates of sampling grid corners for Si-OH terminated T2 cluster.

-8.186435	-13.971664	-4.226306
9.012895	-13.971664	-4.226306
-8.186435	3.640896	-4.226306
9.012895	3.640896	-4.226306
-8.186435	-13.971664	13.592870
9.012895	-13.971664	13.592870
-8.186435	3.640896	13.592870
9.012895	3.640896	13.592870

(24) Co-ordinates and stereoview of Si-OH T2 cluster + NH_4^+ at 3-21G/NONE.

H	-4.9372870	-2.3737669	2.1883148
O	-3.4638331	-3.4638350	1.6876261
H	1.5755728	-6.1537021	-1.0020257
O	0.0932410	-6.6153189	0.0932372
H	-4.8803703	-9.3194459	2.8273769
O	-3.3939037	-8.2609892	3.3566062
O	3.3939094	-3.3566081	8.2609874
H	4.8803778	-2.8273788	9.3194440
O	-0.0932334	-0.0932391	6.6153189
H	-1.5755672	1.0020238	6.1537021
O	3.4638406	-1.6876280	3.4638350
H	4.9372926	-2.1883148	2.3737650
Si	1.6935107	-2.4717625	5.8575385
O	0.0880102	-5.0175437	5.2539012
Al	-1.5897760	-5.7513113	2.5244915
H	-0.2298909	-7.3010780	7.0004905
N	-1.1027103	-9.0863916	7.4120484
H	-2.3373311	-9.0831621	5.6640097
H	0.1608176	-10.5131579	7.4233396
H	-2.0937094	-9.0463615	9.0388215

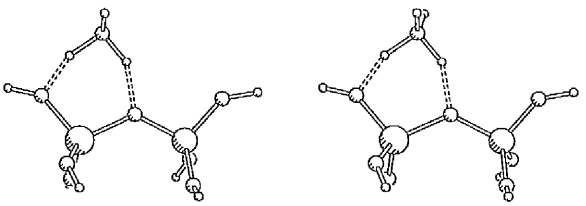

(25) Co-ordinates and stereoview of Si-OH T2 cluster + NH_4^+ at 3-21G/3-21G.

H	-4.9372870	-2.3737669	2.1883148
O	-3.4638331	-3.4638350	1.6876261
H	1.5755728	-6.1537021	-1.0020257
O	0.0932410	-6.6153189	0.0932372
H	-4.8803703	-9.3194459	2.8273769
O	-3.3939037	-8.2609892	3.3566062
O	3.3939094	-3.3566081	8.2609874
H	4.8803778	-2.8273788	9.3194440
O	-0.0932334	-0.0932391	6.6153189
H	-1.5755672	1.0020238	6.1537021
O	3.4638406	-1.6876280	3.4638350
H	4.9372926	-2.1883148	2.3737650
Si	1.6748572	-2.4898075	5.8669115
O	0.0881180	-5.0162360	5.2406372
Al	-1.5858057	-5.7791526	2.5361058
H	-0.1236543	-7.4481176	7.0945120
N	-0.9722946	-9.2210762	7.4286913
H	-2.2101090	-9.2283025	5.7903323
H	0.3031367	-10.6425834	7.3726646
H	-1.9311684	-9.2541672	9.0801404

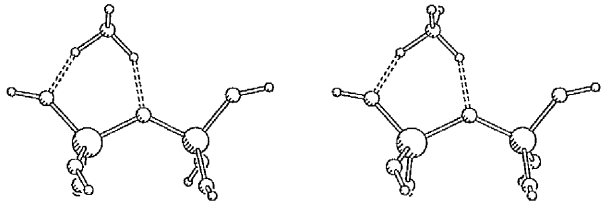

(26) Co-ordinates and stereoview of Si-OH T2 + NH_4^+ at 6-31G/NONE.**

H	-4.9372870	-2.3737669	2.1883148
O	-3.4638331	-3.4638350	1.6876261
H	1.5755728	-6.1537021	-1.0020257
O	0.0932410	-6.6153189	0.0932372
H	-4.8803703	-9.3194459	2.8273769
O	-3.3939037	-8.2609892	3.3566062
O	3.3939094	-3.3566081	8.2609874
H	4.8803778	-2.8273788	9.3194440
O	-0.0932334	-0.0932391	6.6153189
H	-1.5755672	1.0020238	6.1537021
O	3.4638406	-1.6876280	3.4638350
H	4.9372926	-2.1883148	2.3737650
Si	1.7092256	-2.4682646	5.8500155
O	0.1326947	-5.0093763	5.3505607
Al	-1.5452182	-5.7064473	2.5773113
H	-0.1892372	-7.6641304	7.4035031
N	-1.1830313	-9.3274848	7.5022659
H	-2.3175305	-9.1785555	5.7788163
H	-0.0083866	-10.8136207	7.4531368
H	-2.2452088	-9.3860664	9.0698527

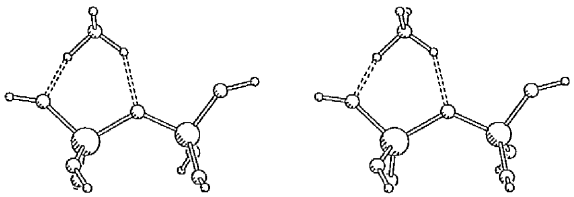

(27) Co-ordinates and stereoview of Si-OH T2 cluster + NH_4^+ at 6-31G/3-21G.**

H	-4.9372870	-2.3737669	2.1883148
O	-3.4638331	-3.4638350	1.6876261
H	1.5755728	-6.1537021	-1.0020257
O	0.0932410	-6.6153189	0.0932372
H	-4.8803703	-9.3194459	2.8273769
O	-3.3939037	-8.2609892	3.3566062
O	3.3939094	-3.3566081	8.2609874
H	4.8803778	-2.8273788	9.3194440
O	-0.0932334	-0.0932391	6.6153189
H	-1.5755672	1.0020238	6.1537021
O	3.4638406	-1.6876280	3.4638350
H	4.9372926	-2.1883148	2.3737650
Si	1.6897237	-2.4895335	5.8564784
O	0.1310979	-5.0119387	5.3449048
Al	-1.5507494	-5.7463545	2.5899724
H	-0.0248839	-7.7834383	7.5349865
N	-0.9696547	-9.4643917	7.6245539
H	-2.1376550	-9.3790668	6.0278785
H	0.2418302	-10.9231757	7.5103218
H	-1.9769735	-9.5876208	9.2297444